

SOLAR ENERGY TO HYDROGEN FUEL  
VIA HIGHLY EFFICIENT III-V SEMICONDUCTORS

by

James L. Young

B.S., University of Illinois at Urbana-Champaign, 2010

A thesis submitted to the  
Faculty of the Graduate School of the  
University of Colorado in partial fulfillment  
of the requirement for the degree of  
Doctor of Philosophy  
Materials Science and Engineering Program  
2016

ProQuest Number: 10108680

All rights reserved

INFORMATION TO ALL USERS

The quality of this reproduction is dependent upon the quality of the copy submitted.

In the unlikely event that the author did not send a complete manuscript and there are missing pages, these will be noted. Also, if material had to be removed, a note will indicate the deletion.



ProQuest 10108680

Published by ProQuest LLC (2016). Copyright of the Dissertation is held by the Author.

All rights reserved.

This work is protected against unauthorized copying under Title 17, United States Code  
Microform Edition © ProQuest LLC.

ProQuest LLC.  
789 East Eisenhower Parkway  
P.O. Box 1346  
Ann Arbor, MI 48106 - 1346

This thesis entitled:  
Solar energy to hydrogen fuel via highly efficient III-V semiconductors  
written by James L. Young  
has been approved for the Materials Science and Engineering Program

---

Steven M. George

---

Todd G. Deutsch

Date\_\_\_\_\_

The final copy of this thesis has been examined by the signatories, and we find that both the content and the form meet acceptable presentation standards of scholarly work in the above mentioned discipline.

# Abstract

Young, James Luke (Ph.D., Materials Science and Engineering)

## **Solar energy to hydrogen fuel via highly efficient III-V semiconductors**

Thesis directed by research advisor Todd G. Deutsch and academic advisor Steven M. George

A sustainable energy economy depends critically on the conversion of renewable energy resources, whose inherent variability requires a storage mechanism. Pathways for conversion of solar energy, being the most abundant, to fuel represent crucial areas of research. Hydrogen as a chemical energy carrier is storable and transportable, while being a feedstock for ammonia fertilizer that is essential to global food supply. Direct photoelectrochemical conversion of sunlight via water splitting is a prominent concept for clean, scalable, cost-effective, and locally produced hydrogen, but the technology is not yet commercially viable. Here, we address the technical challenges of realizing economical solar hydrogen production using III-V semiconductor-based devices: high conversion efficiency and extended lifetime in aqueous electrolyte.

Solar-to-hydrogen conversion efficiency is a fundamental metric for evaluating progress that will impact introduction of commercial solar water-splitting systems. Its definition is generally agreed upon, but measurement technique standards are not well defined. We demonstrate common practices, show how they can lead to significant error, and introduce methodology and cross-validation practices for improved accuracy. The advanced techniques are relevant to device configurations based on tandem absorbers, necessary for achieving maximum conversion efficiency.

We outline the development pathway for III-V tandem devices to reach maximum efficiency, demonstrate progress toward 15% enabled by a new architecture allowing lower bandgaps, and investigate alternative p-i and p-n PEC junction doping profiles that enhance photovoltage. We identify reflection as the primary loss and model anti-reflective TiO<sub>2</sub> coatings that demonstrate improved photocurrent.

We present findings on the intrinsic stability of III-V photocathodes and the development of stabilizing surface modifications. We show that water vapor reversibly passivates p-GaInP<sub>2</sub> surfaces and derive a model describing the behavior. Bare p-GaAs photocathodes etch ~100x slower than other III-V photocathodes due to residual surface As. Bare p-GaInP<sub>2</sub> is unstable, but surface modification involving nitridation and/or PtRu alloy co-catalyst deposition offers corrosion resistance. We show that sputtered PtRu consistently provides better initial performance than other treatment variations, making it preferable for device development. Department of Energy progress milestones are exceeded for STH efficiency and approached for durability, while considerable reduction of device processing cost remains to be addressed.

## Acknowledgements

I gratefully acknowledge support from the National Science Foundation through a Graduate Research Fellowship (Grant No. DGE1144083). Further financial support was provided by the U.S. Department of Energy (DOE) under Contract No. DE-AC36-08GO28308 with the National Renewable Energy Laboratory.

Thank you to my research advisor, Todd Deutsch, for introducing me to the field and continued opportunity and support throughout. Thank you to Henning Döscher and John Turner for countless valuable and challenging discussions; to Myles Steiner and Ryan France for device design; Waldo Olavarria and Alan Kibbler for operating the epitaxy systems; to Michelle Young, Arrelaine Dameron, and Anna Duda for device processing assistance; and to John Geisz for use of the band bending calculator.

Thank you to Steven George for academic advising, providing ALD advice, use of reactors and related equipment; and to Chris Bowman and Sabria Khushad for advising specific to the Materials Science and Engineering Program.

# Table of Contents

<b>Title page</b> .....	i
<b>Signature page</b> .....	ii
<b>Abstract</b> .....	iii
<b>Acknowledgements</b> .....	iv
<b>Table of contents</b> .....	v
<b>List of tables</b> .....	vi
<b>List of figures</b> .....	vii
<b>List of publications</b> .....	ix
<b>1. Introduction and background</b> .....	1
1.1 Renewable hydrogen from abundant sunlight.....	1
1.2 Tandems: III-V PEC state of the art.....	6
<b>2. Development of auxiliary components and techniques</b> .....	14
2.1 Evaluation of common characterization practices.....	14
2.2 Components for on-sun and two-source solar simulation.....	24
2.3 Photoelectrode mounting and compression cell design.....	32
2.4 Measuring the spectral response of tandems.....	38
<b>3. Tandem III-V semiconductor devices for water splitting</b> .....	42
3.1 Toward maximum efficiency with III-Vs.....	42
3.2 Light-limited photocurrent: Band gap and reflection.....	47
3.3 Photocurrent onset potential: Improving with doping profiles.....	54
3.4 Design and demonstration of anti-reflective TiO <sub>2</sub> coating.....	65
<b>4. Stability and stabilization of III-Vs</b> .....	71
4.1 Surface passivation of GaInP <sub>2</sub> by water vapor.....	71
4.2 Remarkable stability of unmodified GaAs photocathodes.....	83
4.3 Stabilizing GaInP <sub>2</sub> with nitridation and Pt/Ru sputtering.....	96
<b>5. Conclusions and outlook</b> .....	117
4.1 Conclusions.....	117
4.1 Outlook.....	118
<b>Complete bibliography</b> .....	120

# List of tables

## Chapter 2 Tables

2.2.1 Collimating tube design parameters.....	27
---	----

## Chapter 4 Tables

4.3.1 Tabulated Pt and Ru loading averages.....	102
4.3.2 Summary of durability metrics.....	106

# List of Figures

## Chapter 1 Figures

1.1.1 Comparison of PV-electrolysis and PEC.....	2
1.1.2 Water splitting principles and requirements.....	4
1.1.3 Schematic of III-V tandem PEC device.....	8

## Chapter 2 Figures

2.1.1 Solar and laboratory light source spectral flux .....	15
2.1.2 Theoretical current limit vs. absorber bandgap for various light sources.....	16
2.1.3 Device structure of classical GaInP <sub>2</sub> /GaAs PEC/PV tandem.....	17
2.1.4 Spectral response of GaInP <sub>2</sub> /GaAs PEC/PV tandem.....	19
2.1.5 Comparison of solar reference spectra to measured solar flux.....	20
2.1.6 Water splitting performance under actual sunlight.....	21
2.1.7 Spectral transmission of photoelectrode mounting epoxy.....	23
2.2.1 Picture of apparatus and collimating tube used for on-sun measurements.....	25
2.2.2 Collimating tube schematic and design parameters .....	26
2.2.3 Collimating tube alignment.....	28
2.2.4 Comparison of "AM 1.5G filter" to the AM 1.5G reference spectrum.....	29
2.2.5 Two-source solar simulator design and spectral output.....	31
2.3.1 Epoxy-mounted photoelectrode and cross-section schematic.....	33
2.3.2 PEC compression cell components and assembly sequence.....	36
2.3.3 Hydrogen evolving from photoelectrode in the compression cell mount.....	37
2.4.1 Schematic of spectral response measurement components.....	39

## Chapter 3 Figures

3.1.1 Isoefficiency contour plot.....	43
3.1.2 Inverted metamorphic tandem device structure.....	44
3.1.3 Spectral response of upright, inverted, and inverted metamorphic tandems.....	46
3.2.1 Schematic and calculation of reflectance losses of a PEC cell.....	49
3.2.2 Absorbed photon-to-current efficiency from incident photon-to-current efficiency.....	53
3.3.1 Initial IV characterization of inverted metamorphic tandem.....	56

3.3.2 Description and structures of the "p-i" and "p-n" doping profiles investigated.....	57
3.3.3 Band bending of uniformly doped p-GaInP <sub>2</sub> photocathode.....	60
3.3.4 Band bending and IV characterization of "p-i" doping profiles.....	61
3.3.5 Band bending and IV characterization of "p-n" doping profiles.....	63
3.3.6 IV characterization of inverted metamorphic tandem with "p-n" PEC junction.....	64
3.4.1 Modeling of tandem spectral response with anti-reflective TiO <sub>2</sub> coating.....	66
3.4.2 IV characterization of TiO <sub>2</sub> coating on p-GaInP <sub>2</sub> photocathode and FTO.....	67

## Chapter 4 Figures

4.1.1 GaInP <sub>2</sub> photoluminescence response to ambient.....	74
4.1.2 Schematic of photoluminescence dependence on ambient.....	76
4.1.3 Photoluminescence dependence on water vapor pressure and model fits.....	80
4.2.1 GaAs IV characterization and durability testing.....	86
4.2.2 Post-durability characterization.....	88
4.2.3 Post-durability X-ray photoelectron spectroscopy.....	91
4.3.1 Nitridation and PtRu sputtering treatment vacuum chamber.....	97
4.3.2 Treated sample cleaving schematic and PtRu loading values.....	101
4.3.3 Durability testing: Potential vs. time.....	104
4.3.4 Durability testing: IV characterization before and after.....	105
4.3.5 Durability testing: Photovoltage performance metrics.....	107
4.3.6 Post-durability analysis: Stereomicroscope images.....	109
4.3.7 Post-durability analysis: Optical profilometry.....	110
4.3.8 Corrosion evolution and post-analysis of untreated p-GaInP <sub>2</sub> .....	111

## List of Publications

- [1] J. L. Young, K. X. Steirer, J. Dzara, Michael, J. A. Turner, and T. G. Deutsch, “Remarkable stability of unmodified GaAs photocathodes during hydrogen evolution in acidic electrolyte,” *J. Mater. Chem. A*, 2015.
- [2] J. L. Young, H. Döscher, J. A. Turner, and T. G. Deutsch, “Reversible GaInP<sub>2</sub> surface passivation by water adsorption: A model system for ambient-dependent photoluminescence,” *J. Phys. Chem. C*, Under Revision.
- [3] H. Döscher<sup>†</sup>, J. L. Young<sup>†</sup>, J. F. Geisz, J. A. Turner, and T. G. Deutsch, “Solar to hydrogen efficiency: Shining light on photoelectrochemical device performance,” *Energy Environ. Sci.*, 2015.
- [4] B. A. MacLeod, K. X. Steirer, J. L. Young, U. Koldemir, A. Sellinger, J. A. Turner, T. G. Deutsch, and D. C. Olson, “Phosphonic Acid Modification of GaInP<sub>2</sub> Photocathodes Toward Unbiased Photoelectrochemical Water Splitting,” *ACS Appl. Mater. Interfaces*, 2015.
- [5] Y. Yang<sup>†</sup>, J. Gu<sup>†</sup>, J. L. Young, E. M. Miller, J. A. Turner, N. R. Neale, and M. C. Beard, “Semiconductor interfacial carrier dynamics via photoinduced electric fields,” *Science*, 2015.
- [6] J. Gu, Y. Yan, J. L. Young, K. X. Steirer, N. R. Neale, and J. A. Turner, “Water Reduction by a p-GaInP<sub>2</sub> Photoelectrode Stabilized by an Amorphous TiO<sub>2</sub> Coating and a Molecular Cobalt Catalyst,” *Nat. Mater.*, 2015.

---

<sup>†</sup> These authors contributed equally to this work.

# 1. Introduction and background

## 1.1 Renewable hydrogen from abundant sunlight

The vast majority of today's energy supply comes from fossil energy sources such as oil, coal, and natural gas that are being consumed much more rapidly than they are being replenished. Reclamation of the chemical energy stored in fossil fuel relies on combustion, which has the greenhouse gas CO<sub>2</sub> as a byproduct. Since the industrial revolution, CO<sub>2</sub> is estimated to be responsible for 70% of the rise in global temperatures [1], having unforeseeable risks and societal costs. The use of fossil fuels must be offset by 10-30 TW of carbon free power by 2050, in order to slow and reverse climate change [2].

Suitable alternatives are based on renewable energy resources: solar, wind, hydroelectric, geothermal, tidal, and biomass. However, when excluding solar from this list, a maximum of 15 TW capacity potential exists [3]. The total amount of accessible solar energy is on the order of hundreds of TW [4][5], and about 0.16% of the earth's land area is required to harvest 20 TW of solar energy using 10% efficient collectors [6]. Therefore, conversion of solar energy is a crucial area of research.

The availability of sunlight is subject to both daily and seasonal variation, requiring a storage mechanism especially when harvested on a large scale. Hydrogen as a chemical energy carrier is storable and transportable, not to mention a feedstock for ammonia fertilizer essential to global food supply [7]. Hydrogen can be generated through electrolysis of water and efficiently converted to electricity by fuel cells at its point of use. Electrolyzers are a commercially mature technology that currently contributes to hydrogen production [8]. Using

grid electricity, they can be run continuously to pay back their large capital costs. Still, the hydrogen is, at best, as carbon intensive as the energy sources used to generate the electricity.

Solar energy converted to electricity by photovoltaic (PV) cells may be used to drive electrolysis. However, the low capacity factor of solar energy requires over-sizing the electrolyzers, excessive capital cost compounding with high cost PV electricity. Thus separated PV-electrolyzer systems are expensive [8] and unlikely to provide a viable pathway for economical solar hydrogen production.

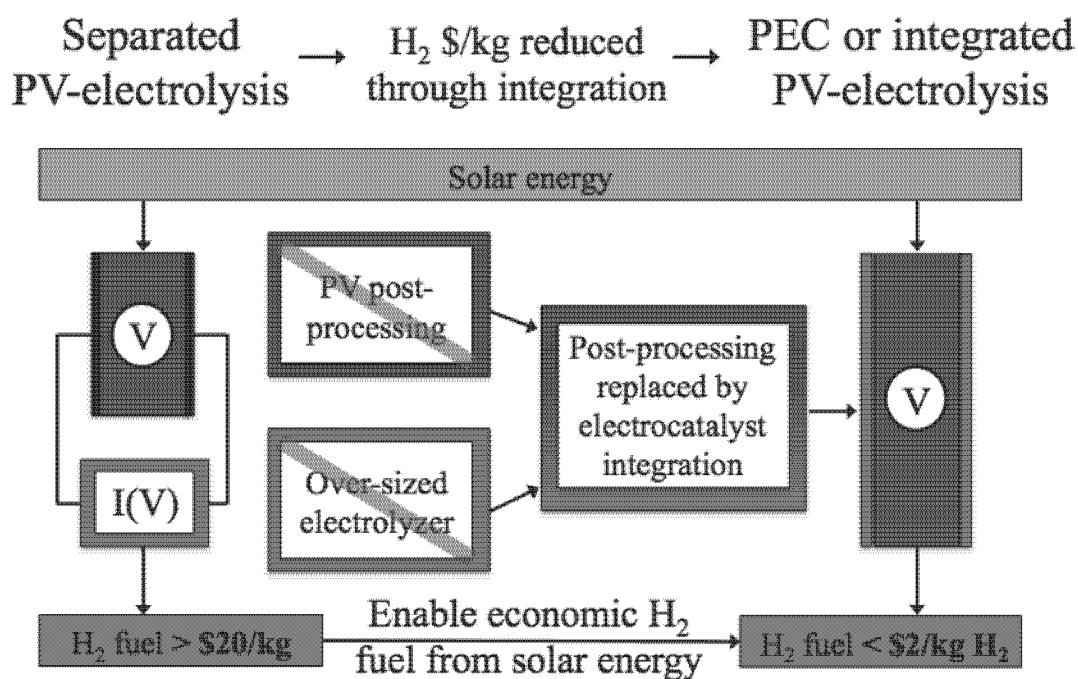


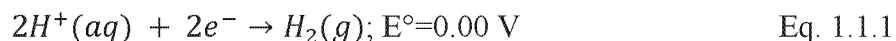
Figure 1.1.1: Separated PV-electrolysis compared to PEC or integrated PV-electrolysis and the anticipated reduction in cost of hydrogen produced.

Alternatively, the PV and electrolyzer functions can be combined into a single device to offer reduced cost and greater efficiency [9], [10]. PV post-processing steps for electricity collection such as contacts and metallization may be eliminated. Linked to solar flux, the electrolysis function occurs at low current densities making it more efficient [11] and/or allowing lower catalyst loading. When immersed in electrolyte and illuminated, a suitably selected or

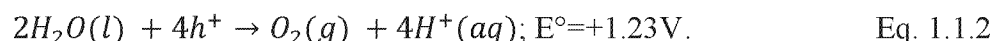
engineering semiconductor generates photovoltage to drive water splitting directly on its surface. This photoelectrochemical (PEC) approach is compelling, having the potential to be cost-competitive with gasoline (\$2-4/kg H<sub>2</sub>) [9], [10], [12].

### Photoelectrochemical water splitting principles

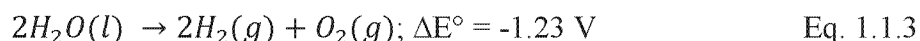
Under standard conditions, the free energy change  $\Delta G$  for splitting one molecule of H<sub>2</sub>O into H<sub>2</sub> and ½ O<sub>2</sub> is 237.2 kJ/mol [13]. Using the Nernst equation, this free energy change corresponds to a standard electrochemical potential difference  $\Delta E^\circ$  of 1.23 V. Electrochemical water splitting proceeds as two simultaneous half-reactions at spatially separate electrodes. In acidic electrolyte, the reduction half reaction proceeds at the cathode as



while the oxidation half reaction proceeds at the anode as



Combining the two half reactions gives the net water splitting reaction:



The 1.23 V thermodynamic requirement places minimum criteria on the absorber material used. Semiconductors have a bandgap, absorbing light with photon energies greater than its bandgap energy ( $E_g$ ). Upon absorption, electron and hole charge carriers are generated, but thermalize to the conduction band energy ( $E_{CB}$ ) and valence band energy ( $E_{VB}$ ), respectively (Figure 1.1.2). Since thermalization is virtually instantaneous, the semiconductor bandgap energy ( $E_g$ ), being the difference between  $E_{CB}$  and  $E_{VB}$ , must be at least 1.23 eV. When the electron and hole reach the electrolyte, they must be able to drive the reduction and oxidation half reactions,

respectively. Thus,  $E_{CB}$  must be higher (more negative) than  $E^\circ(H^+/H_2)$  while  $E_{VB}$  must be lower (more positive) than  $E^\circ(O_2/H_2O)$ ; the band edge energies must straddle the water splitting half reaction potentials.

The minimum bandgap increases when considering the kinetic overpotentials necessary to drive water splitting at reasonable rates and efficiencies. Adding overpotentials  $\eta_c = 80$  mV and  $\eta_a = 220$  mV for the HER (on Pt) and OER (on  $RuO_2$ ), respectively, as well as a 100 mV solution resistance loss [14] raises the minimum band gap to 1.63 eV. Considering energetics and kinetics, Figure 1.1.2a illustrates ideal semiconductor bandgap and  $E_{CB}$  and  $E_{VB}$  alignment.

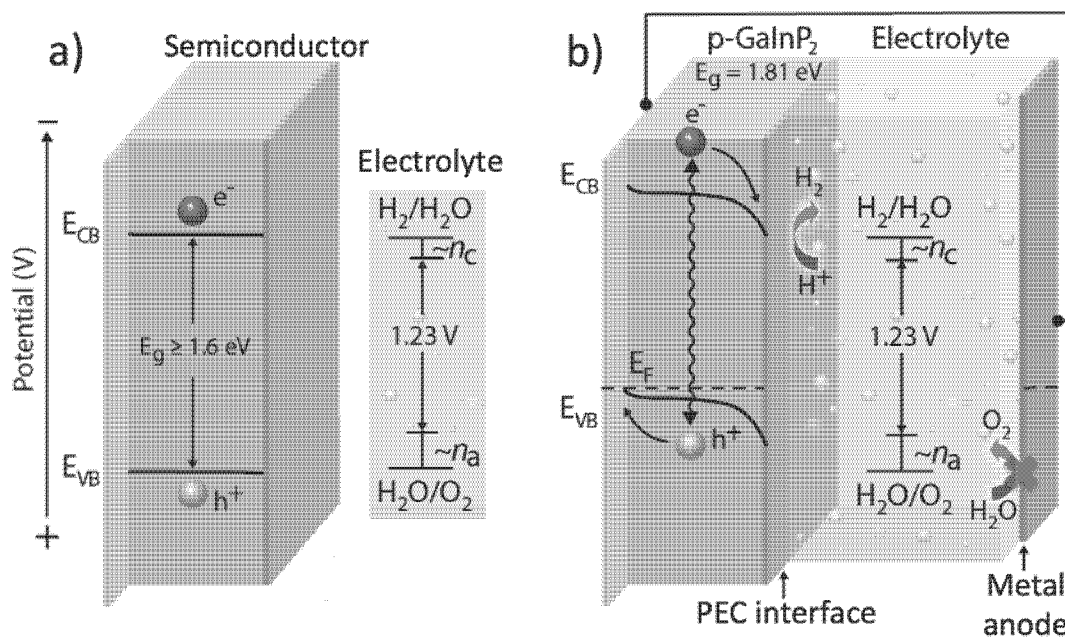


Figure 1.1.2: (a) Illustration of minimum voltage requirements for water splitting including kinetic overpotential and the resulting minimum required semiconductor bandgap. (b) Equilibration of a semiconductor, here p-GaInP<sub>2</sub>, with electrolyte resulting in band bending that separates charges to drive the reduction and oxidation half reactions. For p-GaInP<sub>2</sub>, the Fermi level is not sufficiently positive (red "X").

When the semiconductor is placed in electrolyte (Figure 1.1.2b), its Fermi level energy ( $E_f$ ) equilibrates with the electrolyte. This results in band bending, manifest as an electric field. For the case of a p-GaInP<sub>2</sub> photocathode, the field moves electrons toward the electrolyte to drive the

HER and holes to the metal anode to drive the OER. We discuss p-type photocathodes in this work. The case of an n-type photoanode is analogous, but instead with 1) oxidation occurring at the semiconductor photoanode, 2) reduction occurring at the metal counter electrode, and thus 3) photogenerated charge carriers flowing in the opposite directions [15]. The p-GaInP<sub>2</sub> photocathode  $E_{CB}$  is known to be  $\sim 0.5$  V above  $E^\circ(H_2/H_2O)$  [16]. This misalignment leaves holes at  $E_{VB}$  with insufficient potential to drive the OER (red "X", Figure 1.1.2b). A hypothetical semiconductor providing sufficient  $E_{VB}$ , would also have a larger bandgap which decreases its theoretical efficiency.

Solar-to-hydrogen (STH) efficiency is the primary factor driving the cost of hydrogen produced [10]. The ratio of total power output to total power input  $P_{total}$  defines efficiency, with the input being solar photons. The output power is the product of current density and voltage, which is a constant 1.23 V. Thus, STH efficiency is directly proportional to the current density at short circuit  $I_{sc}$  as:

$$STH = \left[ \frac{|I_{sc} (\frac{mA}{cm^2})| \times (1.23 V) \times \eta_F}{P_{total} (\frac{mW}{cm^2})} \right]_{AM\ 1.5\ G} \quad \text{Eq. 1.1.3}$$

The global solar reference spectrum is given by ASTM standard G173-3 [17], often referred to as the AM 1.5G and has  $P_{total} = 100\text{mW}/\text{cm}^2$ . Assuming a Faradaic efficiency of  $\eta_F \approx 1$  is reasonable when previously demonstrated for similar devices [18][19][20]. Still, quantifying H<sub>2</sub> yield is necessary to verify  $\eta_F$  for formal reporting.

Being directly proportional to current density, theoretical maximum STH efficiency is determined by an absorber's bandgap. Contrasting with PV devices where current and voltage must be optimized, PEC efficiency is maximized with current density, but under a constraint of sufficient voltage. A water-splitting device needing supplemental bias from an external source

requires the additional components of a separated PV-electrolysis system, which alone are too expensive. Therefore, the most important figure of merit is STH efficiency under truly unassisted conditions.

The theoretical  $E_g$ -limited photocurrent density  $J_{BG-L}$  of an absorber is defined by the amount of solar photons it is capable of absorbing. It is calculated by integrating solar photon flux density ( $J_{AM1.5G}$ ) over photons energies ( $E = hv$ ) greater than  $E_g$ :

$$J_{BG-L} = \int_{E_g}^{\infty} J_{AM1.5G}(E) dE = \int_0^{\lambda_{BG}} J_{AM1.5G}(\lambda) d\lambda \quad \text{Eq. 1.1.4}$$

where  $\lambda_{BG}$  is the wavelength corresponding to  $E_g$  [15]. The semiconductor bandgap sets the limit of integration in Eq. 1.1.4 and the portion of solar photons that contribute to its theoretical maximum current density.

We established a minimum  $E_g = 1.63$  eV for water splitting, but even the highest performance PV devices produce a photovoltage that is  $\sim 0.4$  V less than their  $E_g$  [21]. This raises the minimum  $E_g$  to  $\sim 2$  eV, for which Eq. 1.1.4 restricts single-junction absorbers to theoretical STH efficiencies below 15%. However, a tandem absorber configuration can be used, in which the two photovoltages add. Also, two bandgaps allow greater access to and more efficient utilization of the solar spectrum. Both theoretical [14], [22], [23] and experimental [18], [24], [25] results support tandem devices as a necessity to realize economically viable PEC performance [9], [10].

## 1.2 Tandems: III-V PEC state of the art

Tandem configurations place two absorbers in series where their voltage output is additive, but requires the current output of each to match for optimum performance. Current is matched by selecting an appropriate combination of bandgaps in light of the solar energy flux

distribution. Tandem configurations typically use a higher- $E_g$  top junction as a built-in spectral splitter, absorbing higher energy photons and reducing thermalization losses [26]. The photon energies that fall between the two bandgap energies are absorbed by the bottom and lower bandgap junction. Optimal photocurrent can be generated when photon flux is equally distributed. If not, one junction will be current limiting and set the overall device current.

Although the highest efficiency PV devices have more than two junctions, this would unnecessarily increase photovoltage while requiring photon flux to be divided between more junctions. Therefore, the scope of high-efficiency III-V PEC development appropriately focuses on two-junction, tandem devices.

Several groups have demonstrated tandem water-splitting devices over the past three decades. The STH efficiencies range from 0.01-12.4% for devices with at least one PEC junction and 2.3-18% for PV-electrolysis separated systems [27]. Two PEC junctions can be used, combining a photocathode and photoanode in tandem. However, successful demonstrations favor monolithic integration of PV-backed PEC junctions. For oxide-based devices, a  $\text{BiVO}_4$  PEC junction backed by one and two a-Si PV junctions achieved 3.6% and 4.9% STH respectively [24], which was compared to the 4.7% STH of a device based on a commercial a-Si triple-junction PV [25]. The seminal III-V tandem [18] achieved 12.4% in 1998, a world record maintained for 17 years until 14% was achieved by an advanced III-V tandem concept [20]. This report used a metamorphic growth technique to incorporate a lower band gap. Our current work uses an inverted architecture and metamorphic growth. The merits of this combination are presented in Ch. 3.

The traditional III-V tandem [18] consisted of a p-GaInP<sub>2</sub> photocathode epitaxially grown on a p-n GaAs PV (Figure 1.1.3). The top p-GaInP<sub>2</sub> photoelectrochemical junction has  $E_g = 1.8$

eV, allowing lower energy photons to pass to the bottom, solid-state GaAs p-n PV junction. A transparent tunnel junction electrically connects the two sub cells. The additional photovoltage of the GaAs cell overcomes the  $E_{VB}$  alignment of p-GaInP<sub>2</sub>, providing holes at the anode that have sufficient potential to drive the OER.

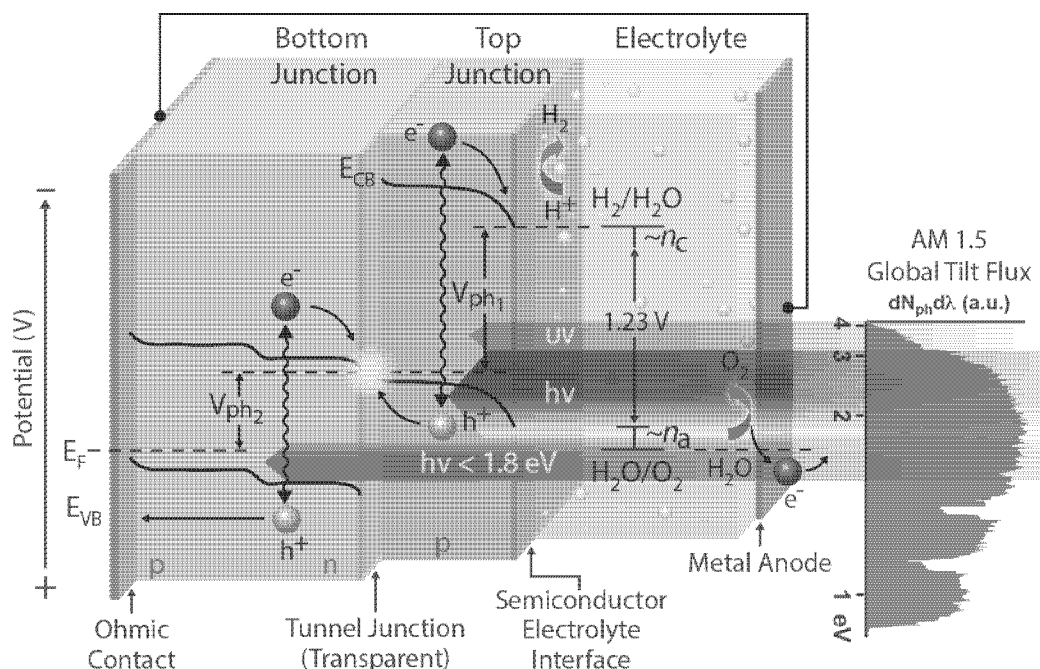


Figure 1.1.3: Diagram of a GaInP<sub>2</sub>/GaAs tandem PEC device shows spectral splitting by the 1.8/1.4 eV PEC/PV junctions with combined photovoltage driving water splitting.

The separate anode and wire interconnect allows external connection for photocurrent measurements, but may be wirelessly integrated by simply depositing OER catalyst directly on the tandem's Ohmic back contact. PEC development often involves simpler, single-absorber photoelectrodes in half-cell configurations that use an external bias from a potentiostat. The single-junction is simpler to fabricate, characterize, and can be preferable for development work. We distinguished between the two, calling single-absorbers photoelectrodes or more specifically photocathodes when the HER occurs on its surface. We refer to the full, two-junction configuration as a tandem or device.

In addition to STH efficiency, stability in contact with PEC electrolytes is a critical research challenge. Operation at reasonable STH efficiency requires strongly acidic or basic electrolytes to minimize solution resistance and concentration overpotential losses [32]. Approaches on inherently stable absorber materials, protective coatings [28][29][30], and surface modifications [31] promise improved durability. Our group [31] and others [29], [33]–[35] have made significant advances in recent years to extend the lifetime of III-V PEC devices beyond 100 hours.

Ultimately, >20% STH, 10,000 hours of stability, and semiconductor cost of \$100/m<sup>2</sup> can meet the Department of Energy's \$2/kg H<sub>2</sub> production cost goals [12][36]. Photovoltaic conversion efficiencies have been well benchmarked since the mid-1970s [37]. Demonstrated PEC efficiencies have been summarized recently [27]. In contrast, they are self-reported in the absence of standardized protocols and designated benchmarking institutions. We scrutinize our own measurement practices in Ch. 2, and with more accurate techniques, show the historical 12.4% STH efficiency record [18] to most likely be less than 10%. We continue in Ch.3, discussing the pathway and device architecture that will enable maximum STH efficiency. We demonstrate 13% STH efficiency and present photoelectrode results that should enable 16% STH when applied to our advanced tandem architecture. In Ch. 4, we present progress in understanding intrinsic stability and stabilizing surface treatments of III-V photocathodes. A new report shows that unmodified GaAs is remarkably stable, ~100x more so than other III-Vs. The explanation of excess surface As stabilizing the surface motivates further investigation and inclusion of other III-V arsenides as PEC junctions. Department of Energy progress milestones are exceeded for STH efficiency and approached for durability, while considerable reduction of device processing cost remains to be addressed.

## References

- [1] M. A. K. Khalil, “Non-CO<sub>2</sub> Greenhouse gases in the atmosphere,” *Annu. Rev. Energy Environ.*, vol. 24, no. 1, pp. 645–661, 1999.
- [2] M. I. Hoffert, K. Caldeira, A. K. Jain, E. F. Haites, L. D. D. Harvey, S. D. Potter, M. E. Schlesinger, S. H. Schneider, R. G. Watts, T. M. L. Wigley, and D. J. Wuebbles, “Energy implications of future stabilization of atmospheric CO<sub>2</sub> content,” *Nature*, vol. 395, no. 6705, pp. 881–884, 1998.
- [3] N. S. Lewis, G. Crabtree, A. J. Nozik, M. R. Wasielewski, and P. Alivisatos, “Basic Research Needs for Solar Energy Utilization,” *Basic Energy Sci. Work. Sol. Energy Util.*, p. 276, 2005.
- [4] UNDP, *World Energy Assessment. Energy and the challenge of Sustainability*. 2000.
- [5] P. Moriarty and D. Honnery, “What is the global potential for renewable energy?,” *Renew. Sustain. Energy Rev.*, vol. 16, no. 1, pp. 244–252, 2012.
- [6] R. F. Service, “Solar energy. Is it time to shoot for the sun?,” *Science*, vol. 309, no. 5734, pp. 548–551, 2005.
- [7] V. Smill and R. A. Streatfeild, “Enriching the earth: Fritz Haber, Carl Bosch, and the transformation of world food production,” *Electronic Green Journal*, no. 17. 2002.
- [8] B. Kroposki, J. Levene, K. Harrison, P. K. Sen, and F. Novachek, “Electrolysis: Information and opportunities for electric power utilities,” 2006.
- [9] B. D. James, G. N. Baum, J. Perez, and K. N. Baum, “Technoeconomic analysis of photoelectrochemical (PEC) hydrogen production,” *DOE Contract Number GS-10F-009J*, vol. 22201, no. December, pp. 1–128, 2009.
- [10] B. a. Pinaud, J. D. Benck, L. C. Seitz, A. J. Forman, Z. Chen, T. G. Deutsch, B. D. James, K. N. Baum, G. N. Baum, S. Ardo, H. Wang, E. Miller, and T. F. Jaramillo, “Technical and economic feasibility of centralized facilities for solar hydrogen production via photocatalysis and photoelectrochemistry,” *Energy Environ. Sci.*, vol. 6, no. 7, p. 1983, 2013.
- [11] B. U. Bossel, “Does a Hydrogen Economy Make Sense?,” vol. 94, no. 10, 2006.
- [12] “Department of Energy Fuel Cell Technologies Office Multi-year Research, Development, and Demonstration Plan,” 2015. [Online]. Available: [http://energy.gov/sites/prod/files/2015/06/f23/fcto\\_myRDD\\_production.pdf](http://energy.gov/sites/prod/files/2015/06/f23/fcto_myRDD_production.pdf).
- [13] A. J. Bard and L. R. Faulkner, *Electrochemical Methods: Fundamentals and Applications*.

Wiley, 2000.

- [14] H. Döscher, J. F. Geisz, T. G. Deutsch, and J. A. Turner, “Sunlight absorption in water – efficiency and design implications for photoelectrochemical devices,” *Energy Environ. Sci.*, vol. 7, no. 9, pp. 2951–2956, 2014.
- [15] T. Bak, J. Nowotny, M. Rekas, and C. . Sorrell, “Photo-electrochemical hydrogen generation from water using solar energy. Materials-related aspects,” *Int. J. Hydrogen Energy*, vol. 27, no. 10, pp. 991–1022, 2002.
- [16] B. A. MacLeod, K. X. Steirer, J. L. Young, U. Koldemir, A. Sellinger, J. A. Turner, T. G. Deutsch, and D. C. Olson, “Phosphonic Acid Modification of GaInP2 Photocathodes Toward Unbiased Photoelectrochemical Water Splitting,” *ACS Appl. Mater. Interfaces*, vol. 7, no. 21, pp. 11346–11350, 2015.
- [17] “ASTM G173-03, Standard Tables for Reference Solar Spectral Irradiances: Direct Normal and Hemispherical on 37° Tilted Surface, ASTM International, West Conshohocken, PA, 2003, [www.astm.org](http://www.astm.org).”
- [18] O. Khaselev and J. A. Turner, “A Monolithic Photovoltaic-Photoelectrochemical Device for Hydrogen Production via Water Splitting,” *Science (80-. )*, vol. 280, no. 5362, pp. 425–427, 1998.
- [19] X. Gao, “Photoelectrochemical decomposition of water using modified monolithic tandem cells,” pp. 208–214.
- [20] M. M. May, H.-J. Lewerenz, D. Lackner, F. Dimroth, and T. Hannappel, “Efficient direct solar-to-hydrogen conversion by in situ interface transformation of a tandem structure,” *Nat. Commun.*, vol. 6, p. 8286, 2015.
- [21] R. R. King, D. Bhusari, A. Boca, D. Larrabee, X.-Q. Liu, W. Hong, C. M. Fetzer, D. C. Law, and N. H. Karam, “Bandgap-Voltage Offset and Energy Production in Next-Generation Multijunction Solar Cells,” *5th World Conf. Photovolt. Energy Convers. 25th Eur. Photovolt. Sol. Energy Conf.*, pp. 6–10, 2010.
- [22] M. C. Hanna and A. J. Nozik, “Solar conversion efficiency of photovoltaic and photoelectrolysis cells with carrier multiplication absorbers,” *J. Appl. Phys.*, vol. 100, no. 7, pp. 1–8, 2006.
- [23] J. R. Bolton, S. J. Strickler, and J. S. Connolly, “Limiting and realizable efficiencies of solar photolysis of water,” *Nature*, vol. 316, no. 6028, pp. 495–500, 1985.
- [24] F. F. Abdi, L. Han, A. H. M. Smets, M. Zeman, B. Dam, and R. van de Krol, “Efficient solar water splitting by enhanced charge separation in a bismuth vanadate-silicon tandem photoelectrode,” *Nat. Commun.*, vol. 4, p. 2195, 2013.

- [25] S. Y. Reece, J. a. Hamel, K. Sung, T. D. Jarvi, a. J. Esswein, J. J. H. Pijpers, and D. G. Nocera, "Wireless Solar Water Splitting Using Silicon-Based Semiconductors and Earth-Abundant Catalysts," *Science (80-. )*, vol. 334, no. 6056, pp. 645–648, 2011.
- [26] M. a. Green, *Third generation photovoltaics: advanced solar energy conversion*, vol. 10. 2006.
- [27] J. W. Ager III, M. Shaner, K. Walczak, I. D. Sharp, and S. Ardo, "Experimental Demonstrations of Spontaneous, Solar-Driven Photoelectrochemical Water Splitting," *Energy Environ. Sci.*, vol. 2, no. 1, pp. 1–3, 2015.
- [28] S. Hu, N. S. Lewis, J. W. Ager, J. Yang, J. R. McKone, and N. C. Strandwitz, "Thin-Film Materials for the Protection of Semiconducting Photoelectrodes in Solar-Fuels Generators," *J. Phys. Chem. C*, p. 150928141004000, 2015.
- [29] S. Hu, M. R. Shaner, J. a Beardslee, M. Lichterman, B. S. Brunschwig, and N. S. Lewis, "Amorphous TiO<sub>2</sub> coatings stabilize Si, GaAs, and GaP photoanodes for efficient water oxidation.," *Science*, vol. 344, no. 6187, pp. 1005–9, 2014.
- [30] B. Seger, T. Pedersen, A. B. Laursen, P. C. K. K. Vesborg, O. Hansen, and I. Chorkendorff, "Using TiO<sub>2</sub> as a conductive protective layer for photocathodic H<sub>2</sub> evolution," *J. Am. Chem. Soc.*, vol. 135, no. 3, pp. 1057–1064, 2013.
- [31] J. Turner, T. Deutsch, H. Wang, A. Welch, and M. Al-jassim, "II.F.2 Semiconductor Materials for Photoelectrolysis," *DOE Hydrogen and Fuel Cells Program FY 2012 Annual Progress Report.*, 2012. [Online]. Available: [http://www.hydrogen.energy.gov/pdfs/progress12/ii\\_f\\_2\\_turner\\_2012.pdf](http://www.hydrogen.energy.gov/pdfs/progress12/ii_f_2_turner_2012.pdf).
- [32] M. a. Modestino, K. a. Walczak, A. Berger, C. M. Evans, S. Haussener, C. Koval, J. S. Newman, J. W. Ager, and R. a. Segalman, "Robust production of purified H<sub>2</sub> in a stable, self-regulating, and continuously operating solar fuel generator," *Energy Environ. Sci.*, vol. 7, no. 1, p. 297, 2014.
- [33] J. D. Benck, S. C. Lee, K. D. Fong, J. Kibsgaard, R. Sinclair, and T. F. Jaramillo, "Designing Active and Stable Silicon Photocathodes for Solar Hydrogen Production Using Molybdenum Sulfide Nanomaterials," *Adv. Energy Mater.*, p. n/a–n/a, 2014.
- [34] B. Mei, B. Seger, T. Pedersen, M. Malizia, O. Hansen, I. Chorkendorff, and P. C. K. Vesborg, "Protection of p + -n-Si Photoanodes by Sputter-Deposited Ir/IrO<sub>x</sub> Thin Films," *J. Phys. Chem. Lett.*, vol. 5, no. 11, pp. 1948–1952, 2014.
- [35] K. Sun, F. H. Saadi, M. F. Lichterman, W. G. Hale, H.-P. Wang, X. Zhou, N. T. Plymale, S. T. Omelchenko, J.-H. He, K. M. Papadantonakis, B. S. Brunschwig, and N. S. Lewis, "Stable solar-driven oxidation of water by semiconducting photoanodes protected by transparent catalytic nickel oxide films," *Proc. Natl. Acad. Sci.*, p. 201423034, 2015.

- [36] T. G. Deutsch and J. A. Turner, "Semiconductor Materials for Photoelectrolysis: 2014 U.S. DOE Hydrogen & Fuel Cells Program Review," 2014.
- [37] "[http://www.nrel.gov/ncpv/images/efficiency\\_chart.jpg](http://www.nrel.gov/ncpv/images/efficiency_chart.jpg)."

## **2. Development of auxiliary components and techniques**

### **2.1 Evaluation of common PEC characterization practices<sup>1</sup>**

This Chapter motivates improved PEC components and characterization techniques by evaluating some traditional measurement practices. We highlight quantitative and qualitative flaws, discuss their impact on research results and strategy, and demonstrate approaches toward advanced measurement accuracy. Our emphasis is on characterizing tandem structures designed for optimum conversion efficiency.

#### **Introduction**

We demonstrate how common practices in laboratory-scale PEC measurements impact performance reporting, namely STH efficiency. We consider 1) illumination and its calibration, 2) device active area definition, and 3) consistency of results with incident photon-to-current efficiency (IPCE). In Chapters 2.2, 2.3, and 2.4 to follow; we discuss in detail the techniques and practices of 1), 2), and 3) respectively.

#### **Illumination and its calibration**

Reference solar spectrum (AM1.5G) [1] and STH efficiency [2] are generally accepted standards. However, the spectral output of commonly used laboratory lights sources and even "solar simulators" deviate significantly and require calibration. Figure 2.1.1 shows spectra of

tungsten, xenon, and ELH sources used for PEC characterization (measured with calibrated StellarNet spectroradiometer) compared to the AM1.5G reference spectrum (ASTM G173-3). Photon flux units are used, rather than power, for direct proportionality to current density and thus STH efficiency. Integration of flux gives the theoretical current densities for a given band gap which we discuss in more detail as relevant to tandem devices in Chapter 3.2. Despite being calibrated to solar-equivalent power, the laboratory sources differ from solar flux, resulting in considerable mismatch for most bandgaps.

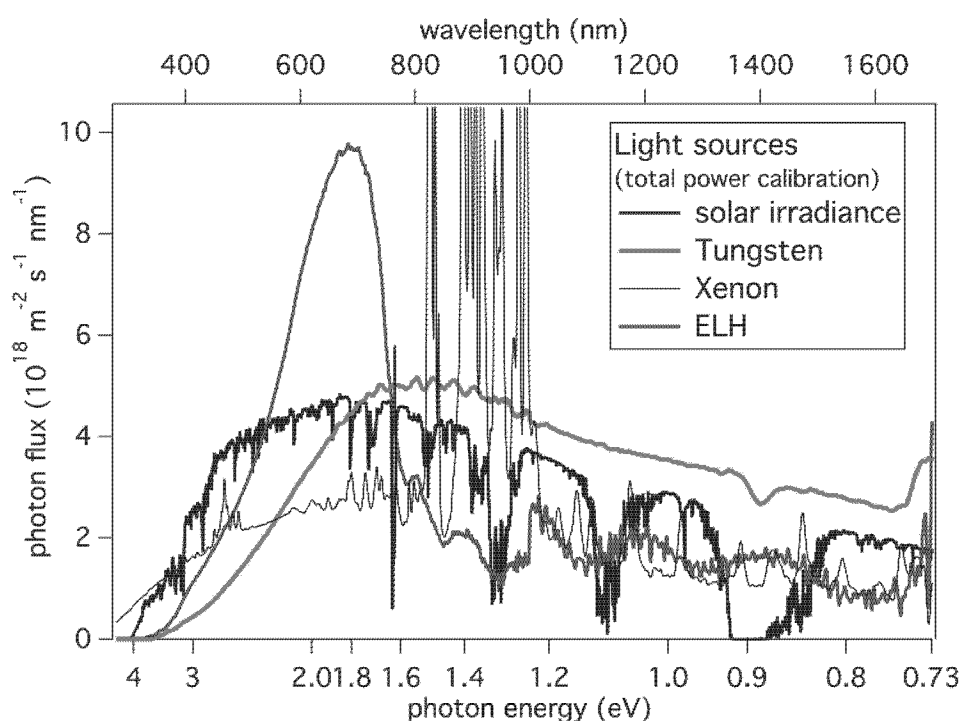


Figure 2.1.1: Spectral flux shown for AM1.5G compared to laboratory light sources (normalized to equivalent power over 200-1800 nm).

Laboratory light sources are calibrated by using a reference solar cell that was calibrated to AM1.5G. The reference cell is placed at the measurement position, and the light intensity is adjusted to the calibration current. When testing absorbers having equal band gap, systematic deviation from the current limit is removed. In Figure 2.1.2, the lab sources were calibrated using

a GaInP<sub>2</sub> (1.8 eV band gap) reference solar cell, setting the integrated flux (above 1.8 eV) for each light source and AM1.5G equal (top graph, 19.4 mA/cm<sup>2</sup>). Still, spectral distribution varies considerably among the light source types. The tungsten source is heavy in the red and lacks UV while the xenon provides excess UV.

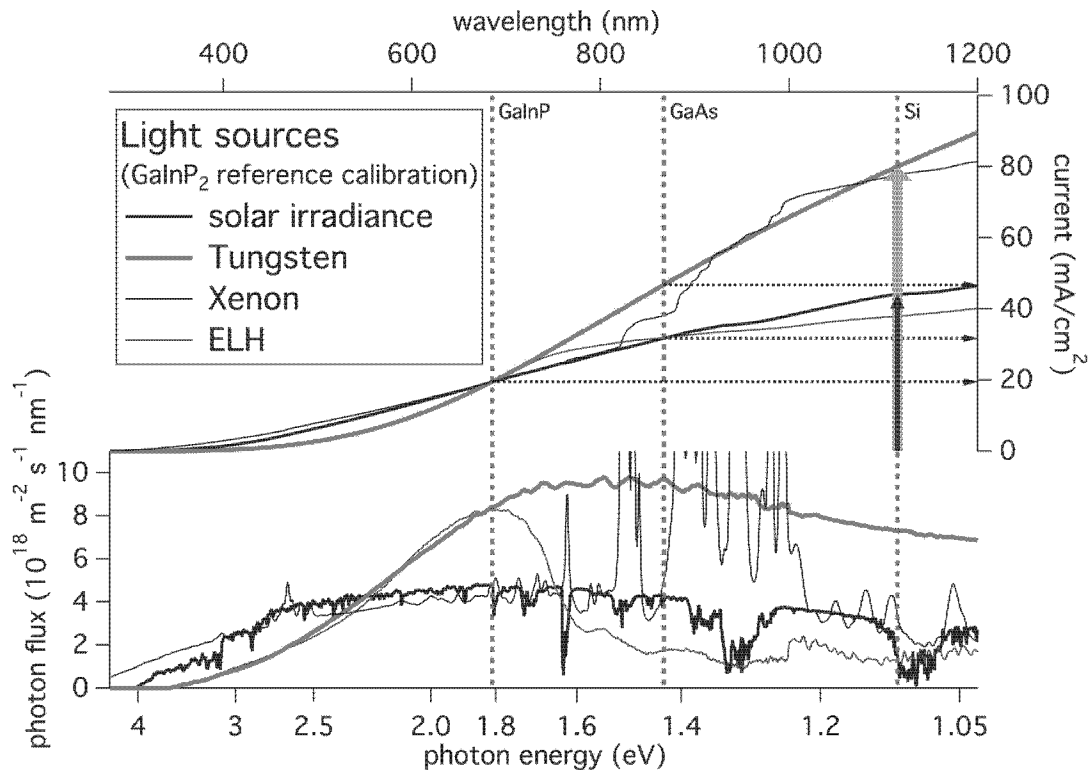


Figure 2.1.2: Theoretical current limit vs. absorber bandgap (top) for AM1.5 global illumination as well as tungsten, Xe, and ELH white light sources when calibrated with a GaInP<sub>2</sub> reference solar cell. Spectral flux of each is shown at bottom.

This calibration approach substitutes photons of different energies and thus is fully valid when such substitution does not influence current output, i.e. when charge collection efficiency (quantum efficiency) is independent of wavelength. Common practice employs a reference solar cell that is the same absorber material (same band gap) as the photoelectrode being characterized and of sufficient thickness to absorb all photons with greater energy than its band gap (i.e. optically thick). However, any calibrated reference cell could be used when the illumination

spectrum is well characterized. For example, in Fig. 2.1.2 the AM1.5G current-density limit for Si is  $44.1 \text{ mA/cm}^2$  (thin black arrow) and the tungsten source calibrated by a GaInP<sub>2</sub> reference cell would provide  $80.0 \text{ mA/cm}^2$  for its 1.12-eV bandgap (thick green arrow). Applying a correction factor (the ratio of the two currents; 1.814) allows photon flux calibration for GaInP<sub>2</sub> characterization using a Si reference cell.

### Calibrated illumination for tandems

Light source calibration for tandems is significantly more complex, requiring calibration for two absorber bands, since the top sub-cell absorption characteristics influence the flux that reaches the bottom. We demonstrate and investigate this complexity using a III-V tandem PEC structure [3] (Fig. 2.1.3a) that replicates the main features of the classical GaInP<sub>2</sub>/GaAs design[4]: 1) a 4- $\mu\text{m}$  p-type GaInP<sub>2</sub> top absorber ( $\text{Ga}_{0.51}\text{In}_{0.49}\text{P}$ , 1.81-eV bandgap) in contact with

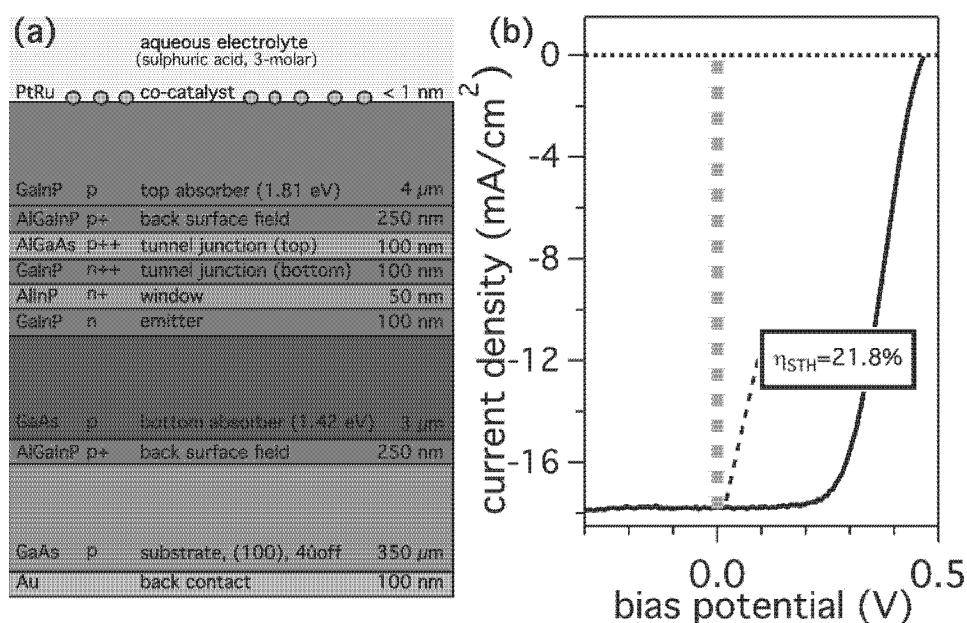


Figure 2.1.3: (a) Device structure of GaInP<sub>2</sub>/GaAs PEC/PV tandem and (b) its current density-voltage performance measured under tungsten source illumination set with a calibrated GaInP<sub>2</sub> reference solar cell.

electrolyte to form a PEC junction, 2) a bottom solid-state p-n GaAs PV junction on single-crystal GaAs(100) substrate; and 3) a tunnel junction for electrical interconnection of the two sub-cells. PtRu co-catalyst is sputtered on the p-GaInP<sub>2</sub> surface, improving hydrogen evolution kinetics and stability (see Chapter 4.3).

Figure 2.1.3b shows traditional STH efficiency characterization in a two-electrode measurement (bias V vs. IrO<sub>x</sub> counter electrode) illuminated by a tungsten source calibrated with GaInP<sub>2</sub> reference solar cell. At short circuit (0 V vs. IrO<sub>x</sub>), unassisted water-splitting proceeds at 17.7 mA/cm<sup>2</sup>, which indicates STH efficiency of 21.8%. We evaluate this performance against the theoretical current densities of Figure 2.1.2. The maximum currents under AM1.5G for GaInP<sub>2</sub> and GaAs are 19.4 mA/cm<sup>2</sup> and 31.7 mA/cm<sup>2</sup>, respectively (dotted horizontal arrows). However, the optically-thick 4- $\mu$ m GaInP<sub>2</sub> (Fig. 2.1.3a) filters all light above its bandgap energy, leaving just 12.3 mA/cm<sup>2</sup> for the GaAs junction. The maximum current from this series-connected tandem is then 12.3 mA/cm<sup>2</sup> making the measured 17.7 mA/cm<sup>2</sup> unrealistic.

The basis of this overestimation is revealed in the shape of the tungsten source spectrum (Fig. 2.1.2), which causes a large over-illumination of the GaAs bottom-junction (27.3 instead of 12.3 mA/cm<sup>2</sup>) when calibrated using a GaInP<sub>2</sub> reference cell. Here, the GaInP<sub>2</sub> top absorber is actually current limiting, establishing a 19.4 mA/cm<sup>2</sup> maximum under the improperly calibrated and mismatched and tungsten illumination. Comparing to the measured 17.7 mA/cm<sup>2</sup> (Fig. 2.1.3), we note this requires 91% of incident photons to be collected as current in the GaInP<sub>2</sub> top junction. Yet, reflection losses are ~25% in a PEC configuration, so we further challenge this result as violating the reflection-limited photocurrent (discussed in Chapter 3.2).

## IPCE for measurement (in)validation

PEC measurements can be validated against spectral response (IPCE) of the tandem device (Fig. 2.1.4). Procedures for independent sub-cell measurement is outlined and discussed in Chapter 2.4.

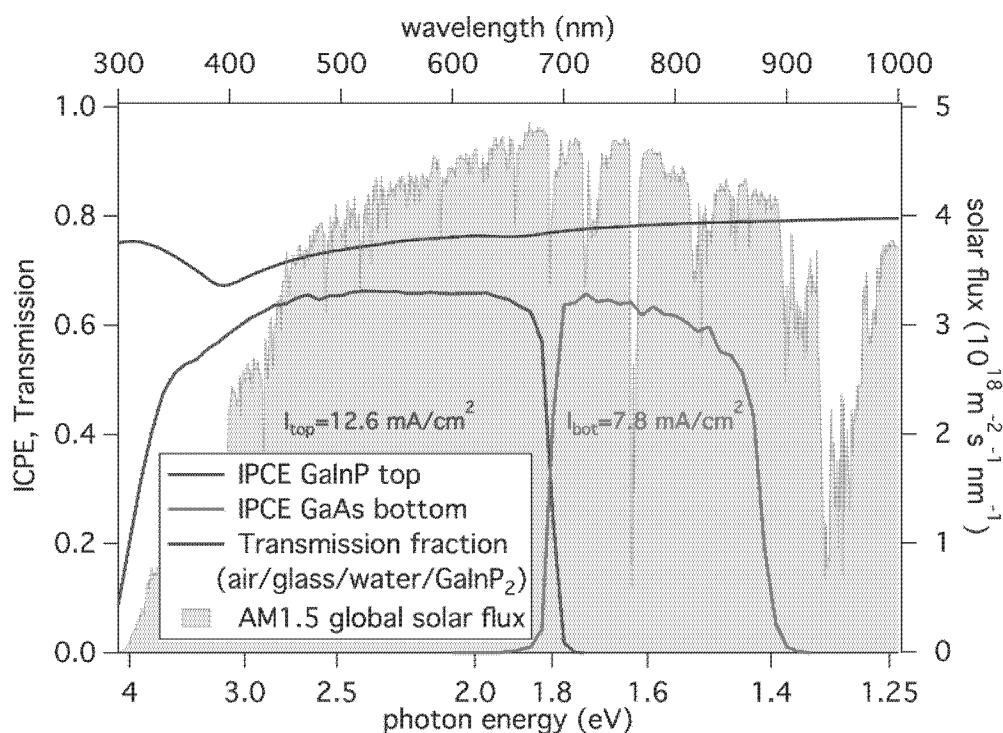


Figure 2.1.4: Independent sub-cell IPCE of GaInP<sub>2</sub> top (blue) and GaAs bottom (red) absorbers in tandem device, transmission through air/glass/electrolyte/GaInP<sub>2</sub> interfaces associated with a PEC cell (dark grey); and AM1.5G solar flux (light grey area).

In Fig. 2.1.4, the measured GaInP<sub>2</sub> (red) and GaAs (blue) IPCE values are confined to about 66% which is in agreement with the calculated transmission of air/glass/electrolyte/GaInP<sub>2</sub> interfaces (black line; by Fresnel normal-incidence model in Chapter 3.2) limiting values to about 70–80%. However, this reflection-limit confirms that our initial STH measurement (Figure 2.1.3) requiring IPCE  $\geq 91\%$  is invalid for additional reasons beyond illumination source and its calibration. Integration of IPCE data over AM1.5G irradiance gives top and bottom sub-cell currents of 12.6 and 7.8 mA/cm<sup>2</sup>, respectively, the latter current limiting to constrain the device

below 9.6% STH efficiency. These results demonstrate a consistency check based on independently-measured IPCE data.

### On-sun measurement

To minimize spectral-mismatch error, we perform PEC characterization outdoors under sunlight illumination. We compare measurements under both global and direct ( $5^\circ$  field of view) illumination, following established PV convention of normalizing data to  $1 \text{ kW/m}^2$  intensity as a 1-sun illumination level [1]. Under clear skies in the middle of the day, a representative measurement of the direct solar spectrum (Figure 2.1.5, blue) is a near-perfect match to the direct reference spectrum (Figure 2.1.5, red) and excellent match to AM1.5G when normalized (Figure 2.1.5, black).

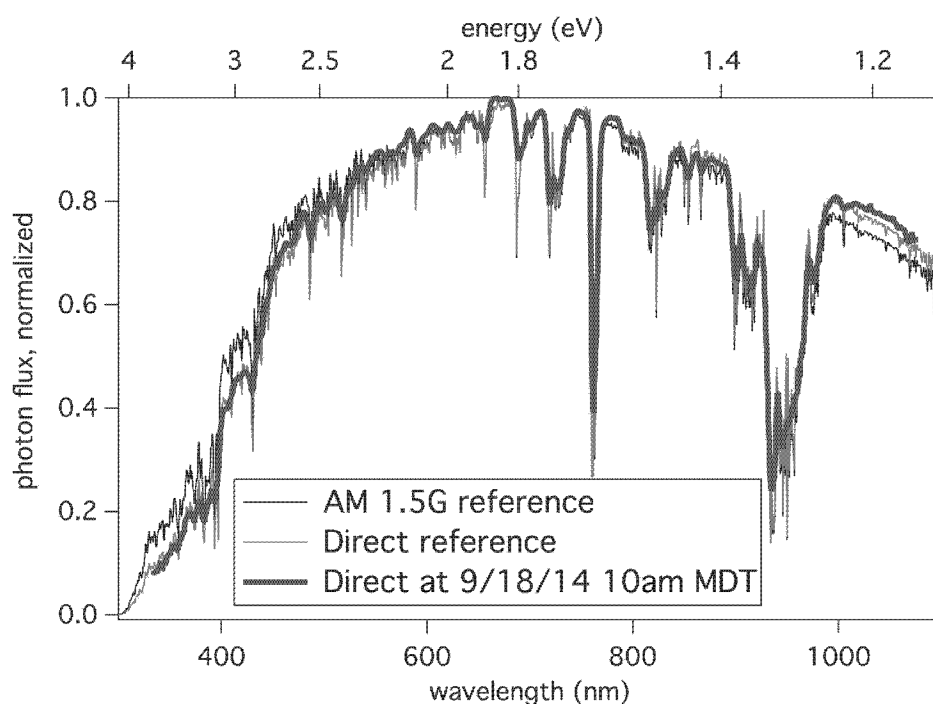


Figure 2.1.5: Normalized photon flux from global (black) and direct (red) reference spectra compared to a representative direct measurement (*credit SRRL [5]*) at 10am MDT 9/18/2014

Measurements in Fig. 2.1.6 were performed at the NREL Solar Radiation Research Laboratory (Golden, CO), where precise solar irradiance data are continuously recorded and published [5].

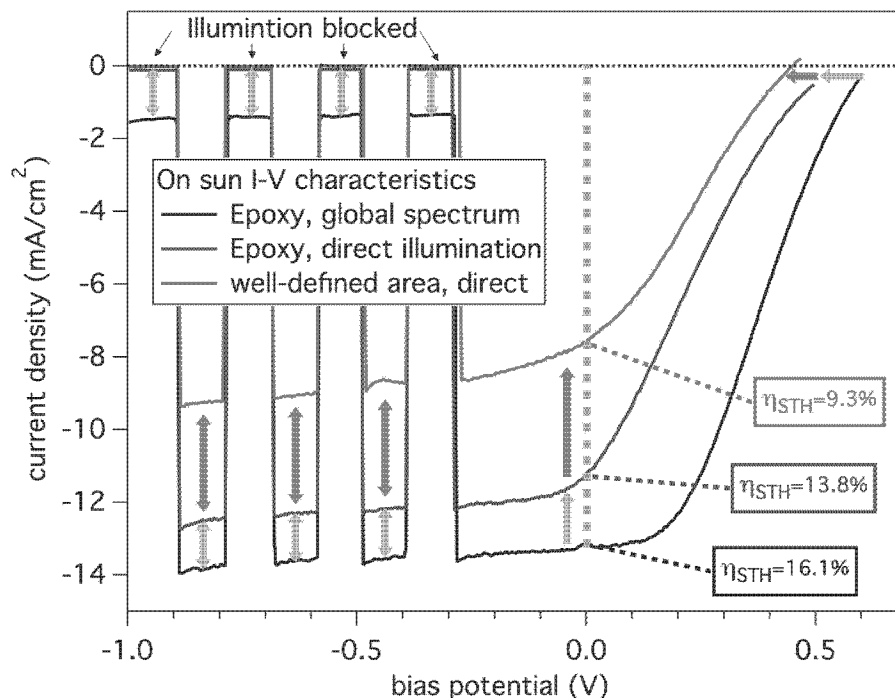


Figure 2.1.6: Water splitting performance under sunlight (outdoors) for epoxy-mounted PEC tandems with normalized global (black) and direct (blue) illumination is compared to proper area definition (red). Current density at zero bias (green dashed line) is used to calculate STH conversion efficiency  $\eta_{\text{STH}}$ .

First measurements yielded unbiased water-splitting, driven only by sunlight, at 13 mA/cm<sup>2</sup> and 16% STH (Fig. 2.1.6, black line), being lower than the laboratory result (Fig. 2.1.3), but still in violation of expectations calculated from IPCE (Fig. 2.1.4). The presence of significant current while blocking the direct light path (Fig. 2.1.6, black line) revealed contribution from indirect illumination that we suspected to be enhanced by the surrounding glassware of the PEC cell. We tested this by using a dark compartment to eliminate indirect light paths. Illumination was provided exclusively through a collimating tube restricting incident

sunlight to 5° field of view (see Figure 2.2.1). Here, the measured 11 mA/cm<sup>2</sup> for 13.8% STH (Fig. 2.1.6, blue line), is still inconsistent with expectations from IPCE data.

Last, we investigate the device area as defined by epoxy-encapsulation, common to photoelectrochemical techniques for simplicity, flexibility, and chemical resistance. Downsides discussed in Chapter 2.3 include: sample-to-sample variation of device area, unexpected under-etching or interaction with the electrolyte, and optical impact of light reflection and/or transmission. To eliminate epoxy, we performed a measurement using an alternative, compression-type PEC cell design (Chapter 2.3), where a black and opaque, inert gasket seal with concentric foil mask precisely define the active area. The result (Fig. 2.1.6, red line) might be perceived as a large decrease in performance to 7.6 mA/cm<sup>2</sup> or 9.3% in STH conversion. Yet, it is in excellent agreement with the 7.8 mA/cm<sup>2</sup> estimated by IPCE (Fig. 2.1.4).

Only the last measurement represents a reasonable and consistent STH energy-conversion efficiency while the previous are inflated or even non-physical. These demonstration measurements show that common, yet deficient, practices significantly overrate STH performance.

### **Device area definition: Epoxy transmission**

We further investigate effects of the commonly used Loctite HySol 9462 epoxy by measuring its spectral transmission, while establishing a simple procedure for characterizing other types. We discuss details of photoelectrode mounting in Chapter 2.3, showing schematic here inset in Fig. 2.1.7 to point out epoxy on the photoelectrode surface, defining an active area. Thus, light transmitted through this epoxy would be absorbed and, lateral charge transport being

sufficient, would contribute to the measured current density. Thus, device active area defined by transparent or semi-transparent epoxy is ambiguous.

We apply epoxy between two glass slides (Fig. 2.1.7) with incremental spacing between defined by a number of microscope cover slips. During epoxy curing, a weight compressing the slides together ensures epoxy thickness matching that of the cover slips.

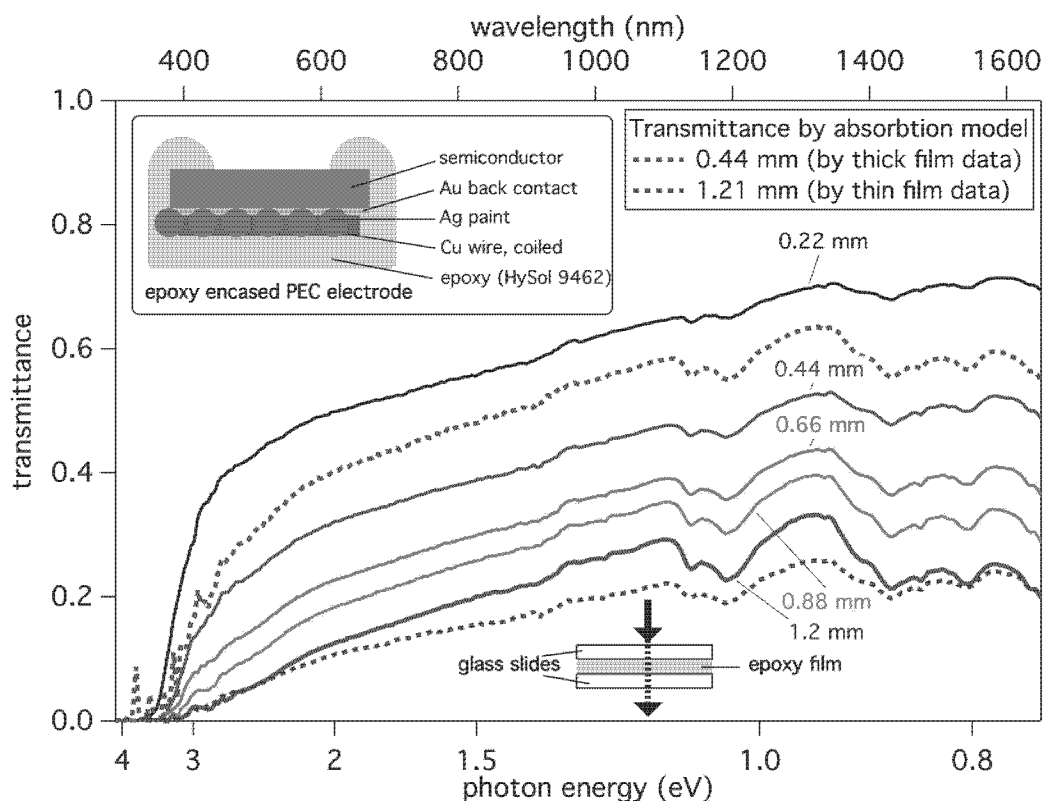


Figure 2.1.7: Spectral transmission through Loctite Hysol 9462 epoxy films between glass slides. The inset shows a schematic cross-section of epoxy-mounted PEC electrodes.

The epoxy film spectral transmittance (Fig. 2.1.7) is considerable even through thicker layers. A simple absorbance model (Fig. 2.1.7, dashed lines) is applied, which assumes transmission of the air/glass/epoxy/glass/air system depends on reflections at interfaces and absorption within the epoxy (exponential decay). The offset to data indicates sub-exponential behavior that we attribute to longer light path lengths caused by scattering within the epoxy.

The transmittance shows that Loctite Hysol 9462 poorly defines illuminated area by allowing partial illumination of covered areas. In addition to systematically overrating performance, variability in thickness and coverage for manually applied epoxy introduces error that complicates comparison among photoelectrodes. Other epoxies may be more suitable, but their use should be accompanied by optical characterization to confirm opacity.

## **Conclusions**

We demonstrated how light-source calibration for tandem devices is particularly susceptible to spectral mismatch. Furthermore, poor illuminated area definition by epoxy yielded STH efficiencies exceeding 20%, inconsistent with the ~10% STH obtained from integrating IPCE over AM1.5G solar flux. Under actual sunlight illumination and using the epoxy-free area definition of a compression cell, we measured a reasonable and consistent 9.3% STH. Outdoor, on-sun measurements provide excellent illumination match to reference spectra. Still, performing measurements in a laboratory setting can be preferable for research purposes. Common single-source "solar simulators" do not appear sufficient for tandem absorbers. Considerable improvement may be made by thoughtful design and calibration of multi-source simulators.

## **2.2 Components for on-sun and two-source solar simulation**

### **Collimating tube design for on-sun measurements**

This section describes the design and construction of the collimating tube (CT) and dark compartment used to mitigate stray light that we found to over-rate STH efficiency by a factor of 1.17 (16.1% vs. 13.8% in Figure 2.1.6). Furthermore, CTs are used in on-sun measurements when a direct solar spectrum is desirable, as for characterization of devices intended to operate

under concentration where the diffuse component of the solar spectrum is not collected. Current work is limited to 1-sun direct illumination while future work will consider concentration at 10-100x. CTs may also be called occulting tubes because they simply occlude the indirect (global) component of radiation rather than acting as a lens. The device field of view (FOV) is thus limited by the CT to the direct solar radiation plus some amount of circumsolar radiation depending on design geometry. The CT is mounted at the front of a dark compartment that houses the PEC cell, which is exclusively illuminated through the CT (Figure 2.2.1).

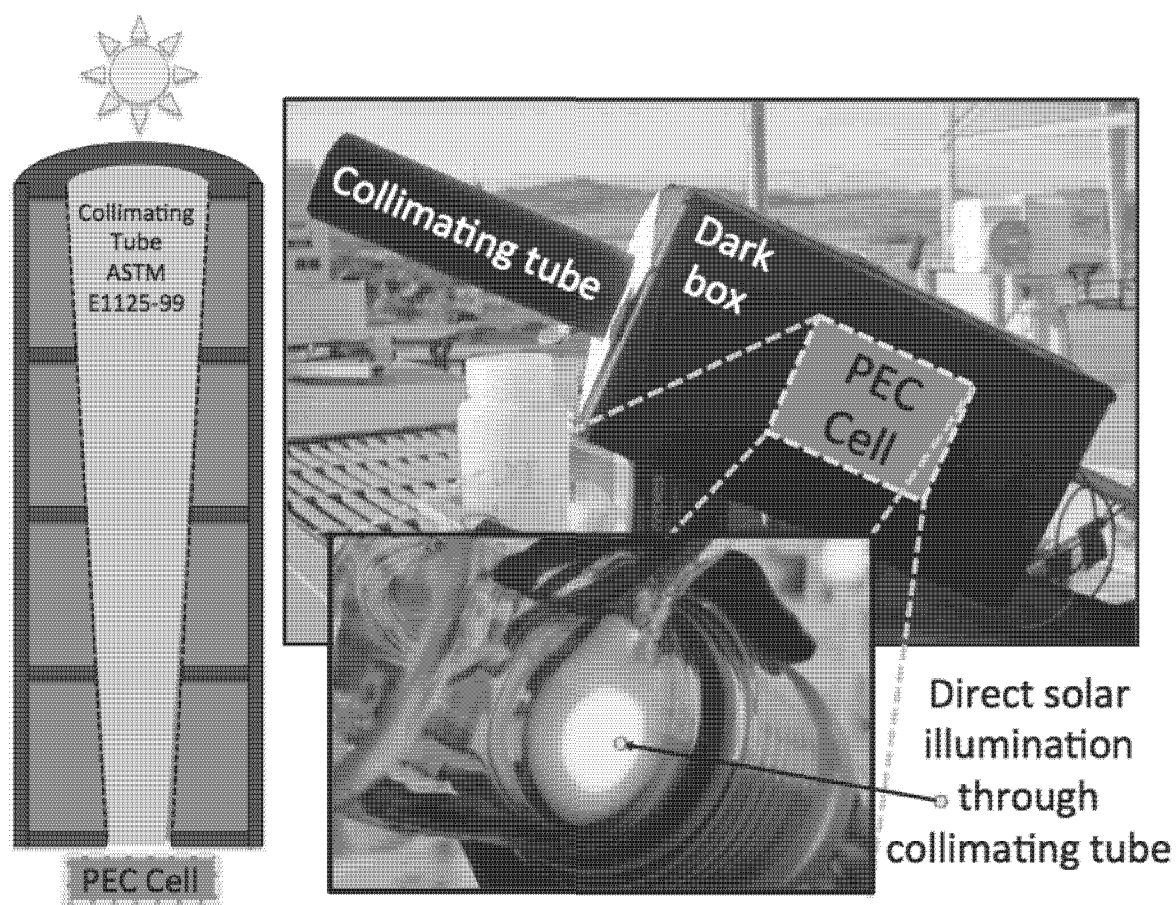


Figure 2.2.1: Picture of a collimating tube during on-sun characterization with a cross-section schematic at the left. The PEC cell inside the dark box is shown in the inset image with the well-defined, collimated beam of sunlight hitting the back of the PEC cell. The sample was removed for this picture to emphasize the uniformity of illumination.

The CT houses a set of evenly spaced washer-like baffles with inner diameters that increase incrementally with proximity to the sun. The largest baffle defines the limiting aperture and the smallest defines the receiving aperture (Figure 2.2.2). The baffles and inner surfaces are painted matte black to minimize coupling of indirect light through the tube by internal reflections. The parameters that define the CT geometry are shown in Figure 2.2.2.

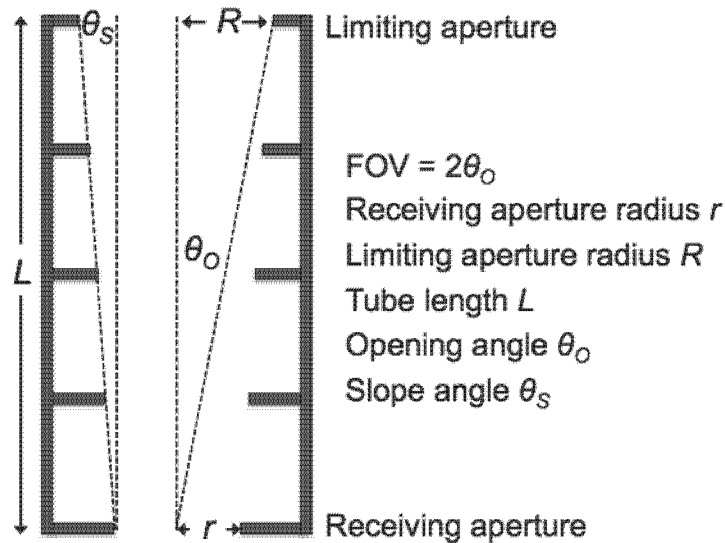


Figure 2.2.2: Schematic of collimating tube with design parameters labeled and defined

The device placed beneath the receiving aperture has a FOV twice the opening angle  $\theta_o$  and is related to the limiting aperture radius  $R$  and the tube length  $L$  by

$$\frac{1}{2}\text{FOV} = \theta_o = \tan^{-1} \frac{R}{L}. \quad 2.2.1$$

The slope angle  $\theta_s$  is given by

$$\theta_s = \tan^{-1} \frac{R-r}{L} \quad 2.2.2$$

where  $r$  is the receiving aperture radius and the limit angle  $\theta_L$  is

$$\theta_L = \tan^{-1} \frac{R+r}{L}. \quad 2.2.3$$

Specifying two of  $\theta_o$ ,  $\theta_s$ , or  $\theta_L$  is necessary and sufficient for complete CT design, of which

$\theta_o$  and  $\theta_s$  are typically used [6]. A  $5^\circ$  FOV ( $\theta_o = 2.5^\circ$ ) is common and used in the radiometers at the Solar Radiation Research Facility (SRRL) where we perform on-sun PEC measurements and obtain reference irradiance data that is publicly available ([www.nrel.gov/midc/srrl\\_bms/](http://www.nrel.gov/midc/srrl_bms/)).

Cannon [7] recommends  $\theta_s \approx 1\text{-}2^\circ$ , but uses  $\theta_s < 0.5^\circ$  to keep tube size small for portability. For CT fabrication convenience, we use baffle inner diameters increments of  $1/16''$  as commonly available in punch or drill bit sets and let  $2R = 3/4''$  and  $2r = 1/2''$ . These and the remaining CT design parameters calculated from Equations 2.2.1-2.2.3 are shown in Table 2.2.1.

Table 2.2.1: CT design for  $5.0^\circ$  FOV with baffle diameter increment of  $1/16''$  from  $1/2''$  to  $3/4''$

FOV	$r$ (cm)	$R$ (cm)	$L$ (cm)	$\theta_o$	$\theta_s$	$\theta_L$
$5.0^\circ$	0.64	0.95	22	$2.5^\circ$	$0.83^\circ$	$4.2^\circ$

Five baffles were punched from  $\sim 1$  mm thick black PPE sheet stock having inner diameters of  $1/2''$ ,  $9/16''$ ,  $5/8''$ ,  $11/16''$ , and  $3/4''$  (all with  $1.5''$  outer diameter) and mounted with hot glue at uniform spacing inside a  $1.5''$  inner diameter black PPE tube that had been cut to  $8.6''$  length. All inner surfaces were spray-painted matte black.

The full CT unit pictured in Figure 2.2.1 (PEC cell, dark box, CT) would be mounted preferably on a solar tracker so that the unit follows the sun, but manual realignment between measurements of short duration can suffice. Chai [6] suggests a tracking accuracy (alignment) of  $2^\circ$  or better. To ensure alignment, we draw a circle concentric to the collimating tube on a piece of white paper as shown in Figure 2.2.3 and point the CT unit so that the CT shadow falls within the alignment circle. To ensure  $1^\circ$  or better alignment, the circle is drawn  $1.7$  mm from the CT since the plane of the paper is  $10$  cm behind the CT tip (limiting aperture).

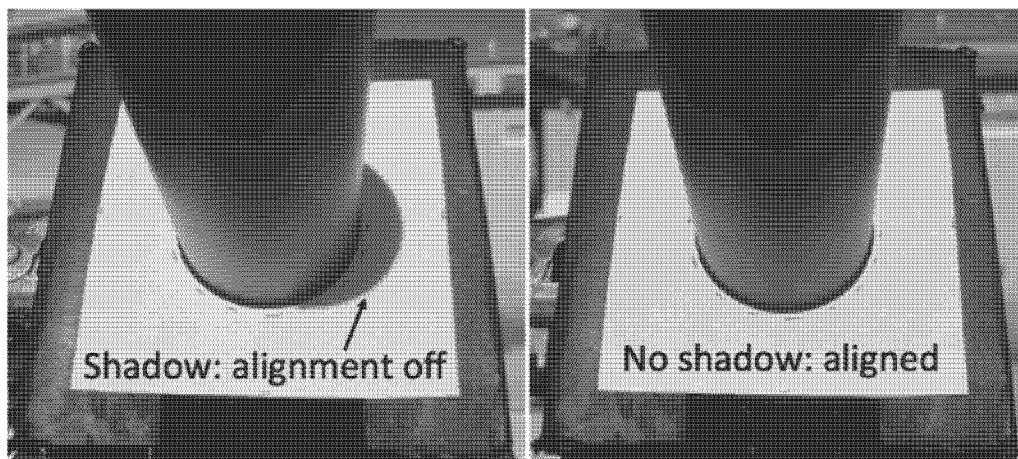


Figure 2.2.3: Front view of collimating tube and dark box with an alignment circle (dashed line) drawn on white paper. The shadow falling outside of the alignment circle indicates misalignment

As an alternative to real-time spectral data, two identical CTs may be constructed and mounted to move in concert. A calibrated reference cell can be placed behind one CT to log solar intensity while PEC characterizations are performed using the illumination defined by the other CT. All calibrated reference cell values, regardless of their type, should be in agreement in an on-sun measurement, allowing any type to be used

### **Two-source solar simulator design**

Measurements performed using direct on-sun illumination are nearly ideal, but come with added complexity of solar tracking, inclement weather (including clouds or haze), and equipment portability. For these reasons, solar simulators and indoor measurements can be preferable. In Chapter 2.1, we discussed the importance of using calibrated reference cells to set the light intensity when characterizing photoelectrodes with one band gap. A tandem photoelectrode having two band gaps that absorb within different spectral bands requires simultaneous calibration of two spectral ranges. In Chapter 2.1, we demonstrated that failure to do so caused

STH efficiency to be overrated by a factor of 1.35 (21.8% vs. 16.1% in Figure 2.1.6). In this measurement, the photon flux was calibrated for the GaInP<sub>2</sub> top junction while the current-limiting GaAs junction was incidentally over illuminated by the red-rich tungsten-halogen (W) lamp spectrum. Thus, it is necessary to accurately replicate the solar spectrum over relevant photon energies - those higher than absorber band gap(s) - when characterizing tandem devices. For later discussion, we note here that the W spectrum above ~800 nm, when appropriately scaled, is a reasonable match to the AM 1.5G reference spectrum (Figure 2.1.1).

Many traditional solar simulators, primarily designed for Si solar cells, use a xenon arc-lamp bulb whose output spectrum (Figure 2.1.1) has a set of very strong emission lines between 800-1000 nm as well as some output below 350 nm where there are no photons in the AM 1.5 G reference spectrum. Solar simulators may use what is called an "AM 1.5 G filter" to mitigate these excess spectral features. The transmittance of one such filter is designed to be low in the 800-1000 nm range and have a UV cut-off at ~350 nm (black line, Figure 2.2.4).

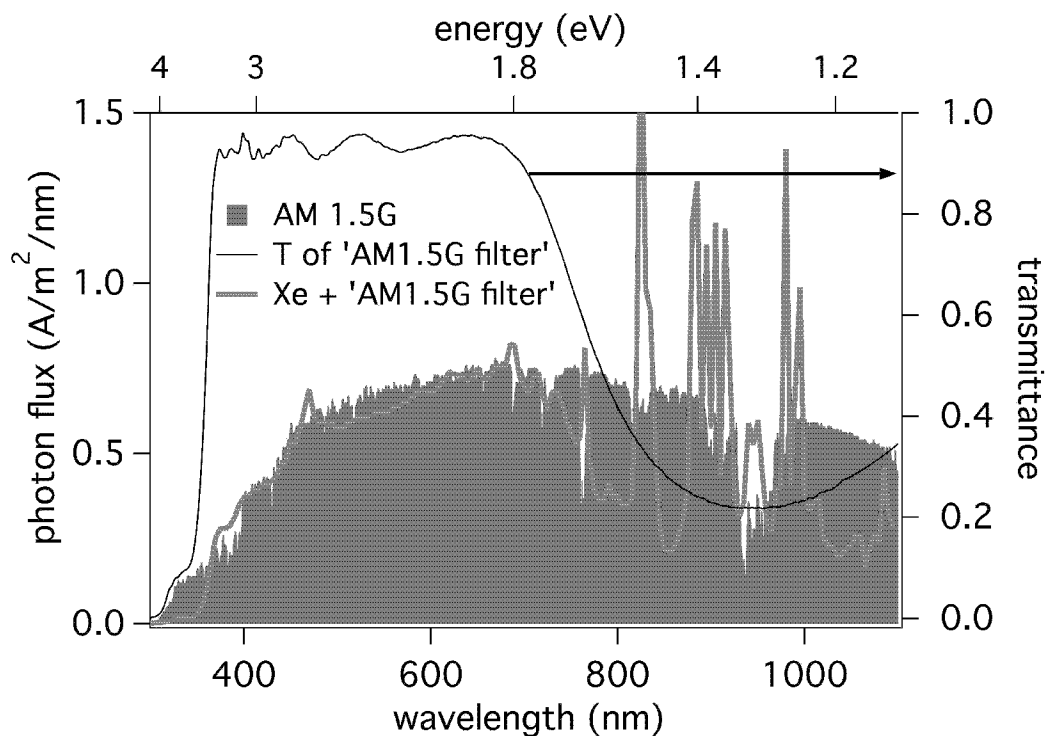


Figure 2.2.4: The AM 1.5 G reference spectrum is shown (filled gray) with the spectrum of a Xe arc lamp when passed through an "AM 1.5G filter" (pink line). The measured transmittance of the "AM 1.5G filter" (black line) is plotted vs. the right axis.

The low transmittance region (20-30% over 800-1100 nm) attenuates the emission lines by 70-80% but the flux density (purple line) is still highly variable within small wavelength ranges. Regardless, this simulator can still have the highest "class A" rating because the rating system is based on matching the cumulative photon flux within 100-200 nm wide spectral bins to that of the AM 1.5G reference spectrum [8]. However, the large peaks in the spectrum will lead to significant measurement error when comparing samples having slightly different band gaps within the 800-1000 nm range. This simulated spectrum is not suitable for development of tandem III-V devices that progress by replacing the GaAs bottom absorber (1.4 eV, 875 nm) with InGaAs (1.2 eV, 1030 nm). We note that below  $\sim 700$  nm, the filtered Xe source (pink line, Figure 2.2.4) is an excellent match to the AM 1.5G reference spectrum. Therefore, the solar spectrum may be simulated smoothly by filtering out a Xe source cut off above  $\sim 700$  nm to completely remove the emission line variability and combining with a W source cut off below  $\sim 700$  nm. Furthermore, the necessary Xe UV cut off below  $\sim 350$  nm can be replicated by a piece of glass or a glass-based optical element, making the relatively expensive 'AM 1.5G filter' unnecessary.

The following describes our approach to designing a two-source Xe-W solar simulator. We screened a set of  $\sim 20$  cut-off filters by measuring their spectral transmittance functions and applying to raw Xe and W spectra. When the filtered spectra are scaled and added, the combination that best matches the AM 1.5 G spectrum is a KG-5 filter (Schott) for Xe and 615 nm long-wavelength pass (LWP) filter for W. The raw Xe (blue dashed) and W (red dashed) spectra are shown in Figure 2.2.4 and the corresponding spectra for each with their

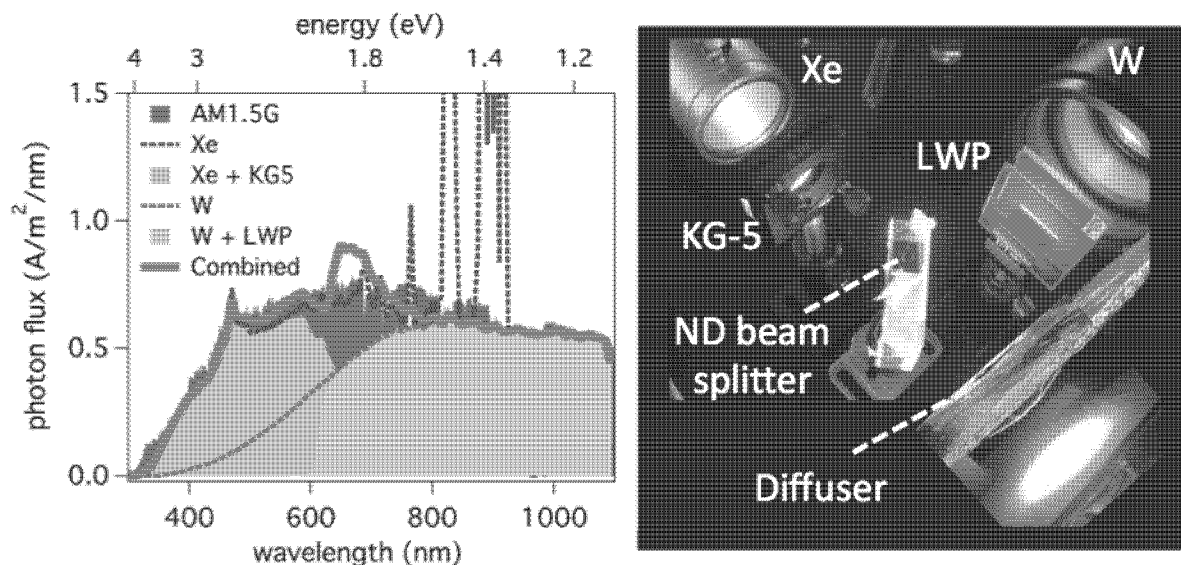


Figure 2.2.5: Raw Xe (blue dashed) and W (red dashed) spectra are plotted on top of the AM 1.5 G reference spectrum (gray filled). The Xe and W spectra shaped by KG5 (blue filled) and LWP (red filled) filters respectively are combined (green line) to simulate the AM 1.5G spectrum. The right image shows the Xe and W sources placed at right angles, combined spatially with a beam splitter, and then passed through a light-shaping diffuser resulting in the uniform white illumination spot shown at the lower right.

respective filters are shown (scaled) as the filled blue (Xe + KG5) and red (W + LWP) regions.

In practice, Figure 2.2.4b shows how the two filtered sources are combined by placing at a right angle to each other and with a neutral density (ND) filter placed at 45° angle to each serving as a beam splitter (combiner). The Xe component transmitted through the ND filter is aligned with the W component reflected by the ND filter then both pass through a light-shaping diffuser (Newport) to reduce spatial non-uniformity. The intensity of each source is adjusted individually so that both GaInP<sub>2</sub> (1.8 eV) and Si (1.1 eV) reference cells read their calibration values. This ensures that the cumulative photon flux above both 1.8 eV and 1.1 eV match that of the AM 1.5G reference spectrum. We use the calibrated spectroradiometer to measure the resulting spectrum (green line) to confirm spectral match and without significant deviation from AM 1.5G.

The largest spectral discrepancy between this simulator and AM 1.5G occurs within a ~50 nm wide absorption band centered around ~950 nm (Figure 2.2.4) caused by water vapor in the atmosphere. A similarly shaped band is removed when light transmits through liquid electrolyte as in all PEC cells [9], which is expected to minimize this discrepancy. The second largest discrepancy occurs where the filtered Xe and W spectra are "stitched" together. The set of filters evaluated was not exhaustive so some improvement, although marginal, may be made with optimal filter selection. Regardless, the match to the AM 1.5 G reference spectrum exceeds other "class A" rated solar simulators and more importantly does so with a smooth spectrum that mitigates the potential measurement error of discontinuous, single Xe source solar simulators.

## **2.3 Photoelectrode mounting and compression cell design**

This section presents construction of epoxy-mounted photoelectrodes (EMP) followed by a discussion of issues associated with their use, the most dire being poor area definition that caused STH efficiency to be over-rated by a factor of 1.48 (13.8% vs. 9.3% in Figure 2.1.6). We propose EMP construction best practice to ensure proper illuminated area definition and then introduce a PEC compression cell as an alternative mounting apparatus.

### **Traditional epoxy-mounted photoelectrode (EMP)**

Photoelectrodes generally consist of a semiconductor absorber film having the "front" surface contacting electrolyte and the other with an Ohmic back contact to collect current. The back contact is connected to a potentiostat through a metal wire lead that also serves as a convenient handle. Conductive Ag paint ensures conductivity between the back contact and wire lead. Epoxy (Hysol 9462, as in Chapter 2.1) is applied to isolate the back contact, wire, and

photoelectrode sides to prevent shorting. A portion of the surface perimeter is also covered to ensure complete coverage of the sides and improve adhesion. Only the remaining photoelectrode

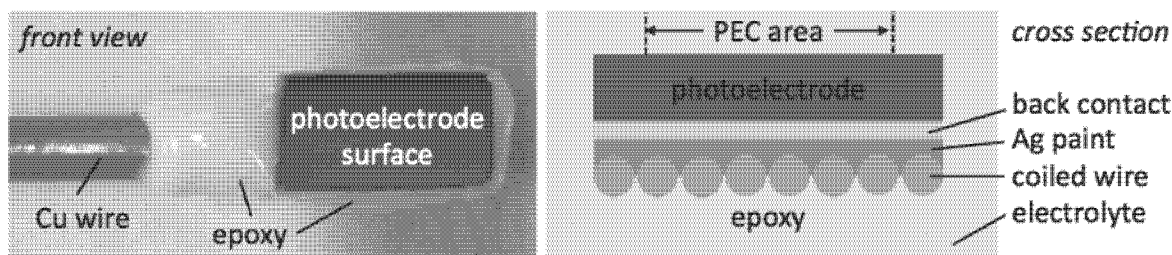


Figure 2.3.1: Picture of epoxy-mounted photoelectrode and cross section schematic

surface is exposed to form a PEC junction in electrolyte (Figure 2.3.1). The PEC junction area of these traditional EMPs is quantified using ImageJ software to analyze a scanned image where the PEC junction area is defined by the region not covered with epoxy [10].

The identified issues associated with EMPs are linked to characteristics of the epoxy: 1) partial transparency, 2) swelling, 3) adhesion failure, 4) reduced Faradaic efficiency, and 5) difficult removal for post-analysis. The degree to which these issues exist for other epoxies is unknown. We describe our observation and/or measurement of each for the commonly used Hysol 9462 epoxy as an outline that may be used to evaluate others:

1) Partial transparency: When photocurrent measurements exceed theoretical expectations (see Chapter 3.2), epoxy transparency was suspected. Light transmitted through the epoxy and collected as current overrates STH as the result of the epoxy poorly defining the active area. To characterize its transmittance, epoxy was applied between pairs of glass slides with spacing with spacers between to define the epoxy thickness. The measurements (Figure 2.1.7) are for uniform epoxy thickness, however, the coverage and uniformity of manually applied epoxy introduces sample-to-sample variability. Thus, partial transparency adds variability when comparing among photoelectrodes, in addition to over-rating STH efficiency. We found that Hysol 9462 transmittance can be drastically reduced when  $\text{TiO}_2$  powder is mixed

in, which may be a suitable mitigation strategy. A 2:1 ratio of epoxy:TiO<sub>2</sub> reduces transmission by ~10x while still having workable viscosity.

2) Swelling: Permeable epoxy will absorb electrolyte resulting in volume expansion that can become evident for long measurements (e.g. durability testing). We observed small decreases in photocurrent density after 24-hour durability testing, usually attributed to degradation, but a portion can be caused by decreased photoelectrode area. Re-measuring after testing revealed decreases of up to 15%, being more pronounced for smaller areas, which we attribute to the occlusion of more active area by swollen epoxy.

3) Adhesion failure: For longer durability testing periods (>100 hr), the epoxy adhesion to the photoelectrode surface may start to fail. Complete failure occurs when electrolyte seeps under the epoxy, reaches the back contact (or other metallic pathway), and creates a short circuit that becomes evident as dark current in IV measurements. Post-inspection shows a gap between the epoxy and photoelectrode surface and considerable corrosion beneath the epoxy.

4) Reduced Faradaic efficiency ( $\eta$ ): For  $\eta = 100\%$ , the quantities of desired electrolysis products (H<sub>2</sub> and O<sub>2</sub>) agree with the current passed through the electrochemical circuit [2]. Performing electrolysis at 10 mA/cm<sup>2</sup> using Pt foil electrodes in a Hoffman apparatus (voltmeter), we measured  $\eta$  for O<sub>2</sub> of 60-80% revealing parasitic oxidation reactions when epoxy is used. However,  $\eta$  was close to 100% efficiency at 80 mA/cm<sup>2</sup>, indicating current density (operating voltage) and/or time dependence; the latter because total charge passed was constant meaning shorter run time at higher current densities.

5) Difficult removal for post-analysis: The techniques used to evaluate durability (see Chapter 4.1) necessitate electrode deconstruction and epoxy removal. Hysol 9462 can be removed with forceps after being embrittled by heat gun treatment, but surface transformation is

likely induced at elevated temperature. Instead, the PEC compression cell described in the next section can be used as an alternative to epoxy.

Despite these issues, EMPs can be convenient. For short measurements not requiring post-analysis, such as the IV measurements performed throughout Chapter 3, issues 2-5 are mitigated. To minimize issue 1) partial transparency, we use an area definition equal to the full device area - the sample area measured before applying epoxy - while using transparent or minimal coverage of partially transparent epoxy. Here, the maximum error associated with the area definition is the ratio of the full device area to the epoxy-defined area and the error is minimized by higher epoxy transmittance.

### **Compression cell design**

The critical design requirement for PEC compression cell is a reliable yet removable seal to photoelectrode surfaces. Rubber washers or O-rings made of Viton<sup>®</sup> or fluorosilicone [10] [11] have been used. We select Kalrez<sup>®</sup> material for its exceptional chemical resistance and availability as sheet stock (0.8 or 1.2 mm thick) from which we punch out custom-sized washers. The punched washer cross section is rectangular rather than circular, which eliminates void space where the washer contacts the sample so that the electrochemically active area matches the illuminated area. The Kalrez<sup>®</sup> washer is black and opaque confining the illuminated area precisely to its inner diameter. Still, sample dimensions may be larger than the washer outer diameter (Figure 2.3.2 inset), so we shade the perimeter with metal foil placed around the Kalrez<sup>®</sup> washer (Figure 2.3.3). The glass compression cell body has an opening that matches the washer inner diameter and concentric recess matching the outer diameter that maintains its position. The washer is placed in the recess followed by the sample and then a spring-loaded Au-

plated stainless steel plunger is screwed into place to provide compressive force and electrical connection to the photoelectrode back contact (Figure 2.3.2). The compression enforces a seal between the glass-Kalrez<sup>®</sup> and Kalrez<sup>®</sup>-photoelectrode surfaces simultaneously. The spring provides constant force, maintaining the seal even if the assembly or washer relaxes over time while limiting excessive force that could damage or crack samples. The cell body is filled with electrolyte while reference and counter electrodes are inserted through separate ports to complete the PEC compression cell setup.

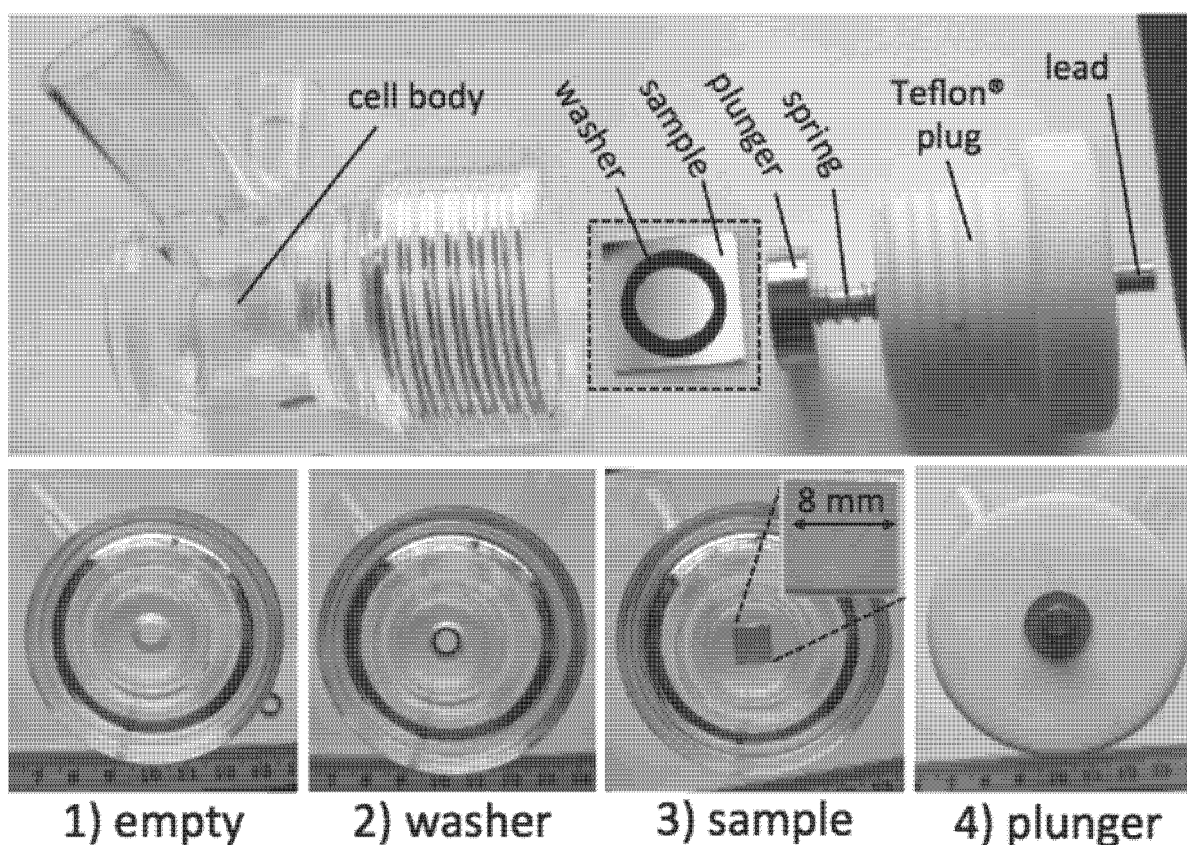


Figure 2.3.2: The individual compression cell components (top) with an inset (3x enlarged) of the washer placement on a sample. The assembly sequence (1-4) is performed with the cell window facing down on a horizontal surface.

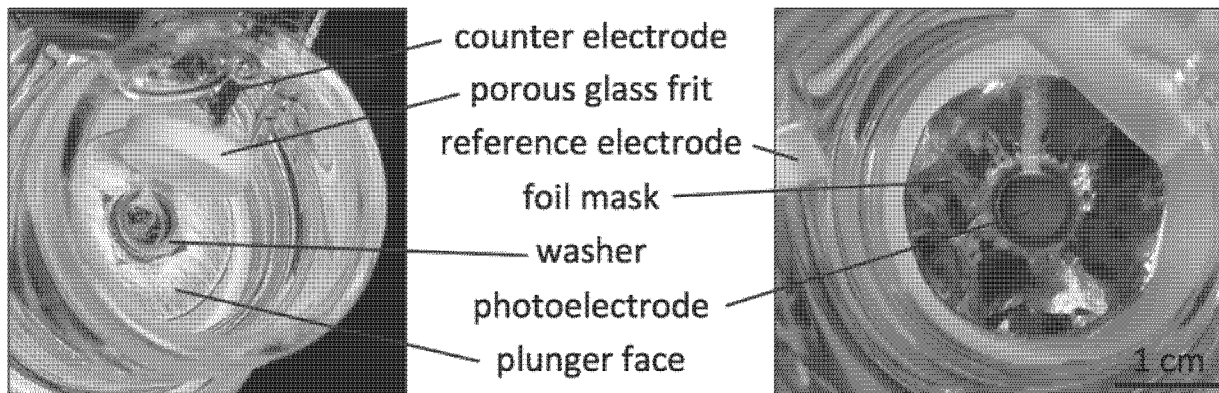


Figure 2.3.3: An operating photoelectrode evolving hydrogen bubbles viewed through the PEC compression cell front window. On the left, the foil mask was left out so that the full sample and plunger face are visible through the cell body back glass wall. On the right, the foil mask shades the sample perimeter, confining illumination to the washer inner diameter.

An additional feature of this cell is a removable counter electrode compartment consisting of a glass tube with porous frit at one end. This feature was implemented to mitigate solution yellowing caused by anodic degradation of surfactant [12], added to help clear bubbles from the photoelectrode surface that, when stuck, can degrade performance and accelerate corrosion [13]. Yellowing (observable after a few hours of operation) influences light transmission, so we prevent it by confining the surfactant to the working electrode (photocathode) compartment with the glass frit. Although some crossover is expected, no yellowing has been observed using this configuration even after weeklong durability tests. One electrode port is angled so that the tube, when inserted, allows the counter electrode to be placed closely to the photoelectrode, minimizing the solution conduction pathway. The separate compartments can also facilitate gas collection and quantification for Faradaic efficiency measurements.

There are a few disadvantages of this compression cell in its current form. Some skill is required to properly position samples and carefully engage the plunger without breaking brittle,

crystalline photoelectrodes. The washer thickness (0.8 mm) forms a lip where some hydrogen bubbles collect at the top of the photoelectrode (visible in Figure 2.3.3). After 24-h durability tests the region under the bubbles shows little etching (e.g. samples B12, B22 in Figure 4.3.6 and 4.3.7), perhaps from lower local solution transport and thus current density. This observation is not well understood, but inhomogeneity caused by the bubbles is evident. The washer diameter requires minimum sample dimensions. Crystalline-based photoelectrodes that cleave along atomic planes have rectangular geometry leading to a minimum excess of  $(2r)^2 - \pi r^2$  outside the circular washer-defined area of radius  $r$ . Furthermore, the excess area is in the dark, which is a concern when optimizing photovoltage. Open-circuit voltage has a logarithmic dependence on the ratio of light to dark current [14] and shaded device area increases dark current.

*Preliminary compression cell construction and design is credited to Yehor Novikov (Integrated Instrument Development Facility at CU-Boulder). Multiple subsequent iterations were developed in collaboration with Precision Glass Blowing (Englewood, CO).*

## 2.4 Measuring the spectral response of tandems

In Chapter 2.1 we showed how IPCE data (Figure 2.1.4) is used to validate STH efficiency measurements and diagnose device performance. When integrated over a solar reference spectrum flux, the expected photocurrent density is obtained which should be consistent with measurements under solar-simulated white light. IPCE is measured as the current response to a small monochromatic illumination signal, ideally under conditions of 'white bias light' that simulate 1 sun. However, two distinctions between PV and PEC devices can preclude such measurements: Capacitance in electrochemical systems introduces transients that can over-rate response and sporadic hydrogen bubble formation/detachment causes current noise that

makes detecting the monochromatic signal difficult [10]. Thus, PEC IPCE is measured at pseudo-steady state to ensure stable current and without white bias light to avoid noise.

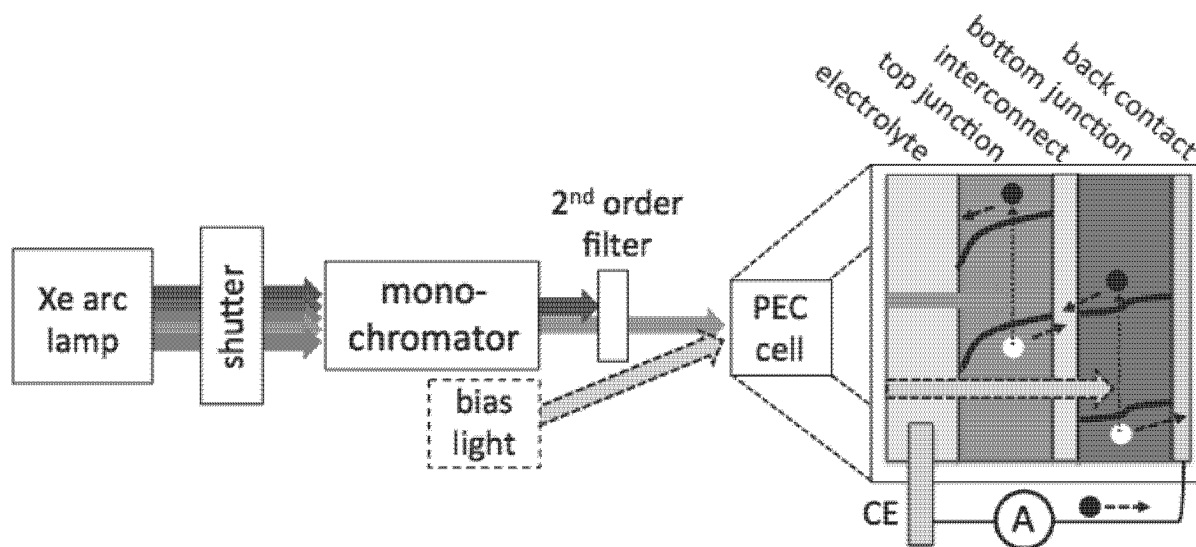


Figure 2.4.1 Schematic of system components for spectral response measurements. Series-connected tandems require additional bias illumination to current-match the junctions.

In series-connected tandems, monochromatic light is absorbed in one junction causing the other to current-limit the device to 0 net current. We overcome this by providing fixed, single-wavelength diode illumination to one junction at sufficient flux so that the other, absorbing monochromatic light, is current limiting and determines the measured response. In Chapter 3, we present GaInP<sub>2</sub>/GaAs and GaInP<sub>2</sub>/InGaAs tandem IPCE. An 808 nm diode selectively illuminates GaAs (or InGaAs) when measuring GaInP<sub>2</sub> and a 532 nm diode illuminates GaInP<sub>2</sub> when measuring GaAs (or InGaAs).

We note here that the photodiode should not be placed within the PEC cell when taking calibration measurements. First, IPCE is intended to represent *external* quantum conversion. Second, two air/glass interfaces exist at the window of a dry PEC cell. When filled with electrolyte, reflection at the inner is largely negated, and IPCE will be overrated by ~5%. Chapter 3.2 further discusses reflection in PEC cells. We also note that IPCE-derived current

estimates an upper limit of device performance because it is measured at low current density, much below the appropriate load of maintaining the water-splitting reaction [2].

IPCE can be divided into a series of processes, each with their own yield, that include charge generation, transport, and transfer [2]. Charge generation is the result of absorption occurring for photons with energy greater than the semiconductor band gap. For sufficient thickness, all incident photons will be absorbed except those reflected at the semiconductor surface. Reflection can be deconvoluted from IPCE to yield internal quantum efficiency (IQE), also called absorbed photon-to-current efficiency (APCE) as:

$$APCE = IQE = \frac{IPCE}{Reflectance}$$

For inverted tandems having a back reflector (Chapter 3), reflectance is modulated by the thickness of the device due to thin film interference. Also, photons having energy lower than both band gaps enter the device, but nearly all are reflected back out. Both effects add complexity beyond the reflection occurring at the front surface. IQE is a diagnostic efficiency of charge transport and transfer/collection, meaning that photons entering but then exiting the device contributed to reflectance.

## References

- [1] “ASTM G173-03, Standard Tables for Reference Solar Spectral Irradiances: Direct Normal and Hemispherical on 37° Tilted Surface, ASTM International, West Conshohocken, PA, 2003, [www.astm.org](http://www.astm.org).”
- [2] Z. Chen, T. F. Jaramillo, T. G. Deutsch, A. Kleiman-Shwarsstein, A. J. Forman, N. Gaillard, R. Garland, K. Takanabe, C. Heske, M. Sunkara, E. W. McFarland, K. Domen, E. L. Miller, J. a. Turner, and H. N. Dinh, “Accelerating materials development for photoelectrochemical hydrogen production: Standards for methods, definitions, and reporting protocols,” *J. Mater. Res.*, vol. 25, no. 01, pp. 3–16, 2010.

- [3] K. A. Bertness, S. R. Kurtz, D. J. Friedman, A. E. Kibbler, C. Kramer, and J. M. Olson, "29.5%-efficient GaInP/GaAs tandem solar cells," *Appl. Phys. Lett.*, vol. 65, no. 8, p. 989, 1994.
- [4] O. Khaselev and J. A. Turner, "A Monolithic Photovoltaic-Photoelectrochemical Device for Hydrogen Production via Water Splitting," *Science (80-. )*, vol. 280, no. 5362, pp. 425–427, 1998.
- [5] "NREL-SRRL, [http://www.nrel.gov/midc/srll\\_bms/](http://www.nrel.gov/midc/srll_bms/)."
- [6] A. Chai, "Some basic considerations of measurements involving collimated direct sunlight." Lewis Research Center, National Aeronautics and Space Administration, Cleveland, OH, pp. 233–246, 1976.
- [7] T. W. Cannon, "Spectral solar irradiance instrumentation and measurement techniques," *Sol. Cells*, vol. 18, pp. 233–241, 1986.
- [8] K. Emery, "Solar simulators and I–V measurement methods," *Sol. Cells*, vol. 18, no. 3–4, pp. 251–260, 1986.
- [9] H. Döscher, J. F. Geisz, T. G. Deutsch, and J. A. Turner, "Sunlight absorption in water – efficiency and design implications for photoelectrochemical devices," *Energy Environ. Sci.*, vol. 7, no. 9, pp. 2951–2956, 2014.
- [10] Z. Chen, H. N. Dinh, and E. Miller, *Photoelectrochemical Water Splitting: Standards, Experimental Methods, and Protocols*. 2013.
- [11] E. Verlage, S. Hu, R. Liu, R. J. R. Jones, K. Sun, C. Xiang, N. S. Lewis, H. A. Atwater, Jr., and H. A. Atwater, "A Monolithically Integrated, Intrinsically Safe, 10% Efficient, Solar-Driven Water-Splitting System Based on Active, Stable Earth-Abundant Electrocatalysts in Conjunction with Tandem III-V Light Absorbers Protected by Amorphous TiO<sub>2</sub> Films," *Energy Environ. Sci.*, pp. 1–13, 2015.
- [12] T. G. Deutsch and J. A. Turner, "Semiconductor Materials for Photoelectrolysis: 2014 U.S. DOE Hydrogen & Fuel Cells Program Review," 2014.
- [13] T. G. Deutsch, C. a. Koval, and J. a. Turner, "III-V nitride epilayers for photoelectrochemical water splitting: GaPN and GaAsPN," *J. Phys. Chem. B*, vol. 110, no. 50, pp. 25297–25307, 2006.
- [14] M. A. Green, *Solar Cells*. 2013.

## 3. Tandem III-V semiconductor devices for water splitting

### 3.1 Toward the maximum efficiency with III-Vs

Techno-economic analysis has shown that STH efficiency most significantly influences the cost of hydrogen produced by solar water splitting [1]. Döscher et al. [2] calculated STH for tandem devices for a range of top band gap  $E_g^{top}$  and bottom band gap  $E_g^{bottom}$  combinations, showing that ~25% STH can be achieved with a 1.8/1.0 eV  $E_g$  combination. The seminal work demonstrating water splitting with III-Vs, used a tandem having top GaInP<sub>2</sub> (1.8 eV) and bottom GaAs (1.4 eV) junctions [3]. In Ch. 2, we showed that GaAs junction, being filtered by GaInP<sub>2</sub>, limited the device to less than 10% STH. However, Figure 3.1.1 shows that for  $E_g^{top}=1.8$  eV and  $E_g^{bottom}=1.4$  eV, 15% is achievable (Figure 3.1.1, dashed line). In Ch. 3.1, we show that this discrepancy is largely from reflection losses, which we seek to address in Ch. 3.3 through anti-reflection coating (ARC) design. ARCs are an optimization measure, increasing the actual performance of a specific device design toward its theoretical performance. To increase theoretical performance, a greater portion of the solar spectrum must be accessed. This is done by decreasing a tandem's lower band gap. Substituting a lower bandgap absorber for GaAs also addresses the issue of it being current limiting. Work here focuses on development and characterization of devices having an InGaAs bottom junction ( $E_g^{bottom}=1.2$  eV). Arrows indicate in Figure 3.1.1 indicate the associated progress toward theoretical maximum STH

efficiency. However, InGaAs is not lattice-matched to GaInP<sub>2</sub> like GaAs, and so GaInP<sub>2</sub>/InGaAs tandems require considerably different growth and processing techniques.

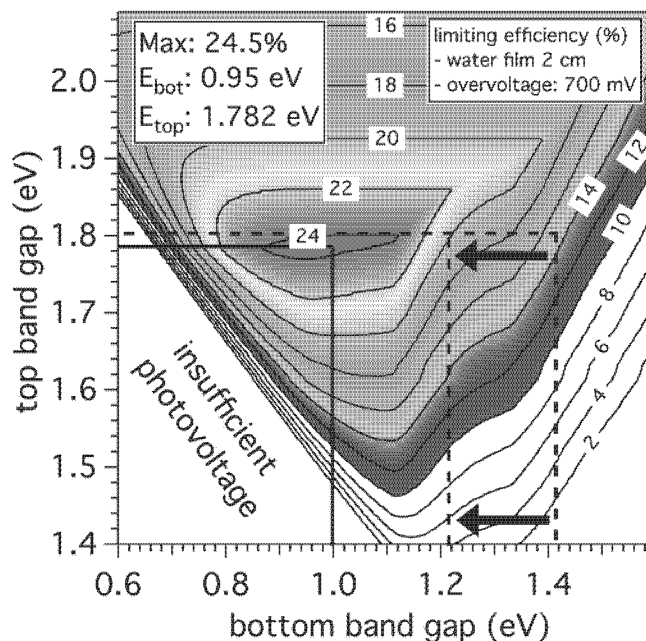


Figure 3.1.1: STH iso-efficiency contour plot shows 24.5% STH can be reached with a 1.8/1.0 eV  $E_g$  combination. STH calculation credited to Henning Döscher, NREL.

Flexibility to monolithically combine non-lattice matched absorbers is enabled by an inverted metamorphic multijunction (IMM) device architecture. The metamorphic growth stage introduces a gradient in lattice constant that tends to initiate defects that can propagate into the top junction. Growing the device inverted, top GaInP<sub>2</sub> junction first on GaAs substrate, eliminates defect propagation concerns [4]. In our work, the GaAs substrate is etched from the device, but adoption of methods [5] to instead remove the device and re-use the substrate would result in significant cost reductions [6].

The PEC tandem structures were grown by the III-V group at NREL using atmospheric-pressure organometallic vapor phase epitaxy (OMVPE). Figure 3.1.2 shows the growth structure of IMM devices where the p-GaInP<sub>2</sub> photocathode is first grown epitaxially on a GaAs substrate

that is connected to the p/n-GaAs PV cell by a tunnel junction. An Ohmic back contact is electrodeposited on the PV cell which is then attached with epoxy to a Si wafer that serves as a handle. After the GaAs substrate is etched away, the p-GaInP<sub>2</sub> is left exposed on what is now the top (Figure 3.1.2). Further device processing and mounting to complete a full PEC cell is discussed and illustrated in Ch. 2.3.

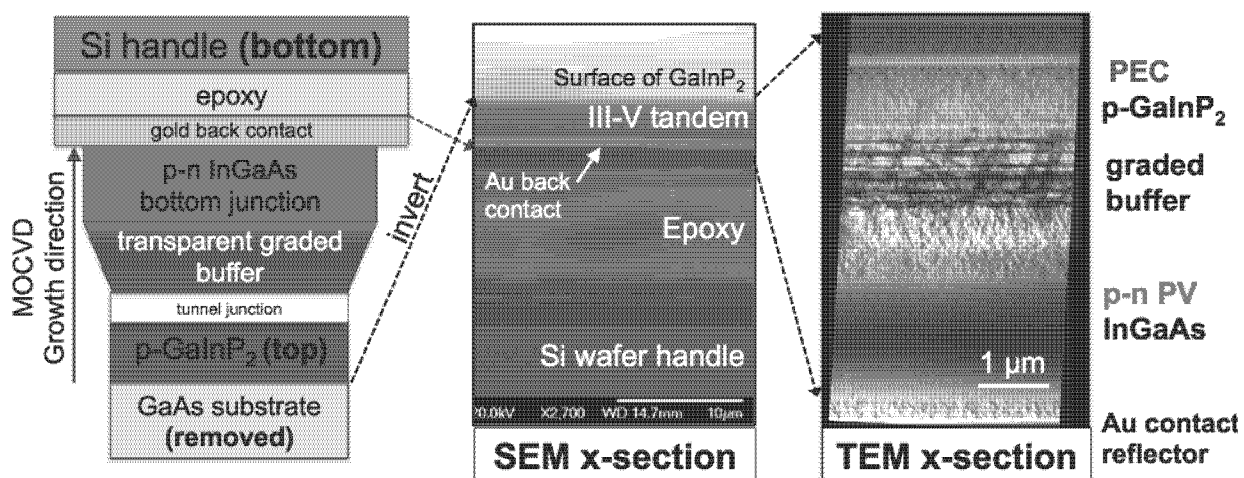


Figure 3.1.2: IMM tandem structure (left) and polished SEM (center) and TEM (right) cross-sections. TEM credit Andrew Norman, NREL.

We demonstrate progress enabled by IMM devices through spectral response (IPCE, Ch. 2.4) measurements. First, we compare a standard “upright” GaInP<sub>2</sub>-GaAs tandem to the equivalent inverted structure (not metamorphic), demonstrating gains from its back reflector. Second, we show the increased solar spectrum utilization allowed by IMM tandems with lower bottom bandgap. We integrate all IPCE data over the standard direct reference spectrum found in ASTM G173 that is scaled to 1 kW/m<sup>2</sup> per established PV convention [4], to determine the expected photocurrent density. As in PV, the primary advantage of concentration is reducing the amount and cost of III-V used. Furthermore, III-V devices generate more voltage under concentration to increase efficiency in PV devices [4]. In PEC, this extra voltage will help compensate for the higher catalytic overpotential from the higher current densities associated

with concentration. Finally, a smaller photocathode leaves more space for a larger metal anode and allows the inherently more difficult water oxidation half-reaction to proceed at lower current densities and, therefore, lower overpotential.

The solar flux (Figure 3.1.3a, line i) is plotted along with IPCE to emphasize that we seek to increase the product of IPCE and solar flux. We also plot the integrated photon flux vs. wavelength to illustrate the theoretical maximum current of a device with IPCE = 1 at all wavelengths (Figure 3.1.3b, line labeled “ $E_g$ -limited current”). This theoretical maximum assumes that every photon with  $h\nu > E_g$  is absorbed and contributes one electron to the current. All devices discussed here have a GaInP<sub>2</sub> ( $E_g = 1.81$  eV) top absorber which has a maximum theoretical current of  $\sim 19$  mA/cm<sup>2</sup>. The photons with  $h\nu < 1.81$  eV ( $\lambda > 685$  nm) pass through GaInP<sub>2</sub> and can be absorbed in the bottom junction. Thus, at  $\lambda = 685$  nm, the cumulative photon flux starts over at zero and represents the theoretical limit of a hypothetical  $E_g$  bottom junction. The two “ $E_g$ -limited current” curves cross at  $\lambda = 950$  nm (1.38 eV) and 19 mA/cm<sup>2</sup> illustrating that an  $E_g = 1.38$  eV bottom  $E_g$  would be current-matched to GaInP<sub>2</sub>. The IPCE of Figure 3.1.3a (colored data) is integrated over solar flux (line iii) as plotted in Figure 3.1.3b, and the current density expected for each junction is the value at which each line intercepts the vertical axis.

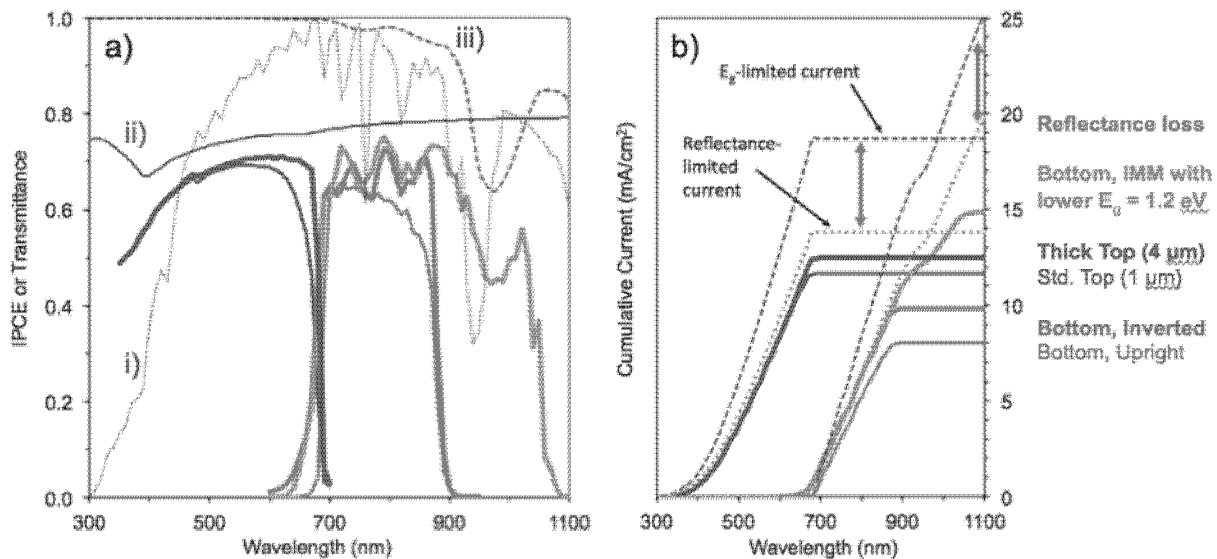


Figure 3.1.3: (a) The IPCE of two top (blue) and three bottom junctions (green and orange) from different tandem PEC device structures are overlaid on: i) direct solar flux spectrum (scaled), ii) calculated IPCE reflectance limit, and iii) transmittance through 1 cm water. Figure 3b shows the  $E_g$ -limited and reflectance-limited current (dashed) for a device with top  $\text{GaInP}_2$  and hypothetical bottom junction. (b) The IPCE is integrated over the direct solar spectrum as cumulative current vs. wavelength.

Line ii) in Figure 3.1.3a shows the reflectance-limited IPCE as calculated by the normal-incidence Fresnel equation for the interfaces of a PEC cell ( $\text{GaInP}_2$ -electrolyte, electrolyte-glass, and glass-air). A full model is presented in Ch. 3.2. We note how closely IPCE approaches the reflectance limit (line ii), meaning absorbed light is extracted as current with 90-95% efficiency and reflectance accounts for the majority of photocurrent loss.

The colored datasets in Figure 3.1.3 show IPCE for different top and bottom junction designs as noted in the legend to the right of Figure 3.3.3b. We first compare 1  $\mu\text{m}$  and 4  $\mu\text{m}$  thick p- $\text{GaInP}_2$  top junctions whose IPCE is nearly identical except in the 600-650 nm range where it is lower for the 1  $\mu\text{m}$  thickness. Its lower response to near- $E_g$  photons is a result of the long absorption length ( $\sim 1 \mu\text{m}$ ) of these photons. However, they are absorbed in the bottom junction, evidenced by a tail in its IPCE at 600-650 nm. The thin green line does not show the tail because its top junction is 4  $\mu\text{m}$  thick. When a cell is current-limited by the bottom junction,

thinning the top junction can be used to increase  $I_{sc}$ , in this case by  $\sim 1 \text{ mA/cm}^2$  as shown in Figure 3.1.3b. Regardless, a lower  $E_g$  bottom junction is necessary to increase the number of accessible solar photons.

A similar comparison is made for two bottom junctions (thin and thick green lines), but in this case, a back reflector enhances long-wavelength response. The green lines compare bottom junction performance of upright (thin green) and inverted structures (thick green). The upright structure resides on an inactive GaAs substrate to which unabsorbed photons are lost. The inverted structure has a gold back contact immediately behind the bottom junction (Figures 3.1.2) that acts as a reflector, effectively doubling its optical thickness. In addition to increasing IPCE at 800-900 nm, we see oscillations that are caused by interference within the inverted device. Figure 3.1.3b shows that a bottom GaAs junction in an inverted device reaches  $10 \text{ mA/cm}^2$  compared to  $8 \text{ mA/cm}^2$  in an upright device.

The final dataset in Figure 3.1.3 is IPCE for an IMM device with InGaAs bottom junction (orange line). Unlike the GaAs that has no response above 900 nm, the InGaAs has excellent response out to  $\sim 1050 \text{ nm}$ . The dip in IPCE centered at  $\sim 950$  is caused by light absorption in the electrolyte (line iii) and can have significant influence of PEC cell design [2]. Still, the lower bottom  $E_g$  enabled by IMM growth progresses toward the maximum STH of Figure 3.1.1; the limiting bottom-junction current of  $10 \text{ mA/cm}^2$  for GaAs is increased to  $15 \text{ mA/cm}^2$  by replacing it with InGaAs. However, the top GaInP<sub>2</sub> junction is now current-limiting at  $12.5 \text{ mA/cm}^2$ .

## 3.2 Light-limited photocurrent: Band gap and reflection

As discussed throughout Ch. 2, the complexity and precision of PEC characterization practices must advance along with the devices themselves. In this section, we improve

photocurrent density prediction, positing that this will better inform device development and confidence in measurement techniques. Döscher et al. [2] modeled in detail the levels of performance that tandem devices *could* achieve with continued development. For the classical GaInP<sub>2</sub>/GaAs tandem [3], 12.3 mA/cm<sup>2</sup> is predicted, yet, we measured (Ch. 2.1) an erroneous 17.7 mA/cm<sup>2</sup> before arriving at an IPCE-validated 7.6 mA/cm<sup>2</sup>. Predictions of what devices *could* achieve are based on the light-limited photocurrent (LLPC) associated with ideal conversion of photons with energy greater than the absorber bandgap, i.e. E<sub>g</sub>-limited photocurrent. Identifying reflection as the dominant loss mechanism in high performance III-Vs, we calculate their reflection-attenuated light-limited photocurrent (RLPC). The optical model allows conversion of reflectance, measured in air, to that of a PEC configuration. Thus, the calculated RLPC provides a more informed upper bound than the E<sub>g</sub>-limited photocurrent.

The model also allows calculation of internal quantum efficiency (IQE), referred to as absorbed photon-to-current efficiency (APCE) in PEC [7], from external quantum efficiency measurements (i.e. IPCE). For optically thick absorbers, IPCE is divided by reflectance to give APCE [8], being spectral response deconvoluted of reflectance. Thus, RLPC is equivalently stated as the physical limit that  $APCE \leq 1$ . Since high-quality III-V junctions have  $0.9 \leq APCE \leq 1$  for solar-relevant  $\lambda \geq E_g$ , RLPC accurately predicts, with limited information, the photocurrent performance of such devices. Thus, RLPC will better inform both IPCE and CLIV measurements, their cross-validation, and confidence in the techniques themselves.

### **Reflection in PEC cells**

Inherent to a PEC cell are several interfaces at which reflection attenuates light. The Fresnel equation (normal incidence) describes reflectance (R) at each interface,

$$R = \left( \frac{n_1 - n_2}{n_1 + n_2} \right)^2, \quad \text{Eq. 3.2.1}$$

where light approaches within a medium having index of refraction  $n_1$  and passes through to a second medium of  $n_2$ . We account for each PEC cell interface according to its transmittance ( $T$ ), so that the transmitted light intensity ( $I_2$ ) is written in terms of the incident ( $I_1$ ) as:

$$T = 1 - R = \frac{I_2}{I_1} \quad \text{Eq. 3.2.2}$$

Figure 3.2.1a shows a schematic the PEC interfaces compared to a reference case (Figure 3.2.1b) of light incident on the same semiconductor in air.

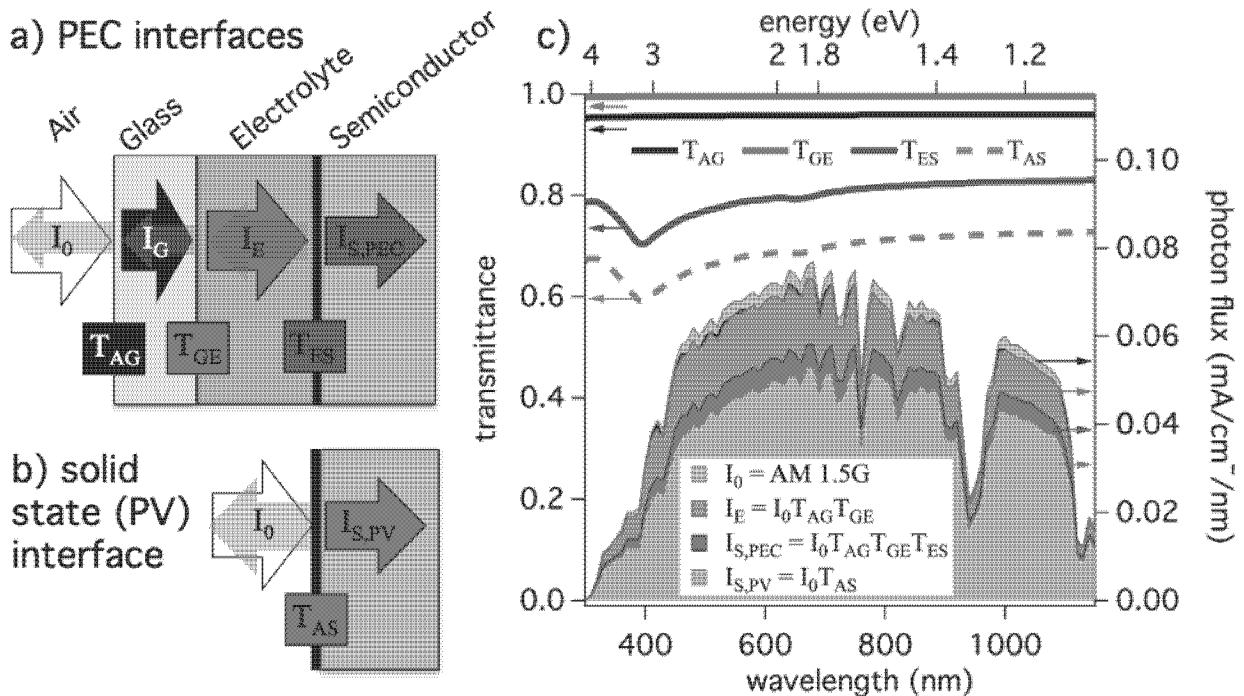


Figure 3.2.1: (a) Schematic showing the interfaces in a PEC cell where reflection at each attenuates the incident light intensity flux  $I_0$ . The transmittance through air|glass ( $T_{AG}$ ), glass|electrolyte ( $T_{GE}$ ), and electrolyte|semiconductor ( $T_{ES}$ ) attenuate  $I_0$  to give the flux entering the semiconductor  $I_{S,PEC} = I_0 T_{AG} T_{GE} T_{ES}$ . This compares to (b) the reference case of air|semiconductor ( $T_{AS}$ ) representing the configuration in which reflectance measurements are taken where  $I_{S,PV} = I_0 T_{AS}$ . (c) The spectral transmittance of each interface is plotted on the left axis using GaInP<sub>2</sub> as the semiconductor. The photon flux in each medium is plotted on the right axis for  $I_0 = \text{AM 1.5G}$ , leaving  $I_{S,PEC}$  (blue area). Integrating  $I_{S,PEC}$  over photon energies greater than bandgap gives the reflectance-limited photocurrent of GaInP<sub>2</sub>.

The spectral transmittance of each interface is shown in Figure 3.2.1c. Transmittance at air|glass ( $T_{AG}$ ) and glass|electrolyte ( $T_{GE}$ ) interfaces are virtually constant at  $T_{AG} = 0.96$  and  $T_{GE} = 0.996$ , only deviating to  $T_{AG} = 0.95$  and  $T_{GE} = 0.995$ , respectively, at the shortest wavelengths. Using optical data for GaInP<sub>2</sub> as the semiconductor ( $n_s \sim 3.2-4$ ), we also plot transmittance at the electrolyte|semiconductor interface ( $T_{ES}$ ) and compare it to that of the air|semiconductor interface ( $T_{AS}$ ). Ranging from 0.7–0.8,  $T_{ES}$  is higher than  $T_{AS}$  of 0.6-0.7 due to index-matching;  $n_E \approx 1.33$  being closer than  $n_A \approx 1.00$  to  $n_s$ . We note that secondary reflection occurs, but it is negligible. Reflection at the semiconductor (amounting to  $\sim 25\%$  of  $I_0$ ) may be reflected back towards it by a secondary reflection at the glass|air interface, having 4% reflectance. Considering another reflection loss at the semiconductor, only 0.8% of  $I_0$  could be gained by this, the largest, secondary reflection. We neglect this error, noting that it will diminish further as the semiconductor reflectance decreases, occurring when anti-reflective coatings are used (Ch. 3.4).

Last, Figure 3.2.1c also shows the photon flux (right axis) making it into each medium, using the AM1.5 G reference spectrum for  $I_0$ . We provide sample calculations relevant to GaInP<sub>2</sub>, integrating the flux above its bandgap ( $E_g = 1.8$  eV, 690 nm) to give its limiting current density: A flux of 20.1 mA/cm<sup>2</sup> is incident on the PEC cell window, establishing the bandgap-limited photocurrent of GaInP<sub>2</sub>. Reflections at air|glass, glass|electrolyte, and electrolyte|GaInP<sub>2</sub> reduce it to 19.2 mA/cm<sup>2</sup>, 19.1 mA/cm<sup>2</sup>, and finally 14.8 mA/cm<sup>2</sup>, respectively. The last is the RLPC; the photon flux that is actually absorbed by GaInP<sub>2</sub>, being 74% of the  $E_g$ -limited photocurrent. We note that the RLPC is higher for the set of PEC interfaces than for the reference air|semiconductor interface (13.3 mA/cm<sup>2</sup>), a photocurrent advantage of  $\sim 11\%$  for GaInP<sub>2</sub>.

Since GaInP<sub>2</sub> is the current-limiting absorber in the GaInP<sub>2</sub>/InGaAs tandem (Ch. 3.1), its RLPC determines the maximum photocurrent of the device. We assumed here that both the glass and electrolyte are transparent having no absorption losses, which is suitable for quartz or optical glass but only to a limited extent for the electrolyte. For GaInP<sub>2</sub>, the transparency assumption is valid for the electrolyte, being virtually transparent to photon energies above its band gap (typical electrolyte thickness < 5 cm) [2]. However, water has an absorption band centered at 1.3 eV that has some impact on GaAs ( $E_g = 1.4$  eV), but will significantly reduce transmittance to InGaAs ( $E_g = 1.2$  eV). The loss to GaAs is negated by ensuring electrolyte thickness of 1 cm or less, while the same for InGaAs ( $E_g = 1.2$  eV) requires ~1 mm or less of electrolyte path length. The small loss to GaAs is a concern for GaInP<sub>2</sub>/GaAs tandems because GaAs is current limiting. The larger loss to InGaAs is not an immediate concern for GaInP<sub>2</sub>/InGaAs because GaInP<sub>2</sub> is current limiting. Ultimately, Döscher et al. [2] showed that a cell design reducing typical electrolyte thickness (~2 cm) to ~1 mm allows a global maximum STH of 28% instead of 25%. Still, it remains in present work that the greatest efficiency return comes from reducing the bottom band gap.

Some PEC configurations exist for which the RLPC model could be modified. For example, an antireflective coating (MgF<sub>2</sub> or polymer) may be applied to the glass window to reduce the reflection, which could recover up to 0.9 mA/cm<sup>2</sup> for GaInP<sub>2</sub>. For production scale design, it may be cost-effective to use a different window material such as polycarbonate instead of glass. Some laboratory PEC setups do without a glass window by placing the photoelectrode facing up in an open container (beaker, tub), illuminating it from above [7]. This removes the air|glass reflection, but is likely outweighed by two issues: 1) evolving hydrogen bubbles float

toward the light source, remaining between it and the photoelectrode and increasing scattering losses while 2) requiring an additional component to collect/contain the hydrogen.

Finally, we present equations for transforming reflectance measured in air (configuration Figure 3.2.1b) to that for the same semiconductor in a PEC configuration (Figure 3.2.1a). The purpose is two-fold: 1) determine the RLPC of any photoelectrode and 2) calculate APCE from IPCE. A reflectance measurement in air gives  $R_{AS}(\lambda)$ , from which we use Eq. 3.2.1 to calculate  $n_2 = n_S(\lambda)$ , given  $n_1 = n_A = 1.00$  for air:

$$R_{AS}(\lambda) = \left( \frac{1.00 - n_S(\lambda)}{1.00 + n_S(\lambda)} \right)^2 \quad \text{Eq. 3.2.3}$$

In Figure 3.2.1a,  $I_{S,PEC}$  is the flux making it to the semiconductor in a PEC configuration. We let  $R_{PEC}(\lambda)$  be the reflectance of the set of interfaces in a PEC cell such that:

$$I_{S,PEC} = I_0 T_{AG} T_{GE} T_{ES} = I_0 T_{PEC} = I_0 (1 - R_{PEC}(\lambda)). \quad \text{Eq. 3.2.4}$$

Then, we calculate  $R_{PEC}(\lambda)$  according to

$$R_{PEC}(\lambda) = 1 - T_{AG} T_{GE} T_{ES} = 1 - T_{AG} T_{GE} \left[ 1 - \left( \frac{n_E(\lambda) - n_S(\lambda)}{n_E(\lambda) + n_S(\lambda)} \right)^2 \right] \quad \text{Eq. 3.2.5}$$

where  $n_S(\lambda)$  is given by the measured  $R_{AS}(\lambda)$  using Eq. 3.2.3 rearranged as:

$$n_S(\lambda) = \frac{1 - \sqrt{R_{AS}(\lambda)}}{\sqrt{R_{AS}(\lambda)} + 1} \quad \text{Eq. 3.2.6}$$

We note that  $n_S(\lambda)$  represents an *effective* index of refraction when calculated from  $R_{AS}(\lambda)$  of a composite absorber; e.g. an IMM with back reflector and/or ARC, where thin-film interference modulates  $R_{AS}(\lambda)$ . Regardless, we combine Eq. 3.2.4-3.2.6 to finish with a direct relationship between  $R_{AS}(\lambda)$  measured in air, and  $I_{S,PEC}$  (letting  $n_E=1.33$ , being wavelength-independent):

$$I_{S,PEC} = I_0(\lambda) T_{AG} T_{GE} \left[ 1 - \left( \frac{2.33\sqrt{R_{AS}(\lambda)} + 0.33}{0.33\sqrt{R_{AS}(\lambda)} + 2.33} \right)^2 \right] \quad \text{Eq. 3.2.6}$$

$I_{S,PEC}$  is integrated to give the RLPC (using the AM 1.5G spectrum for  $I_0(\lambda)$ ) of any photoelectrode:

$$RLPC = \int_0^{\lambda_{BG}} I_{S,PEC} d\lambda \quad \text{Eq. 3.2.7}$$

where  $\lambda_{BG}$  is the wavelength corresponding to  $E_g$  (i.e.  $E_g \lambda_{BG} = hc \approx 1240 \text{ eV} \cdot \text{nm}$  where  $h$  is Planck's constant and  $c$  is the speed of light in vacuum).

Next, we use  $R_{PEC}(\lambda)$  obtained from Eq. 3.2.5 to convert IPCE into APCE. From Figure 3.2.2, we notice that the declining IPCE toward shorter wavelengths between 400 nm and 550 nm, tracks with increasing reflectance. Thus, when reflectance is deconvoluted, we see that

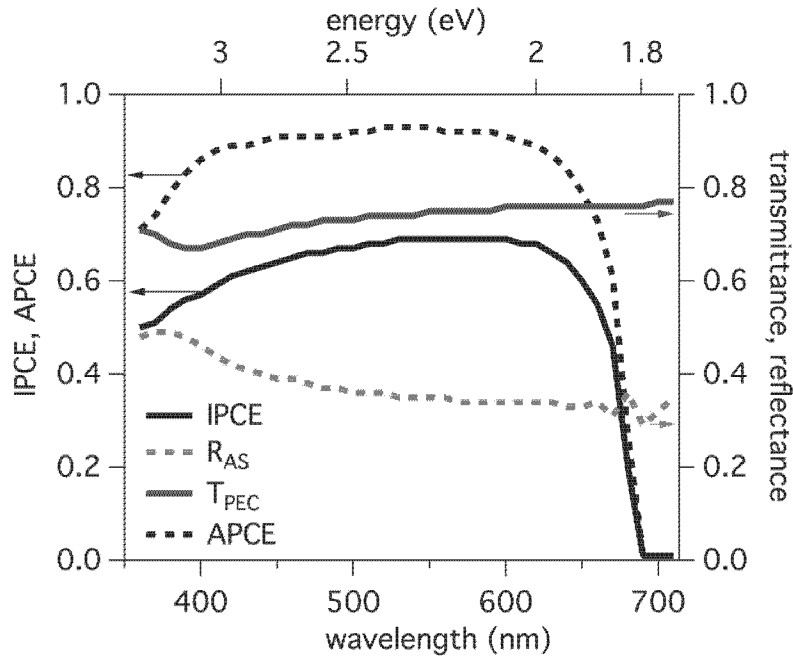


Figure 3.2.2: Example where top p-GaInP<sub>2</sub> sub-cell IPCE is converted to APCE by dividing by  $T_{PEC}$ , which is calculated from measured  $R_{AS}$  using Eq. 3.2.3-3.2.6.

APCE is flatter over this range. At wavelengths below 400 nm, APCE does drop, most likely due to surface recombination.

### 3.3 Photocurrent onset potential: Improving with doping profiles

In this Chapter, we present the development and analysis of alternative PEC junction doping profiles that improve photocurrent onset potential ( $V_{os}$ ). First, we consider performance expectations by considering the voltage load of water splitting and the open-circuit voltage ( $V_{oc}$ ) performance of solid-state PV analogues. In PEC current-voltage (IV) measurements, the photocurrent onset potential ( $V_{os}$ ) is a photovoltage metric defined as the point where cathodic and anodic currents are equal. All samples had PtRu catalyst deposited on their surfaces by sputtering (Ch. 4.3). All characterizations are performed in 3M sulfuric acid electrolyte with 1mM Triton X-100 surfactant added and under illumination by the two-source solar simulator described in Ch. 2.2.

#### Expected photovoltage vs. water splitting load line

A tradeoff of voltage performance for photocurrent is inherent to the lower bandgaps required for reaching higher STH efficiency. However, sufficient photovoltage for unassisted water splitting must be maintained. The thermodynamic constraint is having bandgap energy ( $E_g$ ) greater than 1.23 eV ( $\Delta G$  for water splitting at 25 °C), which should be expanded to account for both electrochemical overpotential and solid-state overvoltage. Seeking efficiencies associated with photocurrent densities near 20 mA/cm<sup>2</sup>, we add kinetic overpotentials of 80 mV and 220 mV for the HER (on Pt) and OER (on RuO<sub>2</sub>), respectively, as well as 100 mV solution resistance loss [2]. Thus, a total load line for water splitting of 1.63 V is expected.

For a wide range of single-junction III-V solar cell bandgaps, King et al. [9] observed a constant offset between  $E_g$  and  $V_{oc}$ . They defined the bandgap-voltage offset ( $W_{oc}$ ) as

$$W_{oc} \equiv E_g/q - V_{oc} \quad \text{Eq. 3.3.1}$$

and derived its theoretical basis from the Shockley-Queisser detailed balance model. This reinforced that  $W_{oc}$  is practically constant, varying by only 70 mV across a bandgap range of 2.0 eV to 0.7 eV. Relevant to water splitting is the range  $E_g = 1-1.8$  eV, having  $W_{oc} = 0.4 \pm 0.05$  V. Thus, we set photovoltage performance expectations for high-quality III-V tandems [9][10] having top ( $E_g^{top}$ ) and bottom ( $E_g^{bottom}$ ) bandgaps as:

$$E_g^{top} + E_g^{bottom} \geq q(1.63 V + 2 * 0.4 V) = 2.43 eV \quad \text{Eq. 3.3.2}$$

The Eq. 3.3.2 limit is manifest as the region of zero STH for low  $E_g^{top}$  and  $E_g^{bottom}$  (Figure 3.1.1) due to insufficient photovoltage.

Per Eq. 3.3.1, a GaInP<sub>2</sub>/InGaAs tandem with 1.8/1.2 eV bandgap combination exceeds the Eq. 3.3.2 limit by 0.57 V. When characterizing the photocathode, we could expect  $V_{os} = 0.57$  V. However, the initial measurements (Figure 3.3.1) fell short of unbiased water splitting, having a negative  $V_{os}$ . In Figure 3.3.1, a GaInP<sub>2</sub>/GaAs photocathode has  $V_{os} = 0.2$  V and generates -9 mA/cm<sup>2</sup> photocurrent at short circuit (0 V vs. IrO<sub>x</sub>) having 11% STH efficiency. The GaInP<sub>2</sub>/InGaAs photocathode produces higher current, but its  $V_{os}$  is slightly less than zero, having by definition, zero STH efficiency.

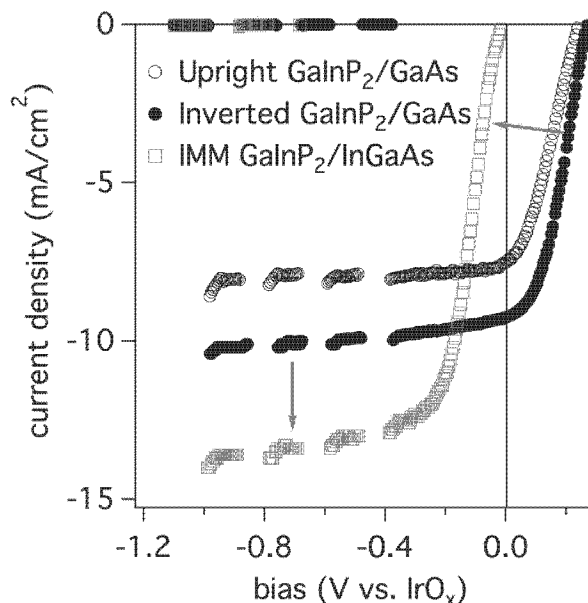


Figure 3.3.1: Preliminary characterization showing current-for-voltage tradeoff between  $\text{GaInP}_2/\text{GaAs}$  (black) and  $\text{GaInP}_2/\text{InGaAs}$  (green) having 1.8/1.4 eV and 1.8/1.2 eV bandgap combinations, respectively. Inverted architecture (solid black circles) provides some photocurrent increase for the  $\text{GaInP}_2/\text{GaAs}$  tandem, without a photovoltage tradeoff of decreasing bandgaps.

However, improving  $V_{\text{os}}$  by only  $\sim 0.3$  V would result in short-circuit photocurrent densities near  $-13 \text{ mA/cm}^2$  and 16% STH efficiency. This motivates the following sections where we investigate doping profiles that improve photovoltage toward the  $V_{\text{os}}$  expectations. We established a RLPC of  $14.8 \text{ mA/cm}^2$  for  $\text{GaInP}_2$  (Ch. 3.2.), which is the current-limiting junction of this device. Therefore, efforts to improve photocurrent, outside of addressing reflection losses (Ch. 3.4), could only result in marginal STH gains. Since the bottom solid-state PV junction is relatively well developed and fully optimized, efforts to improve photovoltage focus on the top PEC junction.

### Doping profiles investigated

We start by presenting reference band bending calculations for traditional p- $\text{GaInP}_2$  photocathodes that have uniform p-type (Zn) doping density ( $p$ ) throughout. This structure

named "p" is illustrated in Fig. 3.3.2. We vary the doping level from a baseline of  $p = 10^{17} \text{ cm}^{-3}$  as targeted during epitaxial growth. These results are discussed in consideration of absorption length data for  $\text{GaInP}_2$ . Next, we investigate the finding that a nominally undoped interlayer between p- $\text{GaInP}_2$  and the electrolyte (Fig. 3.3.2, "p-i") improves  $V_{\text{os}}$ . Due to background carbon incorporation, this layer (i- $\text{GaInP}_2$ ) has intrinsic doping that is moderately p-type at  $p \sim 10^{15} \text{ cm}^{-3}$ . We reveal a trend between the intrinsic layer thickness ( $t_i$ ), depletion width, and  $V_{\text{os}}$ . We also compare one p-i profile a p-n profile (Fig. 3.3.2, "p-n") that showed considerably better  $V_{\text{os}}$  beyond the improvement of the best p-i structure tested. We then investigate the influence of n-type (Se) doping density, comparing the  $n = 10^{18} \text{ cm}^{-3}$  baseline level to samples having 2n and 5n. Finally, we apply the best doping profile to an IMM to demonstrate overall progress.

<u>Name</u>	<u>Description</u>	<u>PEC junction structure</u>	<u>Study</u>
<b>"p"</b>	uniform p-type doping	<p>p-type <math>\text{GaInP}_2</math> (<math>t_p = 2 \mu\text{m}</math>)</p>	baseline case, uniformly p-type
<b>"p-i"</b>	p-type/intrinsic bilayer	<p>p-type <math>t_p = 1 \mu\text{m}</math></p> <p>intrinsic; <math>t_i = 25, 80, 200 \text{ nm}</math></p>	vary thickness of intrinsic layer
<b>"p-n"</b>	p-type/n-type bilayer	<p>p-type <math>t_p = 1 \mu\text{m}</math></p> <p>n-type (25 nm) <math>n, 2n, 5n</math></p>	vary doping of n-type layer

Figure 3.3.2: Name, description, and structure of the doping profiles investigated.

\*Note: "p-i" structures were studied as part of tandem devices (having integrated GaAs PV junction) while "p-n" structures were epilayers grown on degenerate, inactive GaAs substrate.

### Band bending calculations

Band bending diagrams represent the built-in fields that separate charges in a semiconductor. The band edge energetics at a semiconductor/electrolyte interface can be

measured relative the hydrogen reduction potential ( $V_{\text{HER}}$  or  $E_{\text{HER}}$ ) using one or more PEC methods (Chapter 1). Typical measurements place the conduction band edge ( $E_{\text{CB}}$ ) of p-GaInP<sub>2</sub> 0.6 V above (more negative than)  $V_{\text{HER}}$  [11][12], which serves as the p-GaInP<sub>2</sub>/electrolyte boundary condition for band bending calculations.

Band bending in photoelectrochemical junctions follows a Schottky junction model [13]. When a semiconductor Fermi level ( $E_f$ ) equilibrates with electrolyte redox potential, an amount of mobile charge  $Q_E$  in the electrolyte moves to the semiconductor|electrolyte interface, balancing the fixed charge of ionized dopant atoms  $Q_d$  in the semiconductor depletion region [13]. At equilibrium, we have  $E_f = V_{\text{HER}}$  for a photocathode which we set to zero ( $E_f = V_{\text{HER}} = 0$ ). The depletion width approximation assumes full ionization within the depletion region that extends a distance  $x_p$  into the semiconductor and no ionization beyond  $x_p$ . Thus,  $Q_d$  is given by

$$Q_E = Q_d = qN_p x_p$$

where  $N_p$  is the doping density and  $q$  is the elementary charge constant. Beyond the depletion region, the electric field ( $\mathcal{E}$ ) is zero. At a location  $x$  within the depletion region ( $0 < x < x_p$ ),  $\mathcal{E}$  is given by:

$$\mathcal{E}(x) = \frac{qN_p}{\epsilon_s}(x_p - x)$$

where  $\epsilon_s$  is the semiconductor dielectric constant. The negative integral of the electric field over  $x$  gives the potential ( $\phi(x)$ ):

$$\phi(x) = -\frac{qN_p}{2\epsilon_s}[x_p^2 - (x_p - x)^2]$$

Band bending calculations (diagrams) are thus a plot of  $\phi(x)$  whose slope (derivative) is proportional to  $\mathcal{E}(x)$ . Electrons move in 1D space toward lower  $\phi$  and holes toward higher  $\phi$ .

Where  $\phi(x)$  is constant (i.e. beyond depletion region), electrons/holes move by diffusion only. Note that we set  $E_f = E_{\text{HER}} = 0$  to define zero for the energy/voltage axis.

In the following sections, we evaluate photovoltage performance against band-bending calculations representing the electrostatic forces driving charge separation, noting that: 1) under illumination, bands are expected to flatten due to mobile charges negating built-in fields [14] and 2) under bias, the Fermi-level in the bulk semiconductor is controlled, leading to increased band bending and deeper depletion for photocathodes under cathodic bias and decreased band bending and shallower depletion when approaching the photocurrent onset potential [7]. Modeling under illumination and applied bias is beyond the scope of current work. Yet, the following sections reveal trends between photovoltage performance and the reference models provided by equilibrium band bending calculations.

### **Band bending in p-GaInP<sub>2</sub> photocathodes**

We first present reference band bending calculations for traditional, p-GaInP<sub>2</sub> photocathodes that have uniform p-type doping. Within the depletion region at the electrolyte interface, charge separation and collection is field-driven. Beyond the depletion width, the bands are flat and transport occurs by diffusion. The band bending of Figure 3.3.3a shows the doping densities of  $p = 10^{18}$ ,  $10^{17}$ , and  $10^{16} \text{ cm}^{-3}$ , resulting in  $x_p \approx 50, 100, 400 \text{ nm}$ . We include  $p = 10^{15} \text{ cm}^{-3}$  and note that its near-linear band bending extends  $x_p$  to nearly  $1 \mu\text{m}$ . Figure 3.3.3b shows photon absorption length data for GaInP<sub>2</sub> overlaid on AM 1.5G photon flux distribution. This illustrates the depth at which light is absorbed for relevant wavelengths. For  $p = 10^{18} \text{ cm}^{-3}$ , photons having  $\lambda < 420 \text{ nm}$ , only a small portion of the incident flux, are absorbed within the depletion region. For  $p = 10^{17} \text{ cm}^{-3}$ , the same is true for  $\lambda < 480 \text{ nm}$ , a slightly larger portion of the solar flux.

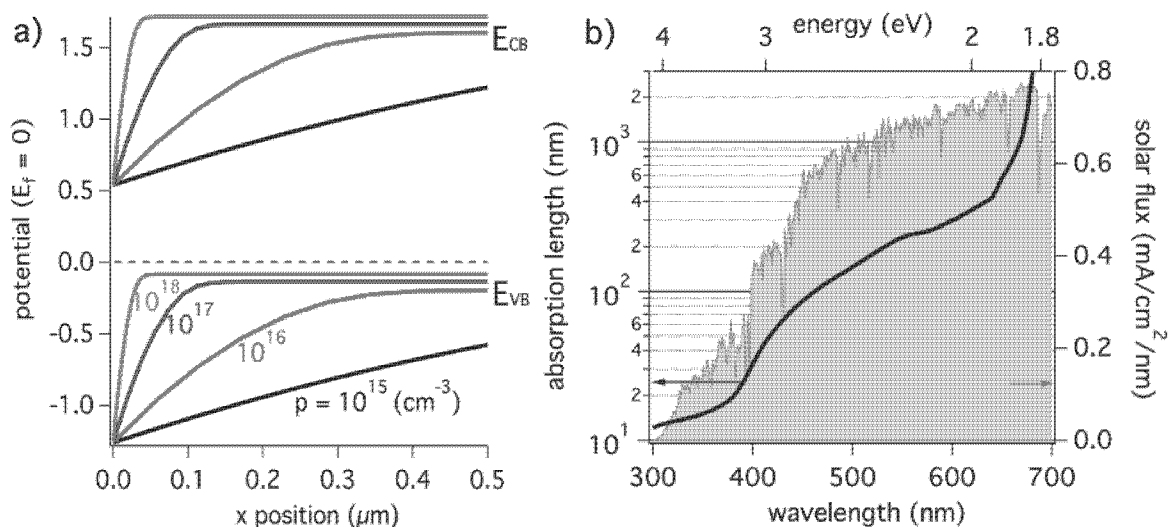


Figure 3.3.3: (a) Calculated band bending diagram vs. position within a GaInP<sub>2</sub> photocathode (electrolyte interface at  $x = 0$ ) for p-type (Zn) doping densities of  $10^{15}$  (black),  $10^{16}$  (red),  $10^{17}$  (blue), and  $10^{18}$  (green)  $\text{cm}^{-3}$ . Both the valence band ( $E_{VB}$ ) and conduction band ( $E_{CB}$ ) are shown. (b) Photon absorption length for GaInP<sub>2</sub> (black line) is plotted with solar flux.

However, the depletion widths for  $p = 10^{16} \text{ cm}^{-3}$  and  $10^{15} \text{ cm}^{-3}$  are larger than the absorption length of most photons. Here, nearly all are absorbed in the wider depletion region, being separated and collected more efficiently by drift (field-driven) than diffusion. This shows how doping tunes band bending and the relative contribution of drift vs. diffusion in charge separation. The calculations are for traditional, uniformly doped p-GaInP<sub>2</sub> photocathodes; the reference case for "p-i" and "p-n" doping profiles.

### "p-i" doping profile

We investigate an observation that a residual, undoped layer (i-GaInP<sub>2</sub>) on top of p-GaInP<sub>2</sub> (Figure 3.3.2, "p-i" structure) improves  $V_{os}$ . Originally, the 500 nm i-GaInP<sub>2</sub> layer was a sacrificial etch-stop layer used in device processing that was inadvertently left on. Despite improved  $V_{os}$ , the photocurrent was low, which we hypothesized could be improved by reducing the i-layer thickness. We fabricated "p-i" doping profiles in the top GaInP<sub>2</sub> PEC junction as part

of IMM GaInP<sub>2</sub>/GaAs tandems, having i-layer thickness ( $t_i$ ) of  $t_i = 200, 80,$  and  $25$  nm. We also compare one "p-n" device with n-layer thickness ( $t_n$ ) of  $25$  nm. Since GaAs is current limiting in GaInP<sub>2</sub>/GaAs tandems, only differences in photovoltage are meaningful. Therefore, we have normalized the photocurrent. The chopped light current-voltage (CLIV) measurements are performed in a three-electrode configuration with voltage relative to mercury sulfate reference electrode (MSE).

The "p-i" band bending calculations (Figure 3.3.4a) show that  $x_p$  increases with  $t_i$ , being approximately equal to  $t_i$  except for the case of  $t_i = 25$  nm (red). Here,  $x_p$  is limited to that of the uniformly p-type band bending (black).

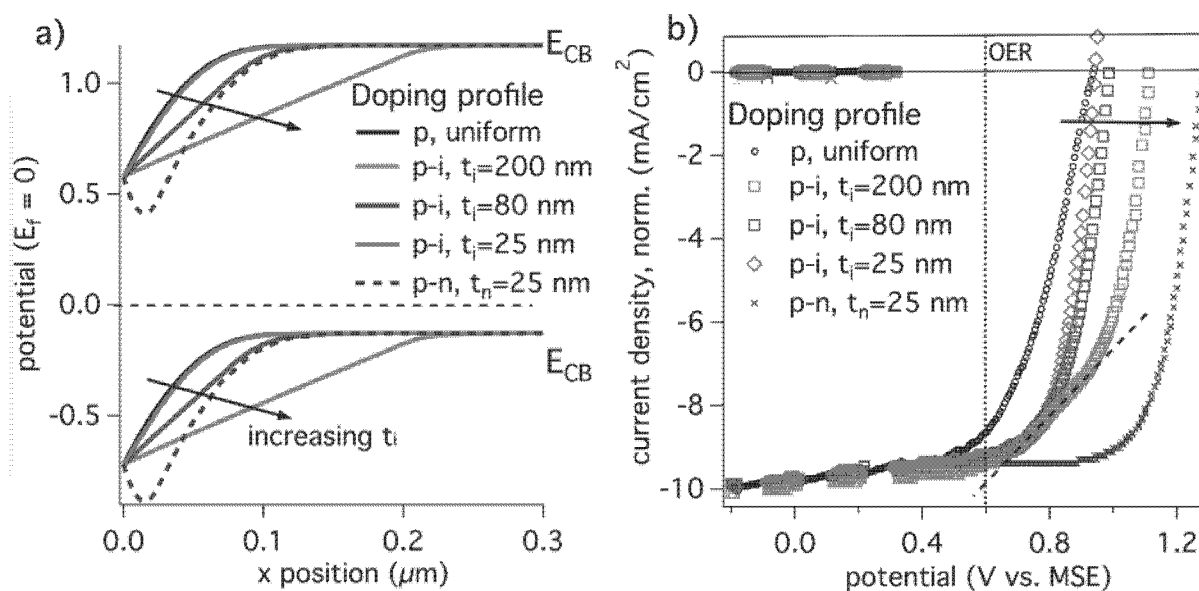


Figure 3.3.4: (a) Band bending calculations and (b) CLIV characterization of tandems with top GaInP<sub>2</sub> junction having "p-i" doping profiles of varying i-layer thickness.

The CLIV characterization of Figure 3.3.4b shows that  $V_{os}$  increases with  $t_i$ , with the thinnest ( $t_i = 25$  nm, red) having the same  $V_{os}$  as the uniformly p-type sample (black). The thickest ( $t_i = 200$  nm, green) shows  $V_{os}$  that is improved by  $0.2$  V. The "p-n" sample is better yet, which motivated further investigation in the next section. An additional feature is distinguishable for  $t_i = 200$  nm, manifest as a linear region (dashed black line) on the "knee" of its CLIV.

The matching  $V_{os}$  of the uniformly p-type and  $t_i = 25$  nm samples is consistent with their band bending being identical. The increase in  $V_{os}$  with  $t_i$  corresponds with the increase in  $x_p$  revealed by the band bending calculations. Having a lower doping density ( $\sim 10^{15}$  cm<sup>-3</sup> p-type), the i-GaInP<sub>2</sub> layer extends the depletion width, as also occurring for the reference band bending calculations of Figure 3.3.3a. Thus, we expect  $V_{os}$  could also be improved by lowering the doping density of the uniformly p-type photocathodes. A consequence of the thickest i-layer ( $t_i = 25$  nm) is the linear "knee" on its CLIV. We attribute this Ohmic behavior to its lower conductivity, becoming significant for thicker  $t_i$ . Although  $V_{os}$  may be improved by further increasing  $t_i$ , the Ohmic knee suggests a limit to the approach of "p-i" doping profiles. Future optimization work could be pursued, but outperformance by the initial "p-n" result precluded further investigation of "p-i" samples.

### **"p-n" doping profile**

Here we analyze photovoltage performance of a "p-n" doping profile (Figure 3.3.2) where the n-layer doping density is varied. Instead of a full tandem, we use GaInP<sub>2</sub> photocathodes without the GaAs bottom junction, being simpler to fabricate. The n-layer thickness is constant at  $t_n = 25$  nm, while its doping is increased from the baseline level of  $n = 10^{18}$  cm<sup>-3</sup> to  $2n$  and  $5n$ . The  $t_n = 25$  nm sample in Figure 3.3.4b of the previous section has the same n-layer doping density, but is part of a tandem and not directly comparable to the "p-n" photocathodes here. Instead, we use a uniformly doped p-GaInP<sub>2</sub> photocathode as the control sample.

The band bending calculations of Figure 3.3.5 show downward band bending toward the surface and depletion widths that increase with n-layer doping density. However, large upward band bending also occurs in a narrow,  $\sim 25$  nm wide region immediately beneath the surface.

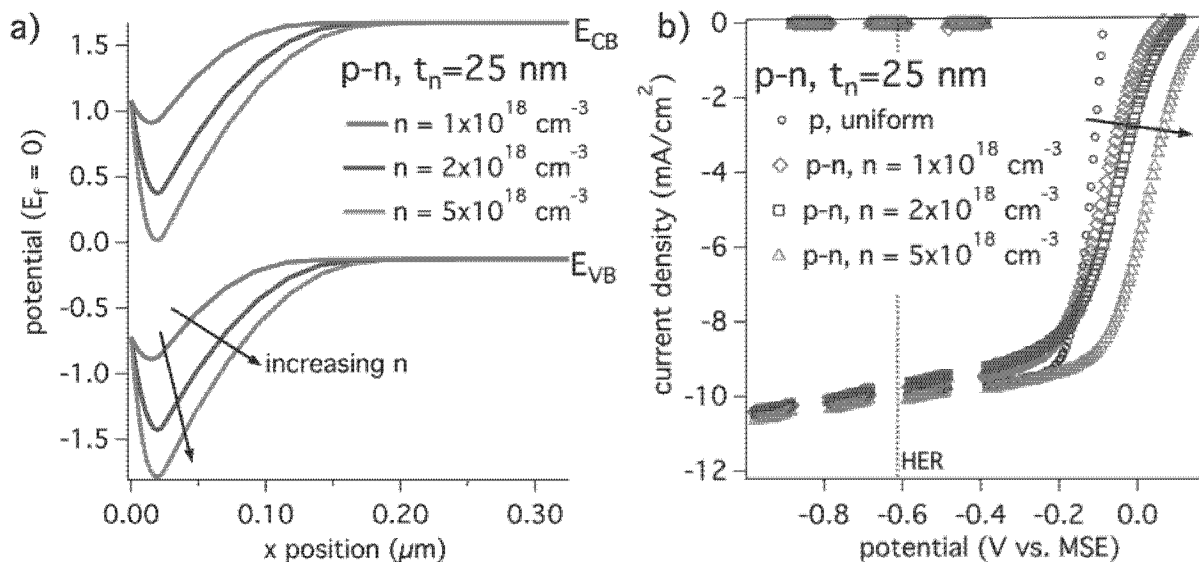


Figure 3.3.5: (a) Band bending calculations and (b) CLIV characterization of GaInP<sub>2</sub> photocathodes having "p-n" doping profiles of varying n-type doping density.

The CLIVs (Figure 3.3.5b) show that the uniformly p-type control photoelectrode (black) has  $V_{os} = -0.1$  V vs. MSE. The "p-n" samples have  $V_{os}$  0.1–0.3 V more positive, increasing with n-layer doping density.

The n-layer clearly improves  $V_{os}$  and is better for higher n. The increased  $V_{os}$  with increasing depletion width matches the trend observed for "p-i" (Fig. 3.3.4). However, this may be unexpected given the large upward band bending at the surface, representing a barrier to electrons. Observations during IPCE measurements are consistent with its presence: IPCE at short wavelengths being absorbed near the surface is either drastically reduced or even negative (anodic current) in "p-n" structures. Thus, upward band bending at the surface drives holes toward the electrolyte, resulting in anodic instead of cathodic current. However, IPCE is measured under monochromatic illumination at much lower intensity than white light. The

upward band bending should flatten under higher flux white light illumination [14], diminishing the barrier. An alternative mechanism is tunneling, occurring for a sufficiently thin barrier, that allows facile electron transport through the barrier. This has been used to achieve high photovoltage demonstrated on  $n^+p$ -Si photoelectrodes [15]. However, the barrier in Figure 3.3.5a is  $\sim 20$  nm and too wide to expect tunneling. Future work includes further increasing doping density to validate this mechanism.

We apply an improved "p-n" structure to an IMM, demonstrating  $V_{os}$  improvement of 0.2 V (Figure 3.3.6, green arrow) over first results (Figure 3.3.1) that used uniform "p" doping. At the time, only the baseline  $n = 10^{18} \text{ cm}^{-3}$  was used, which is expected to improve for 2n, 5n, and may further yet if the  $V_{os}$  trend of Figure 3.3.5b continues.

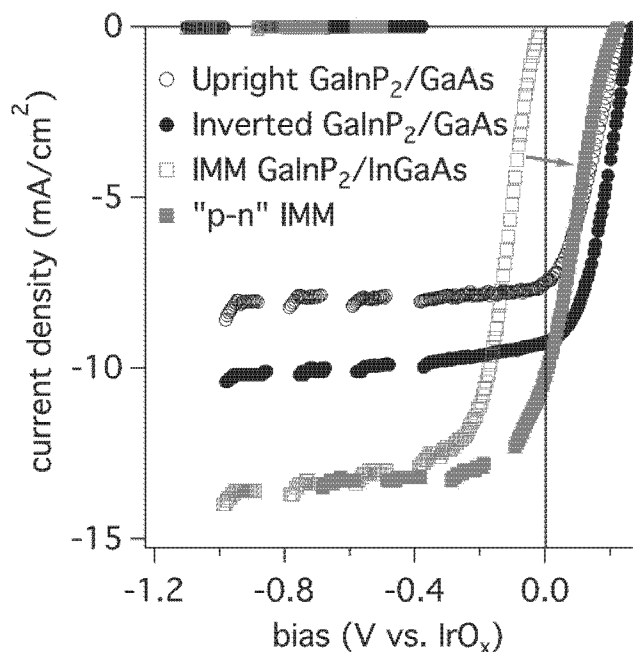


Figure 3.3.6: The progress (green arrow) afforded by a "p-n" doping profile when applied to an IMM GaInP<sub>2</sub>/InGaAs tandem (solid green squares) is as combined with the preliminary data from Figure 3.3.1.

We have demonstrated photovoltage improvements through doping profiles new to GaInP<sub>2</sub> photocathodes. However, the photovoltage expectation given by Eq. 3.3.1 for GaInP<sub>2</sub> ( $E_g$

= 1.8 eV) is  $\sim 1.4$  V. Relative the HER potential indicated in Figure 3.3.5b, we achieve a photovoltage of 0.8 V while facile HER kinetics account for only 50-100 mV overpotential on the PtRu-treated GaInP<sub>2</sub> surface. Thus, considerable opportunity for improvement of another  $\sim 0.5$  V remains.

### 3.4 Design and demonstration of anti-reflective TiO<sub>2</sub> coating

In section 3.2, we calculated reflection losses associated with the interfaces of a PEC cell. Overall reflection is lower in a PEC configuration than for the same semiconductor in air. However, reflection of 20-25% at the semiconductor/electrolyte interface is the largest source photocurrent loss. Here, we use TiO<sub>2</sub> as an anti-reflective coating, with thickness optimized for the spectral response of tandem devices, and demonstrate improved photocurrent on p-GaInP<sub>2</sub> photocathodes.

A photocathode coating material must meet several requirements. It must be 1) transparent to solar spectrum, 2) conductive to electrons with minimal current or voltage loss, and 3) resistant to corrosion or amenable to stabilization. Furthermore, a single-layer anti-reflective coating material should have an index of refraction that is intermediate to GaInP<sub>2</sub> and water (electrolyte). The ideal index of such an index-matched ARC is given by the geometric mean [18] of the two media, in this case GaInP<sub>2</sub> ( $n_3 \approx 3.6$ ) and water ( $n_1 \approx 1.3$ ), which is  $n_2 \approx 2.2$ .

TiO<sub>2</sub> meets the above requirements and its deposition by ALD has the added advantages of providing uniform, pin-hole free films at relatively low temperatures [19]. XRD measurements indicate ALD TiO<sub>2</sub> is amorphous. Electron conductivity through TiO<sub>2</sub> is supported by its intrinsic n-type doping (oxygen vacancies), and its conduction band being just

above the hydrogen redox potential provides a favorable alignment for photocathodes [20][21]. Furthermore, ALD  $\text{TiO}_2$  has been used to successfully stabilize photocathodes [13][15].

To generate optical constants ( $n$ ,  $k$ ) necessary for ARC modeling, we deposit films on Si substrate and characterize with spectroscopic ellipsometry. Modeling was performed by letting the spectral reflectance associated with the ARC modulate spectral response data (EQE) measured for a  $\text{GaInP}_2/\text{InGaAs}$  (1.8/1.2 eV) tandem. Sample calculations<sup>1</sup> showing how reflectance and thus EQE change with the ARC coating thickness are shown in Figure 3.4.1a. Since the top  $\text{GaInP}_2$  junction is current limiting, we are primarily concerned with increasing its response (for  $\lambda < 685$  nm). Without any coating (0 nm thickness, black line), the top junction EQE is limited to a maximum of  $\sim 0.6$  due to significant reflectance (35–40%). For 30 nm  $\text{TiO}_2$ , a considerable decrease in reflectance and associated increase in EQE to  $\sim 0.7$  is realized. For increasing thickness, the reflectance minimum broadens and shifts to higher wavelengths. Thus, reflectance is tuned to increase EQE over the wavelengths relevant to  $\text{GaInP}_2$ .

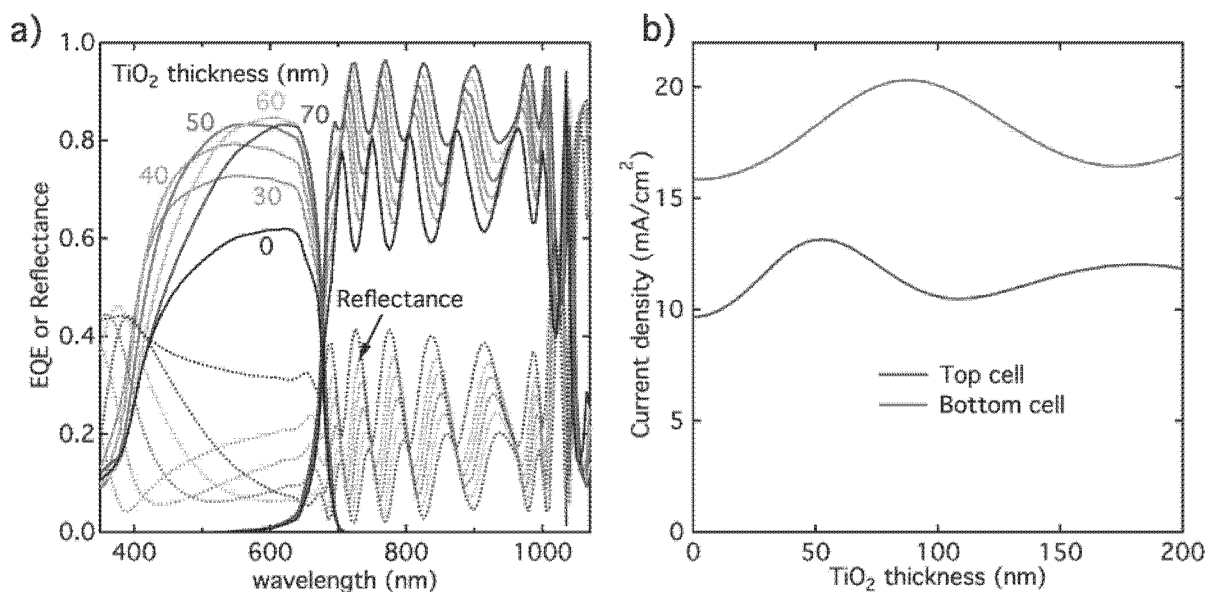


Figure 3.4.1: (a) Spectral response of  $\text{GaInP}_2/\text{InGaAs}$  tandem showing decreased reflectance for a range  $\text{TiO}_2$  ARC thicknesses. (b) Sub-cell current densities plotted vs.  $\text{TiO}_2$  thickness.

<sup>1</sup> Modeling performed by Myles Steiner at the National Renewable Energy Laboratory.

Integrating the EQE over the solar spectrum, we obtain a plot of  $\text{TiO}_2$  thickness vs. current density for each sub-cell (Figure 3.4.1b). The current-limiting top cell has a maximum of  $13 \text{ mA/cm}^2$  for  $50 \text{ nm}$ , an increase of  $30\%$  over the  $10 \text{ mA/cm}^2$  without ARC. We note this modeling assumes that the device is in air instead of electrolyte. As shown in Ch. 3.2, a further increase of  $\sim 11\%$  is expected when accounting for the reduced reflectance of a PEC configuration.

We deposit  $50 \text{ nm}$  ALD  $\text{TiO}_2$  on  $\text{p-GaInP}_2$  photocathodes and then sputter PtRu nanoparticle catalyst on the surface. We compare CLIV performance of this sample in Figure 3.4.2a to bare  $\text{p-GaInP}_2$  (black),  $\text{p-GaInP}_2$  with PtRu (red), and  $\text{p-GaInP}_2$  with  $\text{TiO}_2$  (blue). Conductive fluorine-doping tin oxide (FTO) substrates modified in the same ways are shown in Figure 3.4.2b. Since FTO is not photoactive, its characterization is performed in the dark. The FTO samples provide a measure of the baseline HER onset potential for each modification.

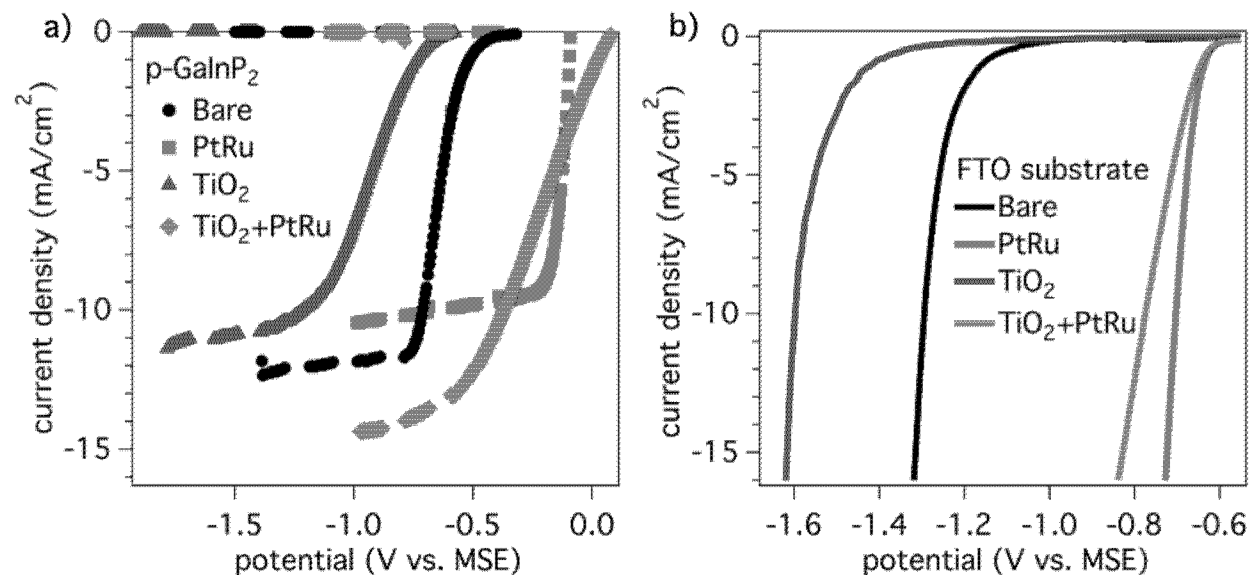


Figure 3.4.2: (a) CLIV characterization of  $\text{p-GaInP}_2$  photocathodes that have no/bare (black), PtRu (red),  $\text{TiO}_2$  (blue), or  $\text{TiO}_2$ |PtRu (green) modification. (b) Equivalently modified set of conductive FTO substrates for baseline HER characterization of each surface.

The PtRu improves  $V_{os}$  over bare p-GaInP<sub>2</sub> by 0.5 V, while the TiO<sub>2</sub> decreases  $V_{os}$  by 0.2 V. Considerable  $V_{os}$  improvement is provided when PtRu is applied on top of the TiO<sub>2</sub> (TiO<sub>2</sub>+PtRu). The measurements on FTO support that TiO<sub>2</sub> has considerably worse activity than PtRu. When applied on top of TiO<sub>2</sub>, PtRu recovers the lost activity, but a residual Ohmic component associated with the TiO<sub>2</sub> is observed. On FTO, the TiO<sub>2</sub>/PtRu requires more negative potentials to obtain the same current densities as PtRu. On p-GaInP<sub>2</sub>, the same effect occurs. Although its  $V_{os}$  is the best, a sluggish onset requires more applied bias to reach its light-limited photocurrent, the ideal photocathode operating point. Still, the TiO<sub>2</sub> + PtRu coating does provide higher photocurrents, demonstrating anti-reflective properties.

First attempts applying the TiO<sub>2</sub> ARC to an IMM tandem device were unsuccessful, likely due to the thermal limit of the mounting epoxy used in processing, evidenced by the device peeling from its Si handle substrate. Future work should include lower temperature ALD or other low-temperature TiO<sub>2</sub> deposition methods.

## References

- [1] B. D. James, G. N. Baum, J. Perez, and K. N. Baum, "Technoeconomic analysis of photoelectrochemical (PEC) hydrogen production," *DOE Contract Number GS-10F-009J*, vol. 22201, no. December, pp. 1–128, 2009.
- [2] H. Döscher, J. F. Geisz, T. G. Deutsch, and J. A. Turner, "Sunlight absorption in water – efficiency and design implications for photoelectrochemical devices," *Energy Environ. Sci.*, vol. 7, no. 9, pp. 2951–2956, 2014.
- [3] O. Khaselev and J. A. Turner, "A Monolithic Photovoltaic-Photoelectrochemical Device for Hydrogen Production via Water Splitting," *Science (80-. )*, vol. 280, no. 5362, pp. 425–427, 1998.
- [4] J. F. Geisz, S. Kurtz, M. W. Wanlass, J. S. Ward, a. Duda, D. J. Friedman, J. M. Olson,

- W. E. McMahon, T. E. Moriarty, and J. T. Kiehl, "High-efficiency GaInP/GaAs/InGaAs triple-junction solar cells grown inverted with a metamorphic bottom junction," *Appl. Phys. Lett.*, vol. 91, no. 2, pp. 1–4, 2007.
- [5] D. Shahrjerdi, S. W. Bedell, C. Bayram, and D. Sadana, "Flexible InGaP/(In)GaAs tandem solar cells with very high specific power," *Photovolt. Spec. Conf. (PVSC), 2013 IEEE 39th*, pp. 2805–2808, 2013.
- [6] T. G. Deutsch and J. A. Turner, "Semiconductor Materials for Photoelectrolysis: 2014 U.S. DOE Hydrogen & Fuel Cells Program Review," 2014.
- [7] Z. Chen, H. N. Dinh, and E. Miller, *Photoelectrochemical Water Splitting: Standards, Experimental Methods, and Protocols*. 2013.
- [8] Z. Chen, T. F. Jaramillo, T. G. Deutsch, A. Kleiman-Shwarsctein, A. J. Forman, N. Gaillard, R. Garland, K. Takanabe, C. Heske, M. Sunkara, E. W. McFarland, K. Domen, E. L. Miller, J. a. Turner, and H. N. Dinh, "Accelerating materials development for photoelectrochemical hydrogen production: Standards for methods, definitions, and reporting protocols," *J. Mater. Res.*, vol. 25, no. 01, pp. 3–16, 2010.
- [9] R. R. King, D. Bhusari, A. Boca, D. Larrabee, X.-Q. Liu, W. Hong, C. M. Fetzer, D. C. Law, and N. H. Karam, "Bandgap-Voltage Offset and Energy Production in Next-Generation Multijunction Solar Cells," *5th World Conf. Photovolt. Energy Convers. 25th Eur. Photovolt. Sol. Energy Conf.*, pp. 6–10, 2010.
- [10] R. R. King, D. C. Law, K. M. Edmondson, C. M. Fetzer, G. S. Kinsey, H. Yoon, R. a. Sherif, and N. H. Karam, "40% efficient metamorphic GaInP/GaInAs/Ge multijunction solar cells," *Appl. Phys. Lett.*, vol. 90, no. 18, pp. 98–100, 2007.
- [11] B. A. MacLeod, K. X. Steirer, J. L. Young, U. Koldemir, A. Sellinger, J. A. Turner, T. G. Deutsch, and D. C. Olson, "Phosphonic Acid Modification of GaInP<sub>2</sub> Photocathodes Toward Unbiased Photoelectrochemical Water Splitting," *ACS Appl. Mater. Interfaces*, vol. 7, no. 21, pp. 11346–11350, 2015.
- [12] S. S. Kocha, J. a. Turner, and a. J. Nozik, "Study of the Schottky barrier and determination of the energetic positions of band edges at the n- and p-type gallium indium phosphide electrode | electrolyte interface," *J. Electroanal. Chem.*, vol. 367, no. 1–2, pp. 27–30, 1994.
- [13] R. S. Muller and T. I. Kamins, *Device electronics for integrated circuits*, 3rd ed. New

York: John Wiley & Sons, 2003.

- [14] J. A. Turner, "Energetics of the Semiconductor-Electrolyte Interface," *J. Chem. Educ.*, vol. 60, no. 4, pp. 327–329, 1983.
- [15] S. W. Boettcher, E. L. Warren, M. C. Putnam, E. a. Santori, D. Turner-Evans, M. D. Kelzenberg, M. G. Walter, J. R. McKone, B. S. Brunschwig, H. a. Atwater, and N. S. Lewis, "Photoelectrochemical hydrogen evolution using Si microwire arrays," *J. Am. Chem. Soc.*, vol. 133, no. 5, pp. 1216–1219, 2011.
- [16] A. Bansal and J. Turner, "Suppression of band edge migration at the p-GaInP<sub>2</sub>/H<sub>2</sub>O interface under illumination via catalysis," *J. Phys. Chem. B*, vol. 104, pp. 6591–6598, 2000.
- [17] W. A. Smith, I. D. Sharp, N. C. Strandwitz, and J. Bisquert, "Interfacial band-edge energetics for solar fuels production," *Energy Environ. Sci.*, vol. 8, no. 10, pp. 2851–2862, 2015.
- [18] J. Krepelka, "Maximally flat antireflective coatings," *Jemná Mech. A Opt.*, vol. 53, pp. 3–5, 1992.
- [19] S. M. George, "Atomic layer deposition: An overview," *Chem. Rev.*, vol. 110, no. 1, pp. 111–131, 2010.
- [20] B. Seger, T. Pedersen, A. B. Laursen, P. C. K. K. Vesborg, O. Hansen, and I. Chorkendorff, "Using TiO<sub>2</sub> as a conductive protective layer for photocathodic H<sub>2</sub> evolution," *J. Am. Chem. Soc.*, vol. 135, no. 3, pp. 1057–1064, 2013.
- [21] M. Malizia, B. Seger, I. Chorkendorff, and P. C. K. Vesborg, "Formation of a p–n heterojunction on GaP photocathodes for H<sub>2</sub> production providing an open-circuit voltage of 710 mV," *J. Mater. Chem. A*, vol. 2, no. 19, p. 6847, 2014.
- [22] A. Paracchino, N. Mathews, T. Hisatomi, M. Stefiik, S. D. Tilley, and M. Grätzel, "Ultrathin films on copper(i) oxide water splitting photocathodes: a study on performance and stability," *Energy Environ. Sci.*, vol. 5, no. 9, p. 8673, 2012.

## 4. Stability and stabilization of III-Vs

### 4.1 Surface passivation of GaInP<sub>2</sub> by water vapor<sup>1</sup>

#### Abstract

The photoluminescence (PL) intensity of semiconductors can be modulated by their ambient. GaInP<sub>2</sub> responds reversibly to water vapor, irreversibly to oxygen, and with a time dependence to air. We characterize the reversible PL response to water vapor in a set of steady-state measurements that reveal a systematic dependence on pressure. We derive a model for this behavior based on Langmuir adsorption and Shockley-Read-Hall recombination principles to describe how luminescence is modulated by partial pressure. The expression for the GaInP<sub>2</sub>/water vapor model system shows excellent agreement to measurements.

#### Introduction

Understanding semiconductor surface defects and controlling their populations is critical to the development and performance of solid-state electronic devices. Some mitigation strategies include gas-phase processing steps to passivate defect states manifested as dangling bonds or surface oxides that cause Fermi-level pinning and/or non-radiative recombination losses [1][2][3]. Chemical sensors and chemical field-effect transistors (ChemFETs) show luminescence that is modulated by a reversibly adsorbing species [4][5]. Reshchikov [6] showed

---

<sup>1</sup> Manuscript by Young, J.L., Döscher, H., Turner, J.A., and Deutsch, T.G. titled "Reversible GaInP<sub>2</sub> surface passivation by water adsorption: A model system for ambient-dependent photoluminescence" was submitted to Applied Physics Letters and is currently under revision.

that GaN photoluminescence (PL) responds reversibly and described a model where adsorbed oxygen induces surface states to reduce radiative recombination. Liu et al. [5] fabricated ZnO oxygen sensors whose PL decreases with increasing oxygen partial pressure and attributed it to dissociative adsorption on surface defects. Kocha et al. [7] observed a PL increase after etching GaInP<sub>2</sub> in sulfuric acid but did not consider any effect of performing the measurement in air. Furthermore, none of these earlier reports suggested a quantitative model for the dependence of PL intensity on ambient pressure.

Here, we show that the PL enhancement of GaInP<sub>2</sub> only persists in air (or other humid ambient) and depends systematically on the partial pressure of water. The model derived here is important not only to solid-state electronic devices, but also is critically important to water-splitting devices where GaInP<sub>2</sub> operates in contact with an aqueous electrolyte [8] [9]. Such systems demonstrate record 12%–14% solar-to-hydrogen conversion efficiencies and are capable of the maximum practical 25% [10]. The interaction of water and oxygen with photoelectrodes has significant implications for photocatalysis, photovoltage, and photocorrosion [11][12][13].

## Experimental

We perform PL measurements of GaInP<sub>2</sub> in both air and controlled gas-phase ambient defined by the vacuum and control systems of an atomic layer deposition (ALD) reactor [14] modified for *in situ* PL monitoring. An attachment houses a vertically oriented sample stage positioned ~1 cm behind a ConFlat<sup>®</sup>-mounted 1"-diameter quartz window while pneumatic and leak valves introduce and maintain water vapor, oxygen, or air pressure measured by a Baratron<sup>®</sup> capacitance manometer. A collimated laser diode (ThorLabs) with center wavelength  $\lambda = 532$  nm adjusted to 0.25 mW provides illumination that an objective lens outside the window focuses on

the sample while collecting PL. With  $\sim 100\text{-}\mu\text{m}$  spot size, the illumination intensity of  $3\text{ W/cm}^2$  is considerably higher than necessary for flat-band conditions [15] where surface-charge effects are compensated [16]. For example, flat-band potential measurements on GaAsPN saturate with only  $0.6\text{ W/cm}^2$  [17]. A dichroic mirror (ThorLabs) with 50% transmission/reflection at  $\lambda = 567\text{ nm}$  separates reflected illumination from the PL signal, which is centered and constant at  $\lambda = 661\text{ nm}$  (Figure 4.1.1a), allowing peak height to serve as the parameter for PL intensity when monitoring it in changing ambient. Two-micron-thick  $\text{Ga}_{0.51}\text{In}_{0.49}\text{P}$  ( $\text{GaInP}_2$ ) epilayers that are Zn-doped  $p$ -type to  $1 \times 10^{17}\text{ cm}^{-3}$  were grown on degenerately Zn-doped (001) GaAs substrates miscut  $2^\circ$  toward (110) by ambient pressure organometallic vapor-phase epitaxy (AP-OMVPE). Samples were etched for 2 min in concentrated sulfuric acid with a sequence of solvent rinses (deionized water, acetone, methanol, deionized water) and blown dry with a nitrogen gun before and after etching.

## Results and model development

Figure 4.1.1a shows that the etching treatment enhances PL relative to unetched samples when PL measurements are performed in air. The enhancement slowly decays by  $\sim 20\%$  over 5 min in air (Figure 4.1.1b, green trace). However, evacuating air after 1 min causes a rapid drop in the PL intensity (Figure 4.1.1b, gray trace) that approaches that of the unetched sample. Notably, the emission intensity of the unetched sample was unperturbed by vacuum (Figure 4.1.1b, black trace), suggesting that the observed PL enhancement results from interaction of the surface with air (oxygen and/or water).

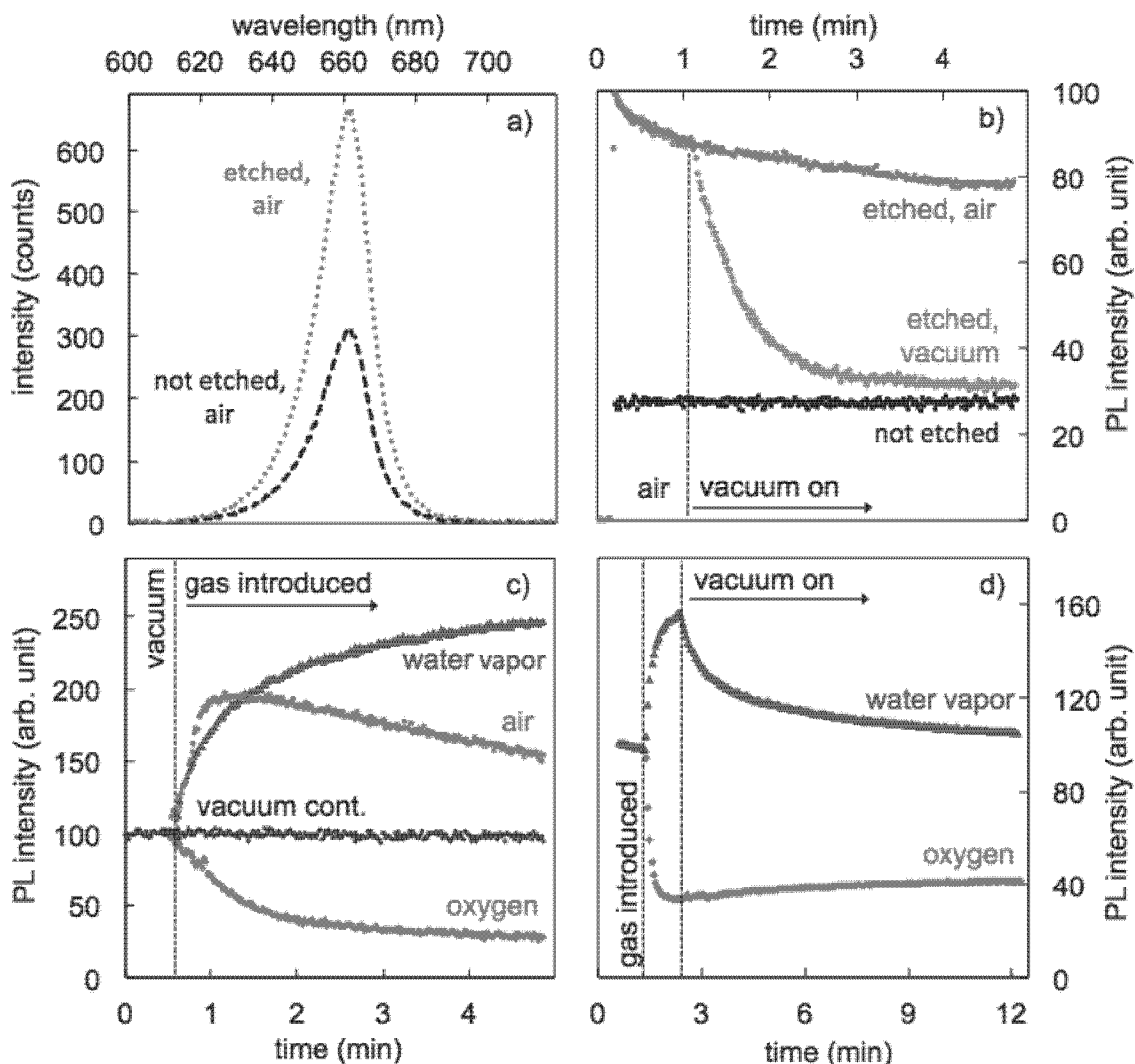


Figure 4.1.1: (a) Band-to-band PL spectrum of GaInP<sub>2</sub> as measured in air ambient before (black) and after (green) etching in concentrated sulfuric acid. (b) The PL intensity response of as-received (black) and etched (gray) GaInP<sub>2</sub> during air-to-vacuum transition as well as the PL intensity of etched GaInP<sub>2</sub> continuously monitored in air (green). (c) Starting from vacuum, PL is monitored while introducing air (green), oxygen (red), and water vapor (blue). The PL continuously monitored in vacuum (black) is stable. (d) Response to water vapor (blue) is reversible and oxygen (red) is irreversible upon evacuation.

The PL intensity remains stable for two days in air when taking measurements intermittently (similar to Kocha et al. [7]) but decays during continuous measurement, indicating higher GaInP<sub>2</sub>/air reactivity under illumination.

To probe the effect of the individual components of air on the PL intensity, experiments were conducted to expose GaInP<sub>2</sub> to vacuum, oxygen, water vapor, and air. Figure 4.1.1c shows that etched GaInP<sub>2</sub> PL is stable in vacuum (black), increases in the presence of water vapor (blue), decreases in oxygen (red), and first increases for 30 s and then decays in air (green). Because air contains oxygen and water vapor, we attribute the initial PL increase to adsorbed water and the subsequent decay to oxygen. We exposed another etched GaInP<sub>2</sub> sample and followed with evacuation (Figure 4.1.1d) to show that the PL response to water vapor (blue) is reversible and to oxygen (red) is irreversible. Longer evacuation times (~20 min) are necessary for complete reversibility, as will be shown. By avoiding the irreversible effect of oxygen exposure, we characterize the pressure-dependent PL response of GaInP<sub>2</sub> to water vapor necessary to validate our model.

We expand on Reshchikov's [6] description of oxygen-induced traps on GaN to derive a quantitative model based on principles of Langmuir adsorption [18] and Shockley-Read-Hall (SRH) carrier recombination [19][20]. Both concepts illustrated in Figure 4.1.2 apply to luminescent semiconductors reversibly passivated by a gas-phase adsorbate in general. Reversibility is necessary to achieve a modulated response from gas sensors and ChemFETs and is desirable for catalytic surfaces such as GaInP<sub>2</sub> photoelectrodes, where interactions of intermediate strength are optimal as suggested by Sabatier's principle. Irreversible passivation is desirable in other solid-state devices for which PL monitoring and associated kinetic models could be developed; but here, we limit our scope to reversible adsorption.

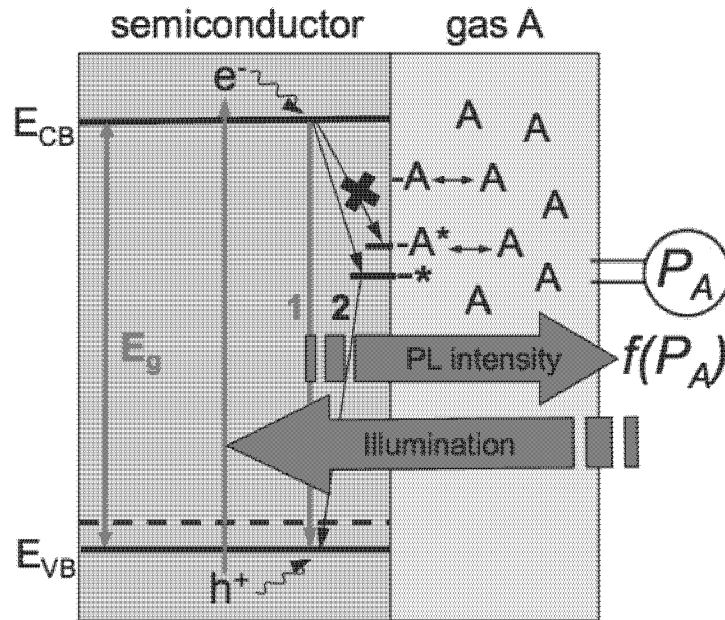


Figure 4.1.2: Semiconductor with conduction and valence band energies ( $E_{CB}$ ,  $E_{VB}$ ) and surface defect (\*) population exposed to gas A with partial pressure  $P_A$  adsorbing reversibly as  $A^*$ . Recombination is radiative (1) yielding PL or non-radiative (2) mediated by a surface defect.  $P_A$  modulates  $A^*$  and  $*$  populations, and thus the frequency of (1) and (2), making PL intensity a function  $f(P_A)$ .

Langmuir [18] described how steady-state adsorbate populations depend on ambient pressure while SRH related [19][20] carrier recombination rates to defect populations. The following derivation shows how these concepts are related when an adsorbate passivates or induces surface defects. At steady state, the total carrier generation rate  $G_T$  [ $s^{-1}$ ] in a semiconductor is equal to total recombination rate  $U_T$  occurring in the bulk  $U_B$  or at the surface  $U_S$  and is either radiative (subscript R) or non-radiative (subscript NR):

$$G_T = U_T = U_B + U_S = (U_{B,R} + U_{B,NR}) + (U_{S,R} + U_{S,NR}). \quad (1)$$

We neglect  $U_{B,NR}$  being small for luminescent semiconductors (may be constant for others) and  $U_{S,R}$  because  $U_{S,NR}$  is dominant at surfaces, giving:

$$G_T = U_{B,R} + U_{S,NR}. \quad (2)$$

Recombination rates [ $s^{-1}$ ] at surfaces are proportional to excess carrier concentration near the surface  $n'_s$ , surface recombination velocity  $S$ , and area  $A$  [21]. Given a flat-band condition,  $n'_s$  is equal to the bulk carrier concentration  $n'$ , which we write in terms of the total number of excess electrons  $N_e = n'V$ , giving:

$$U_{B,R} = G_T - An'S = G_T - A \frac{N_e}{V} S = G_T - \frac{N_e}{d} S. \quad (3)$$

The band-to-band luminescence is the source of a PL signal; but in practice,  $U_{B,R}$  is not measured directly. A fraction  $C_1$  of  $U_{B,R}$  will escape the sample, of which a fraction  $C_2$  is detected depending on collection efficiency and systems throughput. We let  $C_0 = C_1 C_2$  to relate detected luminescence intensity  $PL_{det}$  to  $S$  while applying the relation  $N_e = G_T \tau$ , where  $\tau$  is the bulk carrier lifetime, to get:

$$PL_{det} = C_0 \left[ G_T - \frac{G_T \tau}{d} S \right] \quad \text{or} \quad S = \frac{d}{\tau} \left[ 1 - \frac{PL_{det}}{G_T C_0} \right]. \quad (4)$$

The parameter  $S$  is equal to  $v_{th} \sigma_n N_t$ , where  $v_{th}$ ,  $\sigma_n$ , and  $N_t$  are carrier thermal velocity, trap capture cross-section, and the number of surface traps, respectively. When the presence of an adsorbate activates or deactivates a trap,  $S$  changes proportionally with  $N_t$ , which has a maximum value  $N_{sites}$ . A fraction  $\theta_{active}$  of  $N_{sites}$  are active such that  $N_{active} = N_{sites} \theta_{active}$ , making  $S$  a function of  $\theta_{active}$ . The maximum value of  $S$  occurring when  $\theta_{active} = 1$  is a constant  $S_{max} = v_{th} \sigma_n N_t = v_{th} \sigma_n N_{sites} \theta_{active} = S_{max} \theta_{active}$ .

$$S = v_{th} \sigma_n N_t = v_{th} \sigma_n N_{sites} \theta_{active} = S_{max} \theta_{active}. \quad (5)$$

Next, we consider two cases where the presence of an adsorbate either activates or passivates surface traps. Reschikov [6] and Liu et al. [5] report that oxygen decreases luminescence whereas we showed here that water vapor passivates GaInP<sub>2</sub>. Thus, two cases are possible where

$\theta_{active}$  is equal to the fraction of occupied sites  $\theta_{occupied}$  or the fraction of unoccupied sites

$1 - \theta_{occupied}$ :

Case A) trap active when occupied, decreasing  $PL_{det}$  ( $\theta_{active} = \theta_{occupied}$ ) or

Case B) trap inactive when occupied, increasing  $PL_{det}$  ( $\theta_{active} = 1 - \theta_{occupied}$ ).

Finally, we consider the nature of the adsorption reaction in order to select an appropriate adsorption isotherm function  $\theta_{occupied} = f_{AD}(P)$ , where  $P$  is partial pressure. Alternatively, one could compare the quality of fit to data for several different  $f_{AD}$  to determine its nature. Figure 4.1.2 illustrates a reversible process where A adsorbs to passivate one surface trap \* as the adsorbed molecule A\*, which is described by the molecular isotherm  $f_{AD,M}$ :

$$\theta_{occupied} = f_{AD,M}(P) = \frac{\alpha P}{1 + \alpha P}, \quad (6)$$

where  $\alpha$  is the adsorption reaction equilibrium constant [22]. A dangling bond (unpaired electron) is a common type of surface trap that is passivated by a bonding reaction. This implies that a bond in A breaks (dissociates) and forms two species that may both adsorb such that the dissociative isotherm  $f_{AD,D}$  depends on  $P^{1/2}$  [22]:

$$\theta_{occupied} = f_{AD,D}(P) = \frac{\alpha P^{1/2}}{1 + \alpha P^{1/2}}. \quad (7)$$

Liu et al. [5] suggested that competition between oxygen and water for surface sites could help explain a temperature dependence in their results. Here, a competitive adsorption isotherm [22] should be applied. A number of other theoretical and empirical isotherms, such as those described by Keller and Staudt [23], may be considered for other systems. We summarize the derivation in the following key relationships:

1) Eq. 4 shows that S can be written in terms of  $PL_{det}$ :

$$PL_{det} = C_0 \left[ G_T - \frac{G_T \tau}{d} S \right] \quad \text{or} \quad S = \frac{d}{\tau} \left[ 1 - \frac{PL_{det}}{G_T C_0} \right]. \quad (4)$$

2)  $S$  depends on  $N_{traps}$ , which we write in terms of  $\theta_{active}$ :

$$S = v_{th}\sigma_n N_{sites}\theta_{active} = S_{max}\theta_{active} \quad (5)$$

3) Adsorbed species may activate or passivate surface traps. The relationships relevant to each case are:

A) passivation increases PL and  $\theta_{active} = 1 - \theta_{occupied} = 1 - f_{AD}(P)$

B) activation decrease PL and  $\theta_{active} = \theta_{occupied} = f_{AD}(P)$

4) The dependence of  $PL_{det}$  on  $P$  is fit by incorporating isotherms ( $\theta_{occupied} = f_{AD}(P)$ )

such as Eq. 6 or Eq. 7.

Combining these relationships, we model our GaInP<sub>2</sub>/water vapor system with

$$PL_{det} = G_T C_0 \left[ 1 - \frac{\tau}{d} S_{max} (1 - f_{AD}(P)) \right], \quad (8)$$

while comparing molecular (Eq. 6) and dissociative (Eq. 7) adsorption isotherms used for  $f_{AD}(P)$ .

We measure GaInP<sub>2</sub>  $PL_{det}$  at fixed illumination for a set of water-vapor partial pressures  $P$  in Figure 4.1.3a. The inset shows that exposing GaInP<sub>2</sub> to water vapor ( $P = 36$  mTorr, ~15 min) results in a stabilized  $PL_{det} = 380 \pm 0.4$  counts and  $PL_{det}$  returns to its original level after evacuating for 15–20 min. Similar measurements at increasing  $P$  up to 2.6 Torr are shown on the left axis while  $S$  calculated from  $PL_{det}$  with Eq. 4 is plotted on the right axis for  $\tau = 100$  ns. To obtain  $G_T C_0$  necessary to calculate  $S$ , we note that the maximum theoretical value of  $PL_{det}$  is  $G_T C_0$  and occurs in the limit of high  $P$  ( $\theta_{occupied} = 1$ ), where all surface traps are passivated. Measurements at  $P$  above the saturation vapor pressure may compromise  $PL_{det}$  due to optical distortion of condensed water. Instead, we use the best fit of Eq. 8 to calculate  $G_T C_0 = 722$  counts in the limit of high  $P$ , giving  $\alpha = 3.1$ . Because  $\alpha > 1$ , adsorption is favorable, which has been predicted by Wood et al. [11] for InP and observed by Zhang et al. [24] for GaP.

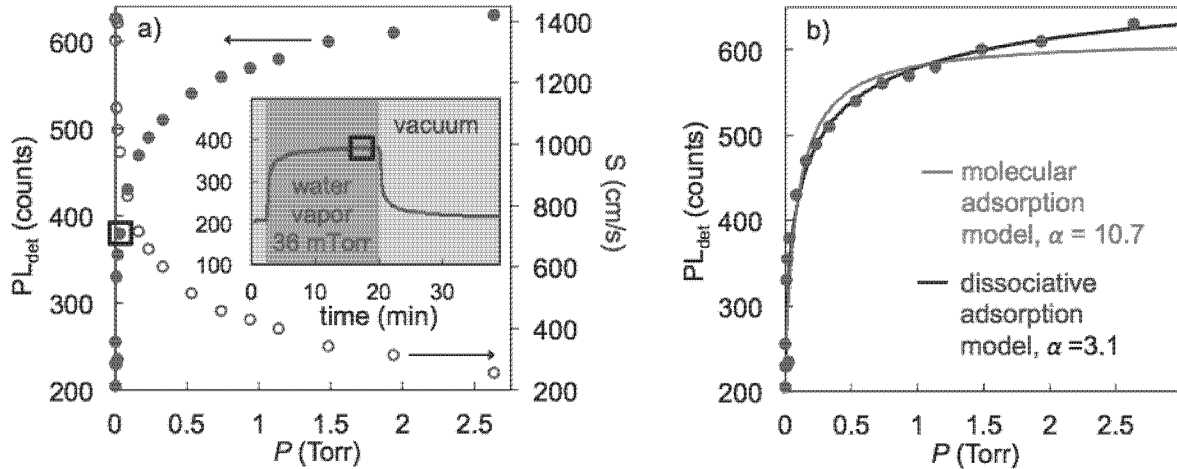


Figure 4.1.3: (a) The  $PL_{det}$  measurements are plotted vs. water-vapor partial pressure  $P$  (dots, left axis). The inset shows a measurement sequence for  $P = 36$  mTorr, where  $PL_{det}$  value is the average over 1 min after stabilization (black square) plotted in the main figure (black square).  $S$  was calculated (circles, right axis) from  $PL_{det}$  using Eq. 4 and  $\tau = 100$  ns. (b)  $PL_{det}$  is again plotted vs.  $P$  comparing best fits of the Eq. 8 model using either a molecular (Eq. 6, black line) or dissociative (Eq. 7, red line) adsorption isotherm for  $f_{AD}(P)$ .

This is illustrated in Figure 4.1.3 by the strong dependence of  $PL_{det}$  at low  $P$ , where half the surface traps are populated ( $\theta_{occupied} = 0.5$ ) at only 0.2 Torr. The better fit to Eq. 8 (Figure 4.1.3b) for the dissociative isotherm would imply that both -H and -OH passivate surface traps because dissociation where only one species passivates defects would behave as molecular adsorption. In the limit of low  $P$  ( $\theta_{occupied} = 0$ ), where all surface traps are active, we measure  $PL_{det} = 205$  counts, and using  $G_T C_0 = 722$  counts from above, Eq. 8 shows that  $S_{max}$  can be written in terms of  $\tau$  as  $S_{max}\tau = 0.72 \cdot d$ , where  $d = 2 \mu\text{m}$ , giving  $S_{max} = 1432$  cm/s for  $\tau = 100$  ns. Because  $S_{max} = \sigma_s v_{th} N_{sites}$  and  $v_{th}$  depends only on temperature, further measurements, analysis, or assumptions could be made to obtain  $\sigma_s$  or  $N_{sites}$ . The calculation of  $S$  from Eq. 4 requires an estimate of  $\tau$  from literature ( $\tau = 100$  ns) [25] but illustrates our key point that ambient can systematically modulate  $PL_{det}$  through  $S$ . Thus, we expect measurements

that inherently convolute  $\tau$  and  $S$  as an effective lifetime [26] may be deconvoluted when  $S$  can be varied independently.

## Discussion

Langmuir adsorption and SRH recombination principles may also be applied to semiconductors where  $U_{B,NR}$  is constant rather than negligible. An alternate derivation may account for  $U_{B,NR}$  as another term subtracted from  $G_T$  in Eq. 2, and a model similar to Eq. 8 would result where its fit to  $PL_{det} = f(P)$  measurements can help evaluate the nature of adsorption while quantifying  $\alpha$ . Additionally, characterizing the measurement system constants  $C_0$  and  $G_T$  would allow  $U_{B,NR}$  to be quantified. Oxide systems such as ZnO/O nanorods studied by Liu et al. [5] may have significant  $U_{B,NR}$ , but such a nanoscale system with high ratio of surface area to volume may still have negligible  $U_{B,NR}$ . Their data suggest that ZnO PL intensity is linear over much of the oxygen partial-pressure range, but two data points at low pressure show a stronger dependence. Such behavior is characteristic of adsorption isotherms that appear linear over a large range of higher pressures (see Figure 4.1.3b). The conceptual model for GaN/O suggested by Reshchikov [6] includes recombination pathways that contribute to  $U_{B,NR}$  and competing channels in a near-surface region that may require additional recombination-rate terms in Eq.2. Regardless,  $PL_{det} = f(P)$  fit with adsorption isotherms can help evaluate the nature of adsorption and quantify  $\alpha$ .

PL measurements are relatively simple among techniques that are surface sensitive, requiring only an excitation source, spectrometer, minimal optics, and line of sight to the sample. However, PL is not inherently quantitative unless combined with a model. Connecting adsorption models to surface defect population describes why and how  $S$  is modulated by

ambient pressure. Varying  $S$  quantitatively could also provide a way to delineate surface and near-surface (or bulk) recombination effects to help explain phenomena such as GaN yellow-band luminescence as discussed by Izpura [27]. The simplicity of PL monitoring and value of a quantitative model could be especially useful when applied in concert with techniques that characterize adsorbed species such as infrared spectroscopy [28], ambient pressure X-ray photoelectron spectroscopy [24][29], or reflection anisotropy spectroscopy [30][31].

## Conclusion

We clarify that the enhancement and subsequent decay of GaInP<sub>2</sub> PL after etching in concentrated sulfuric acid [7] depend on the reversible reaction with water vapor and irreversible reaction with oxygen. We derived a relationship between PL intensity and the partial pressure of adsorbates that reversibly passivates surface defects. A linear combination of terms describes the dependence of PL intensity  $PL_{det}$  on the fractional surface coverage  $\theta_{occupied}$ , which we related to ambient pressure using adsorption isotherms. The model was validated with the water vapor/GaInP<sub>2</sub> reversible adsorption system that is important to high-performance solar water-splitting.

## 4.2 Remarkable stability of unmodified GaAs photocathodes<sup>1</sup>

### Introduction

Established targets for solar-to-hydrogen (STH) efficiency, operating lifetime (stability), and absorber cost must be met before progress can be made toward large-scale, commercially viable photoelectrochemical (PEC) devices and systems that generate hydrogen (H<sub>2</sub>) fuel from sunlight and water [1]. PEC electrodes and devices based on III-Vs have demonstrated high performance enabled by exceptional solid-state properties: direct bandgaps in the visible range, high absorption coefficients, long carrier lifetimes, and high mobilities. Khaselev and Turner also identified the stability challenges of semiconductors in PEC configurations that operate in contact with strongly acidic or basic electrolytes [2], as necessary to minimize solution conductivity losses and pH gradient overpotential [3]. GaAs is frequently used as the substrate in III-V epitaxy and as one of the absorbers in multi-junction photovoltaic (PV) devices. Its use as a substrate and bottom absorber in a monolithic, hybrid PV/PEC tandem with a lattice-matched top GaInP<sub>2</sub> PEC junction achieved a record 12.4% STH efficiency, but with limited stability [2]. A number of reports on the PEC stability of III-Vs exist [4][5][6][7], including those specific to p-GaAs in acid [8][9], which has led to a perception that GaAs and other high-performance photoelectrodes are generally unstable [10][11]. We held a similar perception [12] until recently re-evaluating the stability of unmodified, epitaxial p-GaAs used as control samples for our work on protective surface modification of III-V photocathodes [13]. Using a portfolio of

---

<sup>1</sup> Manuscript by Young, J.L., Steirer, K.X., Dzara, M.J., Turner, J.A., and Deutsch, T.G. titled "Remarkable stability of unmodified GaAs photocathodes during hydrogen evolution in acidic electrolyte" accepted for publication in J. Mater. Chem. A.

photoelectrode durability characterization techniques, we present a clear example showing that p-GaAs photocathodes can have remarkable stability.

## Experimental

We performed PEC durability testing and characterized the photocathodes using microscopy, profilometry, elemental analysis of testing electrolytes, and X-ray photoelectron spectroscopy (XPS) measurements to evaluate the stability of p-GaAs. Two  $\mu\text{m}$ -thick epitaxial GaAs Zn-doped p-type to  $10^{17} \text{ cm}^{-3}$  were grown by organometallic vapor-phase epitaxy on 3"-diameter degenerately p-doped GaAs(100) substrate wafers  $4^\circ$  offcut toward 111B. Ohmic contacts were made to the back by evaporating Ti/Au. The wafer was then cleaved into  $\sim 8 \times 8$ -mm squares to be used as photocathodes. PEC characterization and durability testing were performed in a custom compression cell (Ch. 2.3). We performed the durability tests using a compression cell because the easy disassembly facilitates post-durability analysis. The cell body was filled with 3M  $\text{H}_2\text{SO}_4$  with 1 mM Triton X-100 (both OmniTrace® EMD Millipore) surfactant added to expedite  $\text{H}_2$  bubble evolution. Because surfactant improves stability [14], we compare p-GaAs to p-GaInP<sub>2</sub> here and to p-InP from past work [13]; all tested in the same electrolyte solution with added surfactant. A 1-cm x 2.5-cm Pt foil counter electrode (anode) was contained in a glass tube with a medium-porosity glass frit end that was inserted into a port on the PEC cell body. The glass tube was filled with the same 3M  $\text{H}_2\text{SO}_4$  but without surfactant, a practice we found to mitigate counter electrode fouling and solution yellowing previously observed by our group [13], presumably due to surfactant degradation at the anode. We used a Hg/HgSO<sub>4</sub> reference electrode (MSE) from Koslow Scientific Co. having a reference potential of 0.634 V vs. normal hydrogen electrode (NHE). Its filling solution being the same as the

electrolyte (3M H<sub>2</sub>SO<sub>4</sub>) eliminates concentration gradients that would cause the reference potential to drift over long-term testing. We note that stability testing was also performed in a variety of configurations: epoxy-mounted electrodes [12] instead of a compression cell, without a glass frit separating the photocathode from the counter electrode, and with Zonyl FSN-100 fluorosurfactant instead of Triton X-100—all with excellent results—showing that stability is independent of these testing conditions. The illumination source was a 250-W quartz tungsten halogen lamp with water filter and light-shaping diffuser (Newport) with intensity set to match the current from a Si reference cell calibrated to an AM1.5G spectrum. The p-GaAs durability testing was performed at a constant -15 mA/cm<sup>2</sup> current while continuously monitoring the working electrode's potential vs. MSE. Chopped-light current-voltage (CLIV) measurements were taken before and after each durability test with the voltage scanned at 20 mV/s while blocking/unblocking the light source at 0.1-V intervals. The electrolyte analyzed for dissolved Ga and As by inductively coupled plasma mass spectrometry (ICP-MS) and the quantity detected (in ppb) was converted to nanomoles. The surface profiles were measured with both optical (Veeco) and stylus (Dektak 8 with 5- $\mu$ m tip) profilometry and the surface morphology was examined with a JEOL JSM-7000F scanning electron microscope (SEM) equipped with energy-dispersive X-ray spectroscopy (EDS).

## Results

We performed baseline chemical stability testing of p-GaAs in the dark at open circuit for 96 hours. Stereomicroscopy showed a pristine surface and profilometry showed negligible etching. The lack of etching is unexpectedly different than the statement by Walczak et al. that high-performance photoelectrodes such as GaAs would dissolve quickly in electrolyte solution

near pH 0 [11]. This intrinsic chemical stability is important to survive the diurnal cycle of solar radiation and demonstrates that the corrosion resistance is not exclusively due to cathodic protection [15] [16]. Figure 4.2.1a shows CLIVs performed before durability testing that have a light-limited photocurrent (LLPC) of  $-22 \text{ mA/cm}^2$  and photocurrent onset potential of  $-0.7 \text{ V vs. MSE}$ . After durability tests lasting 72 and 120 h, the p-GaAs shows a slight cathodic shift in photocurrent onset potential, but also a slight increase in fill factor due to the steeper rise in photocurrent.

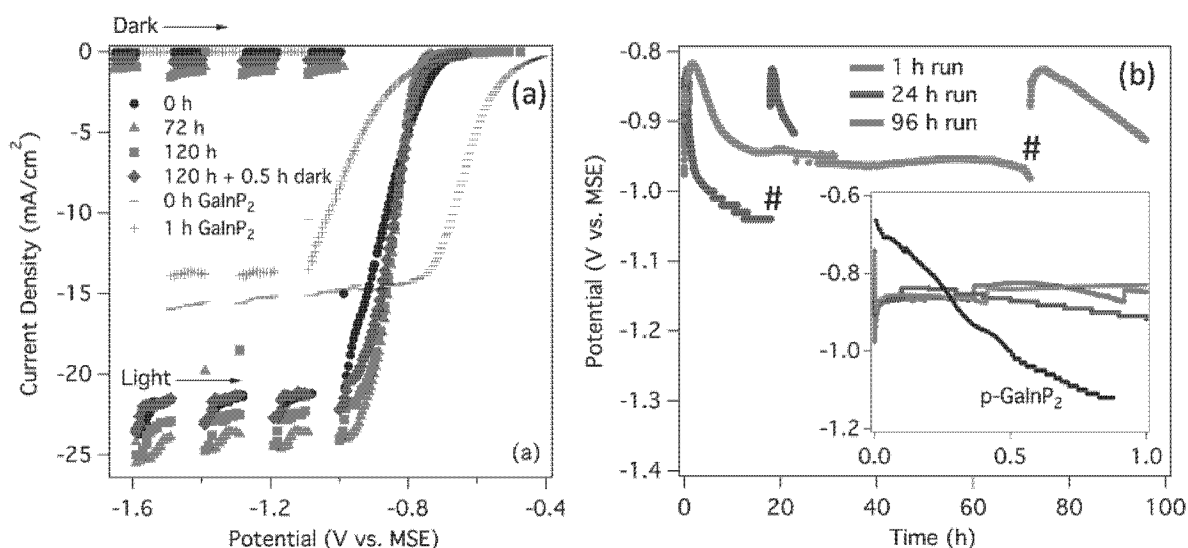


Figure 4.2.1 (a) CLIV characterization of p-GaAs photocathodes before (0 hr, black dots), after 72 hr (green triangles), and 120 hr (red squares) galvanostatic durability testing at  $-15 \text{ mA/cm}^2$ . The 120 hr sample was measured again after 0.5 hr at open circuit in the dark (blue diamonds). This is compared to a p-GaInP<sub>2</sub> photocathode before (0 hr) and after 1 hr durability testing. The "Light" and "Dark" labels indicate, respectively, the current measured under illumination and with the illumination blocked. (b) The p-GaAs potential monitored vs. MSE during durability testing for separate of samples tested for 1 hr (red), 24 hr (blue), and 96 hr (green). The durability tests paused at OCP and restarted are indicated at "#". The inset shows the first hour of testing compared to p-GaInP<sub>2</sub> (black).

This compares to a p-GaInP<sub>2</sub> photocathode before (0 h) and after just a 1 h durability test at  $-10 \text{ mA/cm}^2$ , which showed a large cathodic shift in photocurrent onset potential ( $-400 \text{ mV}$ ) and a  $2\text{--}3 \text{ mA/cm}^2$  decrease in LLPC. The small increase in p-GaAs current density at 72 and 120 h is, in part, due to a small amount of dark current ( $1\text{--}2 \text{ mA/cm}^2$ ), but also due to increased light

absorption discussed later. After letting the sample tested for 120 h sit in the dark in electrolyte at open circuit for 0.5 h, the dark current was reduced and the LLPC closely matched the CLIV taken before durability testing (0 h). Figure 4.2.1b shows the potential of the p-GaAs photocathodes monitored vs. MSE throughout galvanostatic durability testing at  $-15 \text{ mA/cm}^2$ . The p-GaAs starts out at  $-0.9 \text{ V vs. MSE}$ , matching the operation point of the CLIV in Figure 4.2.1a, and then became 50–100 mV more positive during the first 1–2 hours before increasing in magnitude and stabilizing around  $-1 \text{ V vs. MSE}$  over the next 10 hours. The 24 h and 96 h runs were stopped and restarted at 18 h and 72 h, respectively, as indicated by the '#' marker. Upon restarting after less than one minute rest time, the operating potentials recovered to their initial  $-0.9 \text{ V vs. MSE}$  operating point and again improved  $\sim 50 \text{ mV}$  over the next hour before slowly increasing in magnitude over the next few hours.

The sample tested for 120 hours was photographed with a stereomicroscope, characterized with optical and stylus profilometry, and examined with SEM (Figure 4.2.2). Figure 4.2.2a shows a stereoscope image of the p-GaAs with the active photocathode area encircled by a black dotted line. The perimeter that was under or outside of the washer during testing is specular; whereas the majority of the active region has a darker, slightly brown appearance except at the top, where a lip created by the washer would accumulate some  $\text{H}_2$  bubbles. Optical profilometry (Figure 4.2.2b) was taken with the reference height established by the unexposed perimeter (green), and it showed minimal etching throughout the lower two-thirds of the active region and some etching in the upper right, perhaps due to higher current densities associated with its proximity to the counter electrode.

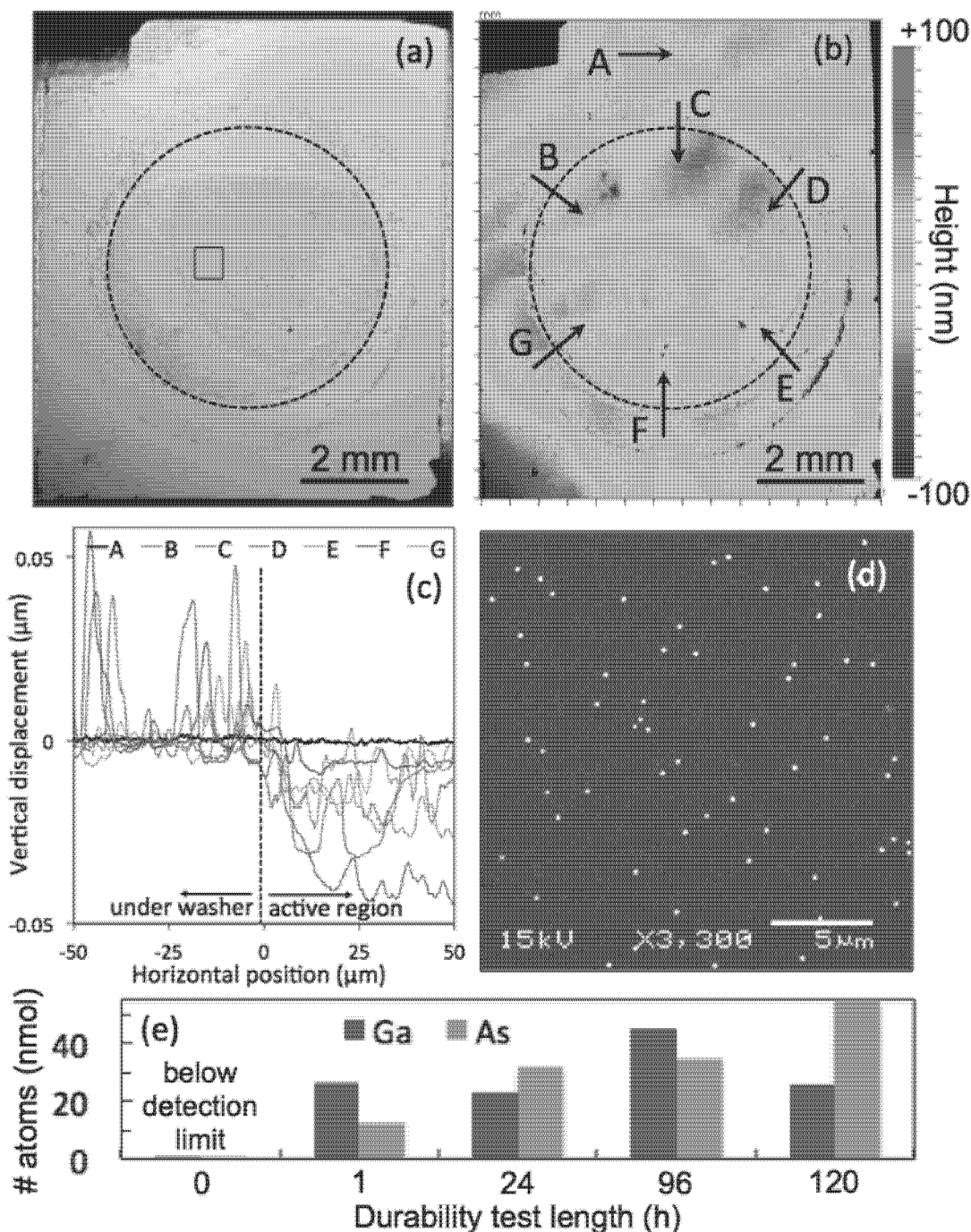


Figure 4.2.2 (a) Stereoscope image after 120 hr testing with active region encircled by black dashed line. (b) Optical profilometry with height scale from -100 nm (dark blue) to +100 nm (dark red). (c) Stylus profilometry scans in the locations/directions indicated by letters A-G and arrows on (b). (d) SEM image of the active region at the location indicated with a black square in (a). (e) Quantification by ICP-MS in nanomoles (nmol) of Ga and As in the electrolyte after durability testing.

Etch profiles were confirmed with stylus profilometry (Figure 4.2.2c) scanned from the perimeter into the active region at the locations indicated by letters A–G in Figure 4.2.2b. The etch depths ranged from 5–45 nm and revealed a texture with amplitude 5–15 nm in the active region. This etch rate ( $<0.5$  nm/h) for p-GaAs is remarkably low compared to the etch rate of unmodified p-GaInP<sub>2</sub> at  $-10$  mA/cm<sup>2</sup> (40–80 nm/h) and unmodified p-InP at  $-25$  mA/cm<sup>2</sup> (170 nm/h) where 1–2  $\mu$ m for p-GaInP<sub>2</sub> [17] and 4  $\mu$ m of p-InP [13] were removed within 24 h. An etch rate two orders of magnitude lower than other unmodified III-Vs is significant. The darker appearance of the p-GaAs region exposed to electrolyte (Figure 4.2.2a) and texturing (Figure 4.2.2c) suggest the presence of antireflective properties, which corroborates with the higher LLPC measured after durability testing (Figure 4.2.1a). The larger texture in the region that was underneath the washer was determined by EDS to be carbon particles, likely residue of carbon black which is a filler used in perfluoroelastomers such as Kalrez®. The texturing within the active region appears to correspond with a dispersion of particles (bright dots) observed with SEM (Figure 4.2.2d). Although not surface sensitive, EDS indicated that the active region is  $\sim 2$  at. % points more As-rich compared to the 50:50 at. % GaAs stoichiometry of the area outside of the washer.

To evaluate the surface composition, XPS was used to characterize p-GaAs surfaces after 1, 24, and 96 h (Figure 4.2.1b) of durability testing. After PEC testing, samples were extracted from the PEC cell in an Ar-filled glove box to eliminate exposure to air. XPS was performed using a Physical Electronics 5600 photoelectron spectrometer with monochromatic Al K $\alpha$  excitation (pressure  $< 2 \times 10^{-10}$  torr). Multipoint binding-energy calibration followed M.P. Seah for Au 4f<sub>7/2</sub>, Ag 3d<sub>5/2</sub> and Cu 2p<sub>3/2</sub> peak centroids [18]. Pass energy was 11.75 eV. Compositions were calculated using Multipak software values. Two baseline samples were included for

comparison. The first sampled, labeled "solvent wash" in Figure 4.2.3, was rinsed with acetone, methanol, and then submerged in Ar-sparged deionized (DI) water before transferring to ultra-high vacuum (UHV). The second sample was similarly cleaned and then soaked for 1 h in the PEC electrolyte before rinsing and transferring to UHV. XPS spectra for As 2p<sub>3/2</sub> (Figure 4.2.3), Ga 2p<sub>3/2</sub>, and O 1s (Figure S4) regions were analysed to develop an understanding of the changes induced under PEC conditions. Figure 4.2.3 shows the As 2p<sub>3/2</sub> spectral region deconvoluted with Gauss-Lorentz (80/20) and Shirley background model fits. Residuals are also shown. The high binding-energy (BE) core level regions were chosen for enhanced surface sensitivity because the photoelectrons detected from the Ga 2p<sub>3/2</sub> and As 2p<sub>3/2</sub> are emitted from the top 0.8–1.2 nm [19]. A summary of the modeled composition is reported in Table S1. Peak positions were restricted to within ±0.1 eV while simultaneously fitting all the spectra. Following literature, the As 2p<sub>3/2</sub> spectra (Figure 4.2.3) were fit with five peaks including lattice As (1322.7 eV), As<sup>0</sup> (1323.7 eV), As<sub>2</sub>O<sub>3</sub> (1325.8 eV), and a mixed oxide (1327.2 eV) whereas the As 2p<sub>3/2</sub> peak (1321.3 eV) was tentatively assigned to As dimers (1321.3 eV) following similar As 3d spectral features. Mixed oxides observed for Ga 2p<sub>3/2</sub> peak (1118.7 eV) and As 2p<sub>3/2</sub> peak (1327.2 eV) spectra are native oxides formed while exposed to air [20].

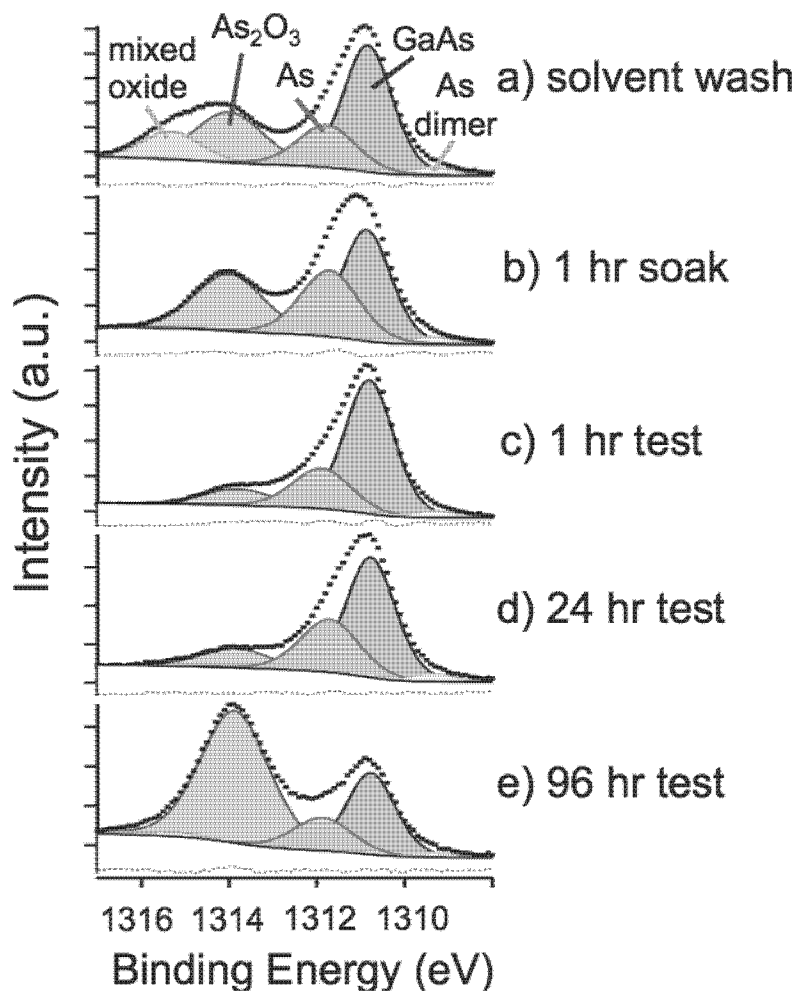


Figure 4.2.3: XPS spectra of the As  $2p_{3/2}$  core level is shown with the deconvoluted peak assignments. The two baseline samples were (a) solvent washed and (b) soaked in electrolyte for 1 hr. Three samples were durability tested for (c) 1 hr, (d) 24 hr, and (e) 96 hr before XPS measurements.

## Discussion

The evolution of the observed surface species and their electrochemical stability under the p-GaAs photocathode operating conditions can provide insight into the stabilization mechanism. Pourbaix provides pH-potential diagrams for Ga and As in contact with electrolyte [21]. For a pH = -0.5 (3M sulfuric acid), the thermodynamically preferred state of Ga is aqueous  $\text{Ga}^{3+}$  ions for potentials more positive than ca. -0.6 V vs. NHE (all subsequent potentials are vs. NHE unless otherwise stated), whereas atomic Ga is favored at more negative potentials. For As,

the stable and insoluble species at pH = -0.5 are  $\text{As}_2\text{O}_3$  for potentials 0.2 to 0.6 V and As for -0.5 to 0.2 V. From our observation of negligible etching after 96 h at open-circuit potential (OCP), we can conclude that the surface potential at OCP is within one of these stable ranges.

Furthermore, the surface potential at OCP must be within the water-splitting half-reaction potentials (0–1.23 V), which means that the stable Ga and As species are dissolved  $\text{Ga}^{3+}$  and either  $\text{As}_2\text{O}_3$  or As. In agreement, we observed that the native mixed oxide (potentially including  $\text{GaAsO}_4$ ,  $\text{Ga}_2\text{O}_5$ ,  $\text{As}_2\text{O}_5$ , and others) is removed by soaking in electrolyte for just one hour, leaving As and  $\text{As}_2\text{O}_3$  as the likely candidates for p-GaAs etch resistance at OCP (Figure 4.2.3a,b).

During  $\text{H}_2$  evolution, the surface potential is more negative than the hydrogen evolution reaction (HER) potential, but the potential at which electrons reach the electrolyte or conduction-band position is not known precisely due to the possibility of Fermi-level pinning/unpinning [22][23] or band-edge migration [24]. The operating pH is -0.5, but now may be slightly more positive in the near-surface region as protons are consumed at  $-15 \text{ mA/cm}^2$ . However, the high 3M bulk acid concentration and vigorous stirring of copious  $\text{H}_2$  bubbling at the surface limit significant deviation [25]. If we assume a kinetic overpotential for  $\text{H}_2$  evolution of less than 0.5 V on p-GaAs, the surface potential is within -0.5 V of the HER. Here, Pourbaix diagrams suggest that As, but not  $\text{As}_2\text{O}_3$ , is stable under  $\text{H}_2$  evolution, which agrees with the relative increase of As over  $\text{As}_2\text{O}_3$  in the samples that were durability tested for 1 h (Figure 4.2.3c) and 24 h (Figure 4.2.3d) compared to the sample soaked in electrolyte at OCP for 1 h (Figure 4.2.3b). At OCP, Ga will dissolve as  $\text{Ga}^{3+}$ , leaving As the more likely surface-stabilizing species. We note that if the surface potential is more negative than -0.5 V, Ga and  $\text{AsH}_3$  are the preferred species. Practically, such a large operating potential above HER is unsuitable because of the voltage loss

of the excess overpotential. Photocathodes modified with attached Pt catalysts may have  $< 100$  mV overpotential [26][27]; but full discussion of the intrinsic stability of unmodified p-GaAs includes consideration of high overpotential. Here, Pourbaix suggests that Ga rather than As could passivate the surface, and previously dissolved  $\text{Ga}^{3+}$  in solution could be reduced to Ga on the photoelectrode surface. Park and Barber's thermodynamic analysis of GaAs gives a narrow potential range for the stability of As, making this a more likely explanation for GaAs stability according to their analysis. However, As and  $\text{As}_2\text{O}_3$  on GaAs is a common experimental observation after etching in acid [28][29][30]. Our quantification of Ga and As in solution (Figure 4.2.2e) shows 2:1 and 1:2 Ga:As ratios for the shortest and longest durability testing times, respectively. This supports a model where excess As stabilizes the surface initially and some  $\text{Ga}^{3+}$  in solution is redeposited after 120 hours. However, a systematic trend connecting these endpoints though the intermediate durability testing times is not yet clear. A change in surface stoichiometry would imply that selective corrosion contributes to photocurrent if occurring as electrochemical reduction. We calculate that a 50 nm etch depth amounts to  $2.2 \times 10^{17}$  atoms removed (GaAs atomic density  $4.4 \times 10^{22} \text{ cm}^{-3}$  [31]) that contribute 3 electrons each to supply a total of 0.020 C toward corrosion reactions. During the 120 hr durability test at  $-15 \text{ mA/cm}^2$ , a total of 1,200 C pass through the  $0.185\text{-cm}^2$  photoelectrode. Therefore, the fraction of corrosion current is negligible at 17 parts per *million* of the photocurrent.

The stable species at OCP are relevant because the p-GaAs photoelectrode returns to OCP upon stopping the durability test. The electrode potential reverts to its original potential upon simply pausing and restarting the durability test (indicated by '#' in Figure 4.2.1b). We previously noted that  $\text{As}_2\text{O}_3$  should not form during hydrogen evolution but that As can convert to  $\text{As}_2\text{O}_3$  after stopping the durability test, both of which we detect with XPS. This is supported

by a brown appearance of the surface (Figure 4.2.1a) that Smeenk et al. also characterized as predominantly elemental As with a small signal from  $\text{As}_2\text{O}_3$ . We also consistently detected  $\text{Ga}_2\text{O}_3$  in all samples, which, in contrast to As and  $\text{As}_2\text{O}_3$ , the Pourbaix diagram for Ga shows that  $\text{Ga}_2\text{O}_3$  is only stable at more neutral pH values. The  $\text{Ga}_2\text{O}_3$  we observe may have formed from  $\text{As}_2\text{O}_3$  reacting with GaAs to form  $\text{Ga}_2\text{O}_3$  and elemental As, which are stable phases in contact with GaAs [29]. If the  $\text{Ga}_2\text{O}_3$  formed during operation, it is plausible that it is also protected, like GaAs, by the As overlayer. Alternatively, the gallium oxide may have also formed during the pH shift of the DI water rinse, as observed by Vilar et al. [29]. The likelihood of oxidation at OCP combined with surface roughness for long durability testing time (Figure 4.2.2a–d) explain the increased amount of  $\text{As}_2\text{O}_3$  (Figure 4.2.3e) and  $\text{Ga}_2\text{O}_3$  (Figure S4e) relative to As and Ga, respectively, detected after 96 hours.

The surface-stabilizing candidates of  $\text{As}_2\text{O}_3$  and As were identified for p-GaAs in pH = -0.5 at OCP. Under  $\text{H}_2$  evolution, As is a more likely candidate, but we noted that Ga rather than As is stable at surface potentials more negative than ca. -0.5 V. We discussed the likelihood that species detected that are not expected to be stable during operation ( $\text{Ga}_2\text{O}_3$  and  $\text{As}_2\text{O}_3$ ) formed after stopping the durability testing.

The observed stability of GaAs is remarkable and in strong contrast to  $\text{GaInP}_2$  and InP. Although the Pourbaix diagrams for Ga and In are similar, As contrasts with that of P where P is expected to form soluble phosphates or phosphites. When excess As is left at the GaAs|electrolyte interface, the photoelectrochemical junction may be better represented by a GaAs|As Schottky model. Here, the junction-forming layers responsible for photovoltage reside in the solid state. The GaAs|As|electrolyte multilayer structure affords stable performance while the As overlayer is thin enough to be highly transparent, thus maintaining high photocurrents.

We note it is important that As has a low work function (3.75 eV [32]) necessary to maintain a Schottky junction to p-GaAs, rather than a high work function that could cause an Ohmic contact and loss of photovoltage. We note that an electrochemical stability regime similar to that of As also exists for Sb and Bi in column V below As, but not for P and N above. III-V arsenide and the less studied III-V antimonide and bismide photocathodes warrant further investigation.

Although not explored here, impurities and crystal defects can enhance etch rates [33]–[36]; thus, variation in material quality could be responsible for the discrepancy among reports on the stability of GaAs. In going beyond the GaInP<sub>2</sub>/GaAs tandems that have demonstrated 12.4% STH, lower bottom and top absorber bandgaps are necessary [37], which will lead into exploration of other III-V ternary and quaternary alloys that incorporate GaAs (e.g., GaInAsP, InGaAs) and could also be stable. We do not expect intrinsic stability to alleviate the need for stabilizing photoelectrode surfaces with catalysts and/or coatings. However, high-performance photoelectrodes that exhibit *intrinsic stability* should be more robust templates for achieving the multi-year operational lifetimes necessary for commercially viable PEC devices.

## Conclusions

We characterized unmodified, p-GaAs photocathodes during hydrogen evolution in acidic electrolyte and found them to be remarkably stable—having two orders of magnitude slower etch rate than unmodified p-GaInP<sub>2</sub> and p-InP. This new finding among PEC corrosion studies is contrary to earlier reports and popular perception in the field toward universal instability of III-V high-performance photocathodes. We discussed a set of candidate species detected with XPS after durability testing that could contribute to stabilizing the p-

GaAs/electrolyte interface. Analysis supports that this remarkable corrosion resistance likely results from the formation of elemental As during PEC conditions.

### **4.3 Stabilizing GaInP<sub>2</sub> with nitridation and PtRu sputtering**

In this Chapter, we present recent progress in surface modification/treatment of III-V photocathodes for improved durability by providing corrosion resistance. Early work attempted stabilizing p-GaInP<sub>2</sub> surfaces by nitrogen ion implantation with exceptional success, surviving 115 h with no detectable degradation [32]. However, subsequent efforts to reproduce results were unsuccessful. Since then, it was discovered using XPS that trace Pt and Ru were present in addition to nitrogen species on the original, exceptionally stable samples [33]. The PtRu source was the sample stage, "contaminated" by unrelated experiments that led to inadvertent PtRu incorporation during our treatments. This explained why efforts to reproduce results that had been using a different chamber, which had a "clean" sample stage, were unsuccessful while revealing PtRu as a key component of the surface treatment. Further work established a standard two-part treatment procedure consisting of separate and sequential nitridation and PtRu sputtering steps intended to decouple the two processes, so that the effect of each on stability could be investigated.

#### **Treatment procedures**

We continue here by subjecting p-GaInP<sub>2</sub> photocathodes to treatment variations, quantifying Pt and Ru loading by inductively coupled plasma mass spectrometry (ICP-MS), and

characterizing their durability. We compare the "full" two-part treatment to individual sputtering-only and nitridation-only variations performed in a vacuum chamber in which samples are mounted on a stage within a rotating wheel[34] (Figure 4.3.1). The nitrogen source is an ion gun which is fixed and pointed at the inside bottom of the wheel hub while the downward pointing sputter head, which is normally recessed, is manually translated into the wheel hub to perform the sputtering step. The wheel serves two purposes: 1) to move the samples out of the way by rotating them to the top of the wheel while the nitrogen gun and sputter head are being warmed up or powered down and 2) to pass the samples through the nitrogen ion or sputtering plumes at a defined rate and number of passes to normalize the exposure in at least one axis.

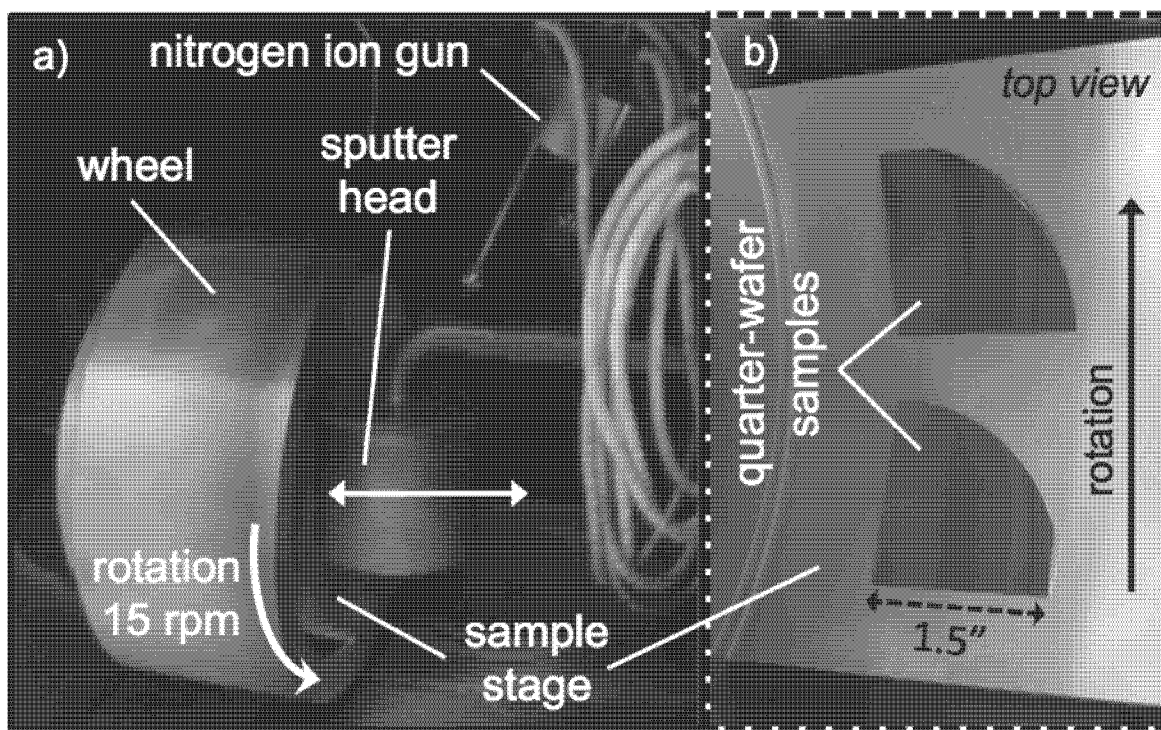


Figure 4.3.1 Inside of the vacuum chamber in which the nitridation and sputtering surface treatments are performed. At right, two samples are mounted on the sample stage.

The samples treated were 2- $\mu\text{m}$  thick Zn-doped p-type ( $10^{17} \text{ cm}^{-3}$ ) GaInP<sub>2</sub> films grown epitaxially on degenerately p-type GaAs substrates (same as Chapters 4.1) with evaporated

Ti/Au ohmic back contacts. A 3" wafer of the epilayer material was cleaved into quarters, each to be used in one of the four treatment variations. Additionally, a quarter wafer of bare GaAs substrate served as witness sample. Although not suitable for PEC measurements, it provided additional data without consuming more of the expensive p-GaInP<sub>2</sub> epilayer material.

Figure 4.3.1 shows a p-GaInP<sub>2</sub> quarter wafer sample placed in front, relative to the direction of rotation, of the GaAs quarter; both mounted and electrically grounded to the wheel by double-sided copper tape. The chamber is pumped down to  $\sim 5 \times 10^{-6}$  Torr base pressure before using a leak valve to introduce and control nitrogen flow through the ion gun in order to establish a chamber pressure of  $7 \times 10^{-4}$  Torr. With the wheel rotated to put the sample stage in the "up" position so it is out of ion gun line of sight, the ion gun is turned on and adjusted to a stable 12 mA ion beam current. The nitridation treatment is performed by rotating the wheel at 15 rpm for 9 min, passing the sample through the ion beam  $\sim 135$  times. For a "full" treatment, a sputtering step using a Pt<sub>0.5</sub>Ru<sub>0.5</sub> alloy target follows. The sputter head is moved into place within the wheel and the chamber evacuated to base pressure before introducing and maintaining 10 mTorr argon background. With samples in the "up" position, the sputter head power supply is adjusted to 20 W DC (0.066 A, 297 V), establishing an Ar plasma allowed to stabilize for 2 min. Then, PtRu sputtering proceeds as two wheel rotations, again at 15 rpm, so that the samples pass underneath the sputter head twice.

Expecting indirect PtRu incorporation during "nitridation-only" treatments as discussed, we first establish reproducible background conditions by preconditioning the sample wheel and stage by direct PtRu sputtering for 30 minutes at 15 rpm. Next, the wafer quarters we have labeled A, B, C, and D undergo the following treatments:

**A) Sputtering only;** only the PtRu sputtering step performed

**B) Full treatment;** sequence of nitridation followed by PtRu sputtering

**C) N<sup>2+</sup>-only alt.;** nitridation step only, with ion gun translated 1" away to alternate position

**D) N<sup>2+</sup>-only std.;** nitridation step only, with standard, centered ion gun position

The alternate nitridation treatment (C) was included to test the influence of the nitrogen ion gun placement relative to the samples. For consistency, we have arranged results into A, B, C, and D quadrants within the figures that follow.

### **Quantifying PtRu loading**

The wafer quarters were cleaved into 13 8x8-mm square pieces (Figure 4.3.2) appropriate for testing in a PEC compression cell (Chapter 2.3). All edges from quarter-wafer perimeters were trimmed or excluded because they contain PtRu sputtered onto the sample sides that 1) overestimates surface loading, and 2) cause electrical short to the substrate. Originally, 5 of 13 samples were submitted for PtRu quantification by ICP-MS analysis, but technical error associated with the destructive technique caused results to be lost; those samples are labeled with "x". Of the remaining eight, four were left as 8x8 mm squares for PEC testing and the other four were cut in half to get greater spatial resolution and re-submitted for ICP-MS.

After measuring each sample's surface area, ICP-MS was performed by Clay MacComber and Heli Wang at NREL. Aqua regia dissolved or digested the entirety of each sample into solution of which 0.24 mL was diluted in 11.76 mL DI water before analyzing. The measured Pt and Ru (in ppb) values were converted to an equivalent film thickness. The calculation assumes Pt and Ru to be present individually and as continuous, dense films. In reality, TEM shows a dispersion of ~5 nm particles having ~30% surface coverage [33]. The

continuous-film-equivalent thicknesses (CFET) convention, used for convenience of discussion, is calculated as:

$$CFET (nm) = \frac{Pt \text{ or } Ru (ppb)}{10^9} \times 12 \text{ mL} \times \frac{1 \text{ mL}}{0.24 \text{ mL}} \times \frac{1 \text{ g}}{\text{mL}} \times \frac{1}{\text{Density (g/cm}^3\text{)}} \times \frac{1}{\text{Area (cm}^2\text{)}} \times \frac{10^7 \text{ nm}}{1 \text{ cm}}$$

Here, 12 mL is the diluted solution volume, 1/0.24 is the dilution factor, and the densities of Pt and Ru are 21.45 g/cm<sup>3</sup> and 12.45 g/cm<sup>3</sup>, respectively.

The cleaving and PEC sample labeling scheme for each treated quarter wafer are shown in Figure 4.3.2 along with Pt CFET loading results. Since the ratio of Ru to Pt was consistent among samples within each treatment, we list its average and standard deviation rather than individual Ru loading values. To elucidate spatial variation within each and differences among the four treatments, the CFET values are highlighted with a color palette ranging from green to red for highest and lowest loading respectively with yellow representing intermediate loading. The average Pt loading and standard deviation values for each treatment are listed in Table 4.3.1 for direct comparison between the four treatments.

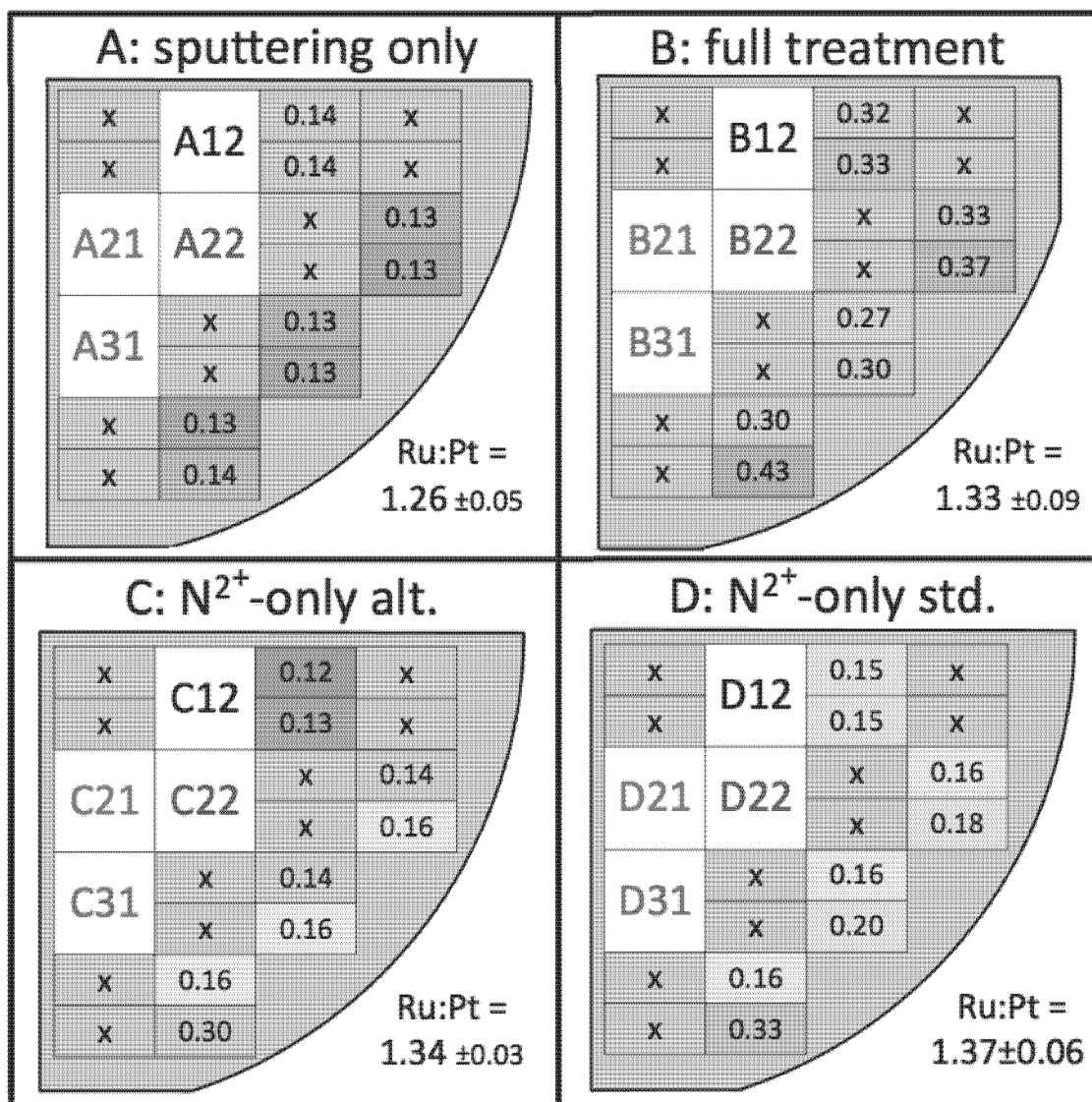


Figure 4.3.2. Four quadrants A-D contain a schematic for each treated quarter wafer showing 1) how each was cleaved after treatment; 2) the labeling for durability-tested samples (e.g. treatment A: A12, A21, A22, A31 etc.); and 3) the Pt CFET (in nm) quantified with ICP-MS and highlighted using color palette ranging from high (green) to low (red) loading. The Ru:Pt ratio is listed in the lower right of each quadrant.

Table 4.3.1 Average Ru and Pt loading among samples within each treatment

Treatment	Ru (nm)	Pt (nm)	Ru:Pt ratio
A) sputtering only	0.17 ±0.01	0.13 ±0.01	1.26 ±0.05
B) full treatment	0.44 ±0.07	0.33 ±0.05	1.33 ±0.09
C) N <sup>2+</sup> -only alt.	0.22 ±0.08	0.17 ±0.06	1.34 ±0.03
D) N <sup>2+</sup> -only std.	0.25 ±0.07	0.19 ±0.06	1.37 ±0.06

From Table 4.3.1, we see that the two nitridation treatments resulted in Pt and Ru loadings that are statistically the same, while each had a high-loading data point closest to the ion gun (0.3 and 0.33 values in Figures 4.3.2C, D). Whether the outlier is included or excluded, the average loading for either nitridation step is similar to the loading for sputtering and the full treatment is approximately the sum of the parts. The spatial variation within each treated quarter-wafer is the lowest for sputtering ( $\pm 0.01$  nm) and ranges from  $\pm 0.05$ – $0.08$  nm for all others, indicating that greater loading variability results from the nitridation step and persists in the full treatment.

### Durability testing

Four 8x8 mm samples from each of the four treatments, represented by the 16 white squares in Figure 4.3.2, were durability tested under conditions similar to those used for p-GaAs in Chapter 4.3.2. The only difference is that a lower current density,  $-10$  mA/cm<sup>2</sup> instead of  $-15$  mA/cm<sup>2</sup>, is appropriate for p-GaInP<sub>2</sub> because of the lower light-limited photocurrent inherent to its higher bandgap. The p-GaInP<sub>2</sub> photocathodes were durability tested for 24 h at constant current while monitoring operating potential vs. MSE reference electrode as shown in Figure 4.3.3. CLIVs characterize performance before and after the 24-h tests (Figure 4.3.4). To

summarize and evaluate results, we establish performance metrics: During the durability test, the metric is simply the operating potential at 10 min, 1 h, and 24 h elapsed time. A decreasing or more negative potential means that the galvanostat is providing additional cathodic bias, compensating for the photocathode's inability to maintain constant current. Conversely, an increasing or more positive potential would indicate improved performance. From CLIVs (Figure 4.3.4), 1) photocurrent and 2) photovoltage metrics are taken, respectively, as the 1) current density at -0.6 V vs. MSE and 2) voltage vs. MSE at -10 mA/cm<sup>2</sup> current density. An example determining the CLIV metrics is shown in the upper left quadrant of Figure 4.3.4. To facilitate analysis, the metrics for all durability tests are tabulated (Table 4.3.2) with their values highlighted using a color palette to indicate performance with green for the best, yellow for intermediate, and red for the worst.

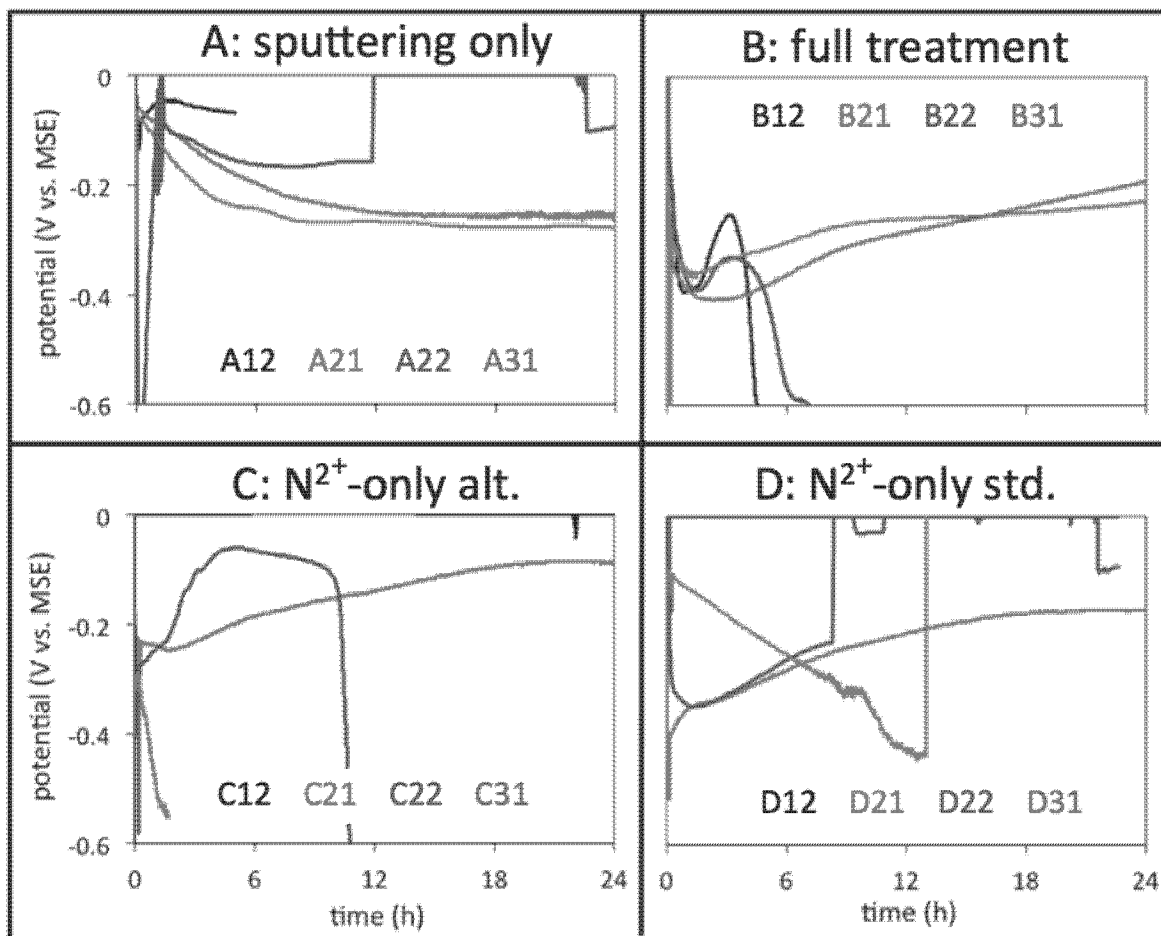


Figure 4.3.3: The monitored potential (V vs. MSE) during the 24-h durability testing of four samples taken from each treated quarter-wafer.

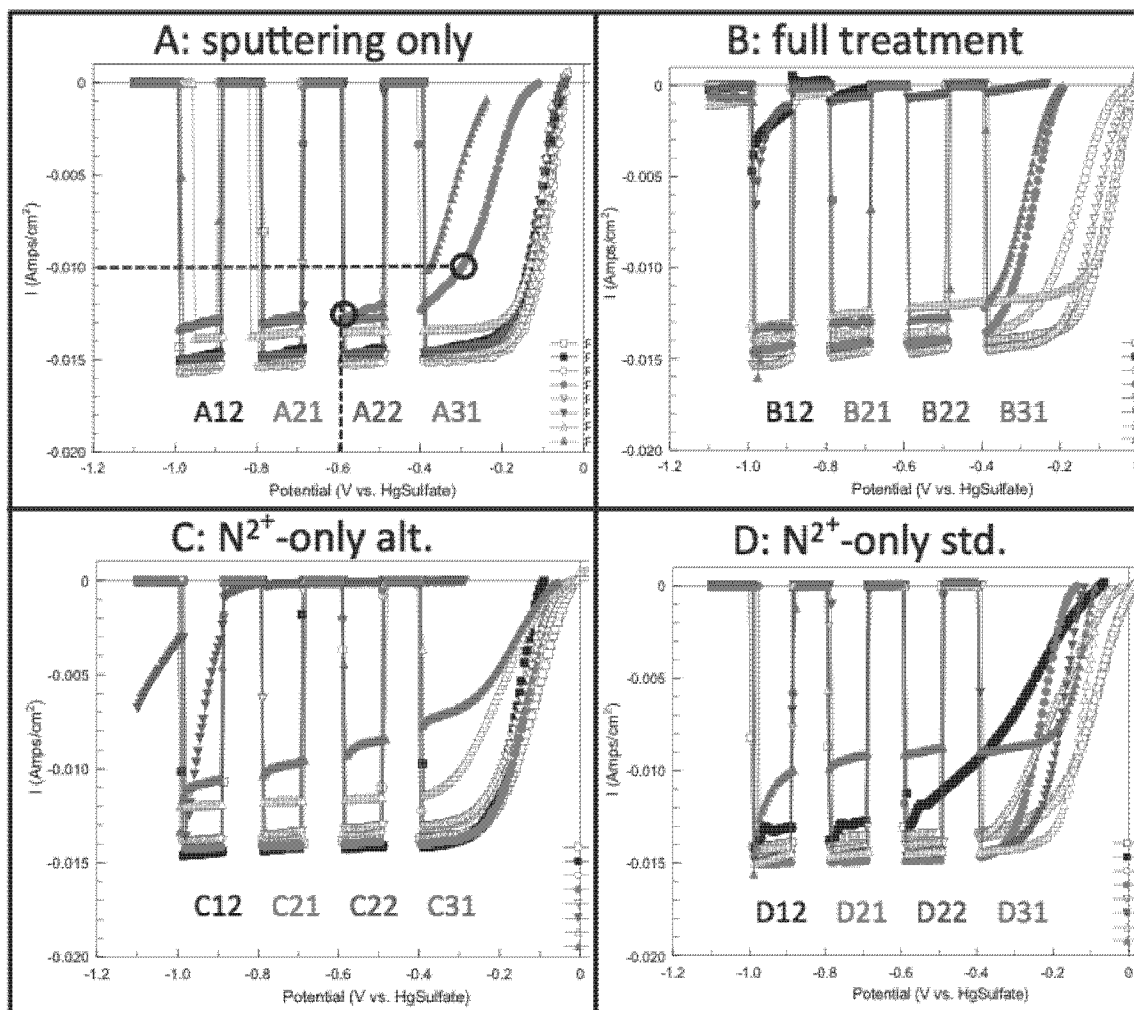


Figure 4.3.4: CLIVs taken before (open-marker data) and after (solid-marker data) 24-h durability testing. An example of extracting durability metrics is shown in the upper left quadrant for sample A21: The photocurrent metric is taken at -0.6 V vs. MSE and the photovoltage metric at -10 mA/cm<sup>2</sup>.

Table 4.3.2: Summary of durability metrics for the four treatments A, B, C, and D

		potential listed as V vs. MSE, current densities as mA/cm <sup>2</sup>						
durability metrics	sample	CLIV before		V during			CLIV after	
		<i>J</i> at -0.6 V	<i>V</i> 10 mA/cm <sup>2</sup>	10 m	1 h	24 h	<i>j</i> at -0.6 V	<i>V</i> 10 mA/cm <sup>2</sup>
	control	5.0	-0.60	-0.70	-1.20	-1.30	0.0	-1.00
A) sputtering only	A12	15.2	-0.11	-0.08	-0.05	-0.10	14.8	-0.14
	A21	15.1	-0.10	-0.06	-0.09	-0.26	12.8	-0.30
	A22	14.9	-0.11	-0.09	-0.11	-0.08	14.7	-0.13
	A31	13.5	-0.14	-0.08	-0.12	-0.28	12.9	-0.38
B) full treatment	B12	14.1	-0.11	-0.22	-0.39	-1.35	0.0	-1.00
	B21	13.7	-0.21	-0.31	-0.39	-0.19	14.2	-0.31
	B22	14.7	-0.14	-0.22	-0.38	-1.28	0.8	-1.00
	B31	12.2	-0.12	-0.25	-0.35	-0.23	12.9	-0.34
C) N <sup>2+</sup> -only alt. pos.	C12	13.8	-0.16	-0.35	-0.38	N/A	14.3	-0.19
	C21	13.4	-0.19	-0.23	-0.24	-0.09	14.0	-0.17
	C22	13.2	-0.19	-0.27	-0.25	-0.96	0.1	-0.96
	C31	11.6	-0.30	-0.21	-0.40	N/A	9.3	-0.77
D) N <sup>2+</sup> -only std. pos.	D12	13.5	-0.15	-0.28	-0.31	-0.71	12.9	-0.43
	D21	13.9	-0.15	-0.40	-0.35	-0.17	14.9	-0.25
	D22	14.0	-0.26	-0.32	-0.35	-0.09	14.6	-0.20
	D31	14.5	-0.15	-0.10	-0.13	-0.44	9.4	-0.58

The durability metrics for control, untreated p-GaInP<sub>2</sub> are included in the top row of Table 4.3.2 (taken from Chapter 4.2, Figure 4.2.1.). The control does not have the PtRu catalytic properties of the treated samples and so the metrics from its initial CLIV, perhaps, underrepresent its initial condition; it does have the same light-limited photocurrents, between 13 and 15 mA/cm<sup>2</sup>, as treated samples, but at potentials cathodic of -0.6 V vs. MSE, where the metric is taken. Regardless, its operating potential is considerably worse than all treated samples after 1 h. Within 24 h, complete failure establishes baseline durability metrics; treated samples that also fail (e.g. B12, B22, C22) take similar values. We note two values are not available due to equipment malfunction as noted by gray, N/A boxes.

One trend distinguishable in the highlighting scheme of Table 4.3.2 is the better (green) initial performance of the A) sputtering-only samples. To consider whether the trend is statistically significant, we plot the average photovoltage metric over time for each treatment including error bars of  $\pm 1$  standard deviation (Figure 4.3.5).

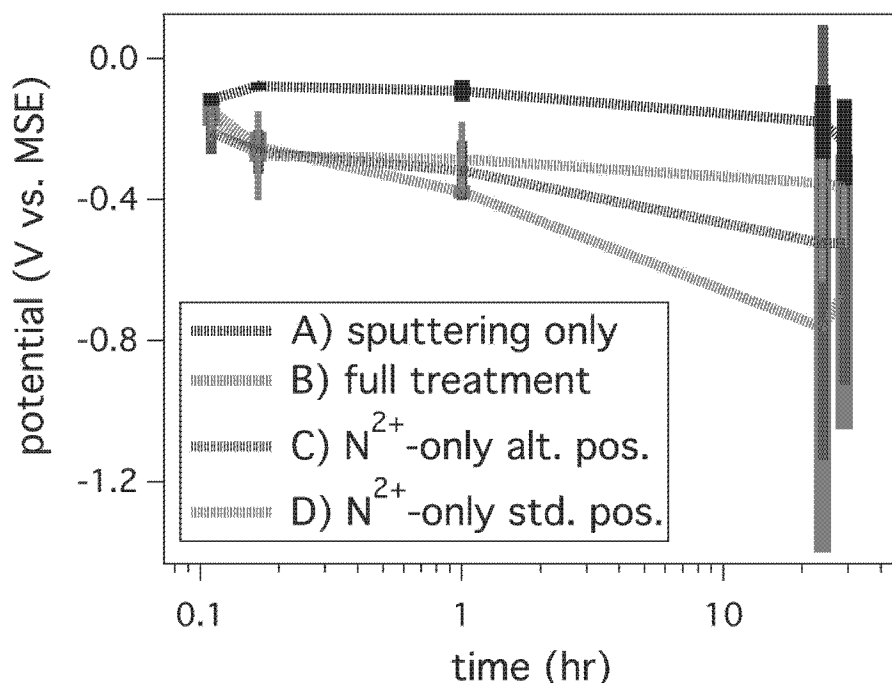


Figure 4.3.5: The photovoltage metric averages over time are shown for each treatment along with error bars of  $\pm 1$  standard deviation. Note that the first (0.1 h) and last (25 h) photovoltage metrics are taken from CLIVs while the middle three are from the 24-hr durability tests.

Figure 4.3.5 shows that initial performance, taken from CLIV before testing, is indistinguishable for all treatments. The second set of values at 10 min show that the sputtering-only samples improve and are distinctly better than the other three treatments. These performance levels are maintained, for the most part, after 1 h testing. After 24 h, considerable variability in the photovoltage metric is attributed to complete failure of one or two samples from each treatment except for sputtering only. We note the variability for A is considerably smaller than all other

treatments throughout, however, large statistical overlap precludes distinction among all treatments at 24 h and after, where data is taken from CLIV after 24 h. Still, the better performance of sputtering only at 10 min and 1 h is validated.

### **Post-durability analysis**

After each durability test, samples were removed from the PEC compression cell, rinsed with DI water, and blown dry with nitrogen. Their surfaces and profiles were imaged with a stereomicroscope (Figure 4.3.6) and optical profilometer (Figure 4.3.7). In each stereomicroscope image, a visible ring of carbon particle residue left by the washer (see Chapter 4.2) conveniently outlines the active region that was exposed to electrolyte during testing.

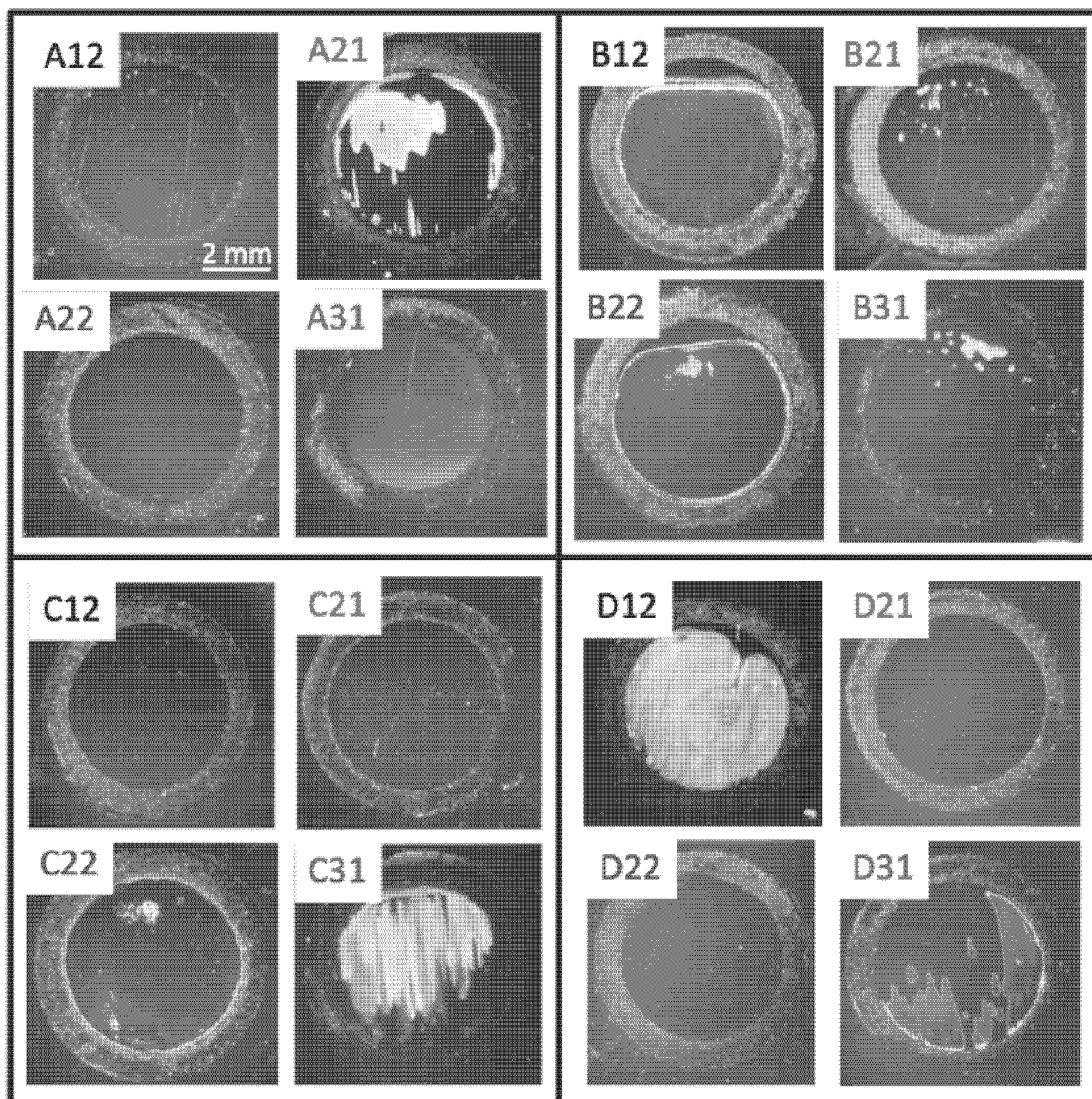


Figure 4.3.6: Stereomicroscope images of p-GaInP<sub>2</sub> photocathode surfaces after 24 h durability testing. The ring visible in each image corresponds to where the compression cell washer was contacting the surface, the area within it being the active region.

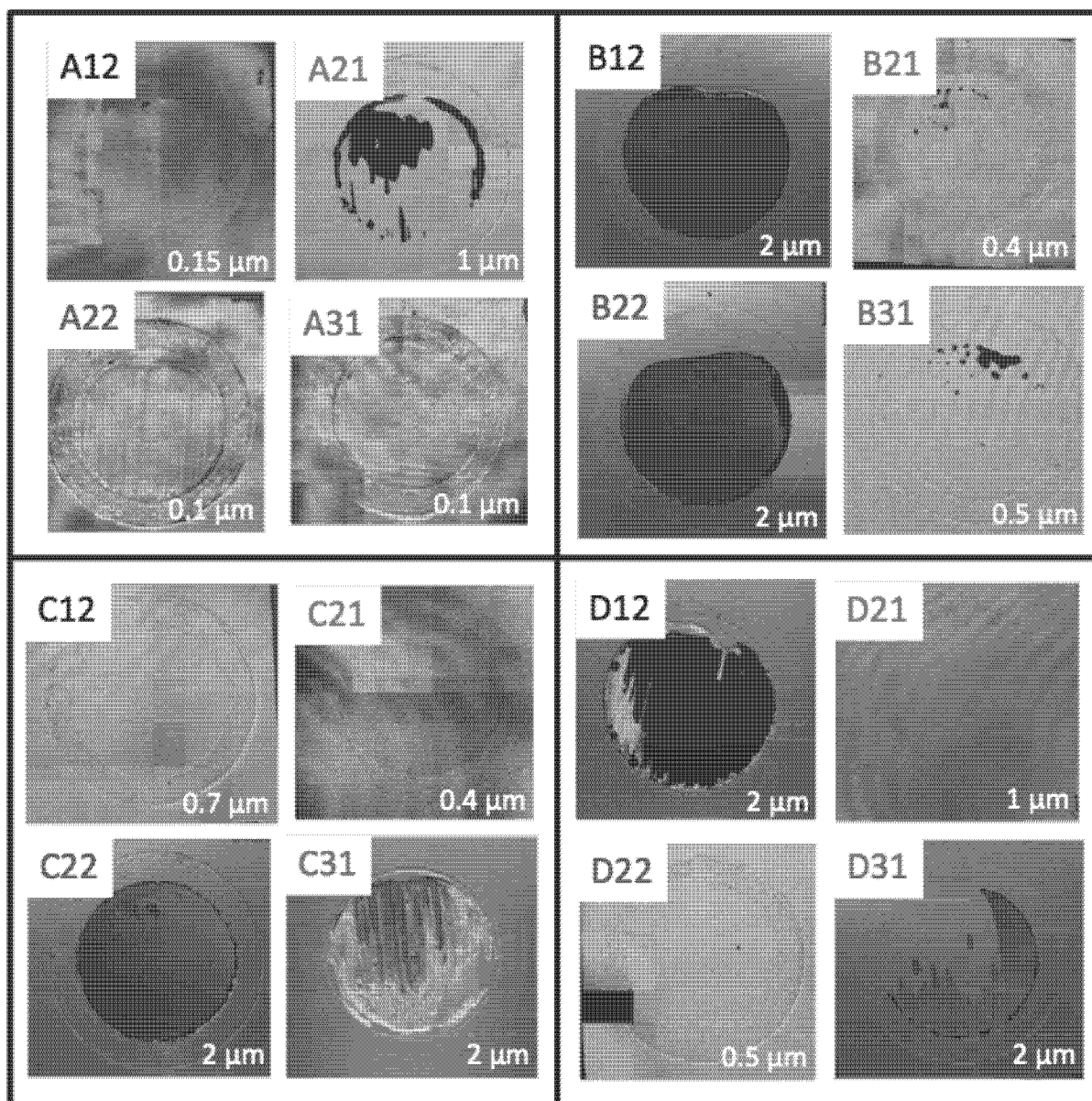


Figure 4.3.7: Optical profilometry of p-GaInP<sub>2</sub> photocathode surfaces after 24 h durability testing. Height is indicated with color scale from blue (lower) to red (higher). The span between maximum and minimum in the height scale is indicated in the lower right and is different for each image, allowing greater texture resolution to be shown for minimally corroded samples.

From the stereomicroscope images (Figure 4.3.6) and profilometry (Figure 4.3.7), we classify each sample as: 1) pristine or minimally corroded, 2) partially corroded, or 3) mostly or fully corroded. Samples A12, A22, A31, B21, B31, C12, C21, D21, and D22 appear pristine or minimally corroded; A21 and D31 appear partially corroded; and B12, B22, C22, C31, and D12

appear mostly or fully corroded. Samples from the latter set show etch depths on the order of the p-GaInP<sub>2</sub> epilayer thickness (1–2 μm) over most of the active area, which is the area within the washer ring. In Chapter 4.2, we showed that p-GaAs, which is also the substrate for our p-GaInP<sub>2</sub> epilayers, is very stable. Thus, frequently observing 1–2 μm depths indicates that most or all of the p-GaInP<sub>2</sub> is removed and etching stops at the p-GaAs substrate.

A common corrosion feature of p-GaInP<sub>2</sub> manifests as shiny silver/blue regions (Figure 4.3.6). Sample C31 shows both blue and silver while A21 and D12 show a silver appearance over much of the photoelectrode area. Samples B12, B22, and C22 show a blue/silver ring spatially concomitant with the washer's inner perimeter. To further investigate, we monitor its evolution during a durability test, stopping at 1 h to examine with SEM-EDS. On untreated p-GaInP<sub>2</sub>, we observe a blue appearance within 5 min which transitions to silver/white within 1 h (Figure 4.3.8). Observed *in operando* from the side, the color progression is thus the result of

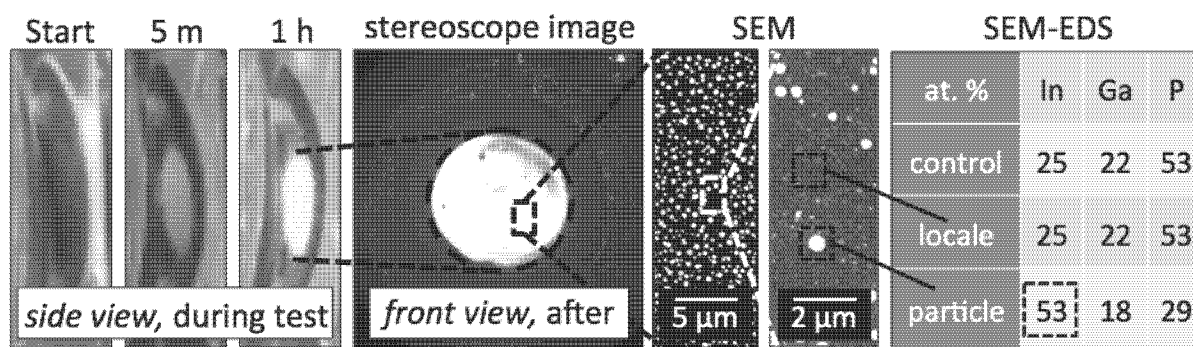


Figure 4.3.8: From the left, an untreated p-GaInP<sub>2</sub> photocathode surface transitions to blue then white appearance within 1 h of photocathodic H<sub>2</sub> evolution. Removed from solution at 1 h, the surface is a shiny white manifest as bright, sub-micron particles under SEM, which EDS analysis reveals to be >2x more In-rich than the 1:1:2 stoichiometry of GaInP<sub>2</sub>.

light scattered by the photoelectrode surface. The *front view* appears very bright under the stereomicroscope illumination and the SEM image shows a dispersion of bright, sub-micron, particles to be responsible for the light scattering. We posit the ripening of these particles during

the testing caused scattering that is initially more efficient for blue light as the particles reach dimensions of its wavelength. Further ripening results in a particle size distribution that efficiently scatters all wavelengths to appear white. We compare SEM-EDS taken directly on a particle to that taken in the darker region (locale) around it and an area that was not exposed to electrolyte (control). The latter two have 1:1:2 stoichiometry similar to that expected for GaInP<sub>2</sub>, while the particle more In-rich by a factor of two. If let sit at open-circuit potential in the dark, the particles are observed to dissolve in the 3M sulfuric acid as expected from electrochemical equilibria diagrams [35] of In or Ga. Since the dissolved In ions are more easily reduced to In than Ga ions to Ga, the In-rich particles can be explained by selective redeposition on the surface during photocathodic operation.

## Conclusions

We performed four treatment variations of nitridation and/or PtRu sputtering of p-GaInP<sub>2</sub> photocathode surfaces; quantified Pt and Ru loadings on the order of 0.1-nm CFET; and test and characterize the durability of each treatment. We conclude that the sputtering-only treatment provides the best PtRu loading uniformity and gives significantly better performance after 10 min and 1 h durability testing. Uniformity and stable initial performance makes sputtering-only the preferred treatment for III-V device development, while higher variability and rapid initial photovoltage decline makes the other treatments less desirable. Although some samples treated with a nitridation step almost fully recovered photovoltage performance over 24 h, about half failed completely. This large variability precluded distinction among the surface treatments after 24 h, yet future work should include extended durability testing.

## References

- [1] M. Houssa, D. Nelis, D. Hellin, G. Pourtois, T. Conard, K. Paredis, K. Vanormelingen, A. Vantomme, M. K. Van Bael, J. Mullens, M. Caymax, M. Meuris, and M. M. Heyns, "H<sub>2</sub>S exposure of a (100)Ge surface: Evidences for a (2x1) electrically passivated surface," *Appl. Phys. Lett.*, vol. 90, no. 22, pp. 3–6, 2007.
- [2] S. Oktyabrsky and P. D. Ye, *Fundamentals of III-V semiconductor MOSFETs*. 2010.
- [3] M. Houssa, E. Chagarov, and A. Kummel, "Surface Defects and Passivation of Ge and III–V Interfaces," *MRS Bull.*, vol. 34, no. 07, pp. 504–513, 2009.
- [4] J. Janata, "Thirty Years of CHEMFETs - A Personal View," *Electroanalysis*, vol. 16, no. 22, pp. 1831–1835, Nov. 2004.
- [5] X. Liu, Y. Sun, M. Yu, Y. Yin, B. Yang, W. Cao, and M. N. R. Ashfold, "Incident fluence dependent morphologies, photoluminescence and optical oxygen sensing properties of ZnO nanorods grown by pulsed laser deposition," *J. Mater. Chem. C*, vol. 3, no. 11, pp. 2557–2562, 2015.
- [6] M. A. Reshchikov, "Strong suppression of the yellow luminescence in C-doped GaN in air ambient," *Appl. Phys. Lett.*, vol. 89, no. 23, pp. 1–4, 2006.
- [7] S. S. Kocha, M. W. Peterson, A. J. Nelson, Y. Rosenwaks, D. J. Arent, and J. A. Turner, "Investigation of Chemical Wet-Etch Surface Modification of Ga<sub>0.5</sub>In<sub>0.5</sub>P Using Photoluminescence, X-Ray Photoelectron-Spectroscopy, Capacitance Measurements, and Photocurrent-Voltage Curves," *J. Phys. Chem.*, vol. 99, no. 2, pp. 744–749, 1995.
- [8] O. Khaselev and J. A. Turner, "A Monolithic Photovoltaic-Photoelectrochemical Device for Hydrogen Production via Water Splitting," *Science (80-. )*, vol. 280, no. 5362, pp. 425–427, 1998.
- [9] M. M. May, H.-J. Lewerenz, D. Lackner, F. Dimroth, and T. Hannappel, "Efficient direct solar-to-hydrogen conversion by in situ interface transformation of a tandem structure," *Nat. Commun.*, vol. 6, p. 8286, 2015.
- [10] H. Döscher, J. F. Geisz, T. G. Deutsch, and J. A. Turner, "Sunlight absorption in water – efficiency and design implications for photoelectrochemical devices," *Energy Environ. Sci.*, vol. 7, no. 9, pp. 2951–2956, 2014.
- [11] B. C. Wood, T. Ogitsu, and E. Schwegler, "Ab initio modeling of water–semiconductor

- interfaces for photocatalytic water splitting: role of surface oxygen and hydroxyl,” *J. Photonics Energy*, vol. 1, no. 1, p. 016002, 2011.
- [12] H. Lewerenz, B. Aspnes, B. Miller, L. Malm, and A. Heller, “Semiconductor Interface Characterization in Photoelectrochemical Solar Cells: The p-InP(111)A Face,” no. 1, pp. 3325–3329, 1982.
- [13] A. Heller, “Hydrogen-evolving solar cells,” *Science*, vol. 223, no. 4641, pp. 1141–8, 1984.
- [14] J. W. Elam, M. D. Groner, and S. M. George, “Viscous flow reactor with quartz crystal microbalance for thin film growth by atomic layer deposition,” *Rev. Sci. Instrum.*, vol. 73, no. 8, p. 2981, 2002.
- [15] J. A. Turner, “Energetics of the Semiconductor-Electrolyte Interface,” *J. Chem. Educ.*, vol. 60, no. 4, pp. 327–329, 1983.
- [16] T. Otaredian, “The influence of the surface and oxide charge on the surface recombination process,” *Solid. State. Electron.*, vol. 36, no. 6, p. 905, 1993.
- [17] Z. Chen, T. F. Jaramillo, T. G. Deutsch, A. Kleiman-Shwarscstein, A. J. Forman, N. Gaillard, R. Garland, K. Takanabe, C. Heske, M. Sunkara, E. W. McFarland, K. Domen, E. L. Miller, J. a. Turner, and H. N. Dinh, “Accelerating materials development for photoelectrochemical hydrogen production: Standards for methods, definitions, and reporting protocols,” *J. Mater. Res.*, vol. 25, no. 01, pp. 3–16, 2010.
- [18] I. Langmuir, “The Adsorption of Gases on Plane Surfaces of Glass, Mica and Platinum,” *J. Am. Chem. Soc.*, vol. 40, no. 9, pp. 1361–1403, 1918.
- [19] W. Shockley and W. T. Read, “Statistics of the Recombination of Holes and Electrons,” *Phys. Rev.*, vol. 87, no. 46, pp. 835–842, 1952.
- [20] R. N. Hall, “Electron-Hole Recombination in Germanium,” *Phys. Rev.*, vol. 87, no. 387, p. 6, 1952.
- [21] R. S. Muller and T. I. Kamins, *Device electronics for integrated circuits*, 3rd ed. New York: John Wiley & Sons, 2003.
- [22] R. I. Masel, *Principles of adsorption and reaction on solid surfaces*. New York: Wiley, 1951.

- [23] J. U. Keller and R. Staudt, *Gas Adsorption Equilibria: Experimental Methods and Adsorptive Isotherms*, vol. 33. Boston: Springer US, 2005.
- [24] X. Zhang and S. Ptasinska, “Distinct and dramatic water dissociation on GaP(111) tracked by near-ambient pressure X-ray photoelectron spectroscopy,” *Phys. Chem. Chem. Phys.*, vol. 17, pp. 3909–3918, 2015.
- [25] R. R. King, C. M. Fetxer, P. C. Colter, K. M. Edmondson, D. C. Law, A. P. Stavrides, H. Yoon, G. S. Kinsey, H. L. Cotal, J. H. Ermer, R. A. Sherif, K. Emery, W. Metzger, R. K. Ahrenkiel, and N. H. Karam, “Lattice-matched and metamorphic GaInP/GaInAs/Ge concentrator solar cells,” pp. 10–13, 2003.
- [26] D. K. Schröder, “Carrier lifetimes in silicon,” *IEEE Trans. Electron Devices*, vol. 44, no. 1, pp. 160–170, 1997.
- [27] J. I. Izpura, “Surface-assisted luminescence: The PL yellow band and the EL of n-GaN devices,” *Adv. Condens. Matter Phys.*, vol. 2013, 2013.
- [28] A. Dobrich, P. Kleinschmidt, H. Döscher, and T. Hannappel, “Quantitative investigation of hydrogen bonds on Si(100) surfaces prepared by vapor phase epitaxy,” *J. Vac. Sci. Technol. B Microelectron. Nanom. Struct.*, vol. 29, no. 4, p. 04D114, 2011.
- [29] K. A. Stoerzinger, W. T. Hong, G. Azimi, L. Giordano, Y. Lee, E. J. Crumlin, M. D. Biegalski, H. Bluhm, and K. K. Varanasi, “Reactivity of Perovskites with Water: Role of Hydroxylation in Wetting and Implications for Oxygen Electrocatalysis,” *J. Phys. Chem. C*, no. 001, 2015.
- [30] H. Döscher, A. Dobrich, S. Brückner, P. Kleinschmidt, and T. Hannappel, “Si(100) surfaces in a hydrogen-based process ambient,” *Appl. Phys. Lett.*, vol. 97, no. 15, p. 151905, 2010.
- [31] S. Brückner, H. Döscher, P. Kleinschmidt, and T. Hannappel, “In situ investigation of hydrogen interacting with Si(100),” *Appl. Phys. Lett.*, vol. 98, no. 21, p. 211909, 2011.
- [32] J. Turner, T. Deutsch, H. Wang, A. Welch, and M. Al-jassim, “II.F.2 Semiconductor Materials for Photoelectrolysis,” *DOE Hydrogen and Fuel Cells Program FY 2012 Annual Progress Report.*, 2012. [Online]. Available: [http://www.hydrogen.energy.gov/pdfs/progress12/ii\\_f\\_2\\_turner\\_2012.pdf](http://www.hydrogen.energy.gov/pdfs/progress12/ii_f_2_turner_2012.pdf).
- [33] T. G. Deutsch and J. A. Turner, “Semiconductor Materials for Photoelectrolysis: 2014 U.S. DOE Hydrogen & Fuel Cells Program Review,” 2014.

- [34] A. A. Dameron, T. S. Olson, S. T. Christensen, J. E. Leisch, K. E. Hurst, S. Pylypenko, J. B. Bult, D. S. Ginley, R. P. O. Hayre, H. N. Dinh, T. Gennett, R. P. O'Hayre, H. N. Dinh, and T. Gennett, "Pt-Ru Alloyed Fuel Cell Catalysts Sputtered from a Single Alloyed Target," *ACS Catal.*, vol. 1, no. 10, pp. 1307–1315, 2011.
- [35] M. Pourbaix, *Atlas of Electrochemical Equilibria in Aqueous Solutions*, 2nd ed. National Association of Corrosion Engineers, 1974.

## 5. Conclusions and Outlook

### 5.1 Conclusions

PEC water splitting can be a viable pathway toward economical solar hydrogen production. STH conversion efficiency is the key benchmarking figure of merit for comparing technologies and evaluating progress toward commercial viability. We evaluated common measurement practices to identify illumination spectra and area definition as underestimated sources of error. We propose standards that include: 1) full disclosure of the illumination source(s) and configuration and/or a measured spectrum, 2) thorough device-area definition avoiding indirect light paths, and 3) cross-validation with IPCE measurement.

We introduced the IMM tandem growth technique and device architecture that can allow monolithic pairing of absorber bandgaps capable of reaching the maximum practical 25% STH efficiency. The IMM devices demonstrated greater spectral utilization primarily through a lower bottom bandgap, a tradeoff that required work in improving photovoltage to maintain spontaneous water splitting. An IMM with improved "p-n" PEC junction doping profile attained 13.5% STH efficiency while being capable of reaching 16% with another 0.1 V photovoltage improvement. Still, we calculated the top GaInP<sub>2</sub> junction to be current limiting with a reflection-limited photocurrent of 14.8 mA/cm<sup>2</sup>. The photocurrent loss of 26% of the E<sub>g</sub>-limited photocurrent is largely due to reflection at the GaInP<sub>2</sub>|electrolyte interface. This compares to IQE charge collection losses of just 5–10%. We identified the requirements of suitable ARCs on photocathodes, selected TiO<sub>2</sub> as a nearly ideal candidate material, calculated the optimal thickness based on the spectral response of tandem devices, and demonstrated a 2–3-mA/cm<sup>2</sup>

photocurrent enhancement when applied to p-GaInP<sub>2</sub> photocathodes. The TiO<sub>2</sub> ARC should afford 20% STH efficiency when applied to the IMM device reported here.

We presented durability testing and post-analysis of III-V photocathodes that included unmodified p-GaAs, unmodified p-GaInP<sub>2</sub>, and p-GaInP<sub>2</sub> modified with surface treatment variants involving nitridation and PtRu sputtering steps. We showed p-GaAs to be remarkably stable; orders of magnitude more so than p-GaInP and p-InP, which sharply contrasts with popular perception that high-performance III-V photocathodes are generally unstable. Analysis supported As as the stabilizing surface species, motivating further investigation of III-V arsenides. Of the treatment variants studied on p-GaInP<sub>2</sub>, the sputtering-only treatment provided the best PtRu loading uniformity and gave better performance after 10 min and 1 h. All samples treated with a nitridation step showed a photovoltage decline in the first 10 min. After 24 h, some stabilized or even recovered while about half completely failed. This large variability precluded statistical distinction among the surface treatments after 24 h of testing. Still, we showed that the sputtering-only treatment gives better initial performance and uniformity, making it preferable for III-V device development.

To date, we have exceeded Department of Energy progress milestones for STH efficiency and durability, while considerable reduction of device processing cost remains to be addressed.

## 5.2 Outlook

The IMM approach allows great flexibility in tandem bandgap pairings. Meeting future milestones may require lowering the top junction bandgap in addition to the bottom. This can be achieved with slightly more In-rich alloys of GaInP<sub>2</sub> or alternatives such as AlGaAs or GaInAsP. Since the bottom solid-state junction is well understood, considerable emphasis will be on

optimizing the top PEC junction photovoltage performance with the tradeoff of using even lower bandgaps.

Considerable progress has been made in improving the stability of high-performance photoelectrodes to the range of hundreds of hours. Still, photoelectrodes serve as template systems, and in addition to improving their longevity, durability testing protocol must advance toward more stringent conditions of unbiased water splitting as the tandem devices capable of doing so become a more vetted concept. Since ARCs are necessary for highest efficiency, approaches could shift toward stabilizing the coating material and coated device systems rather than the absorber material itself. However, texture-based anti-reflective strategies such as black Si are an alternative to ARCs that still require a stable or stabilized absorber material.

The PEC pathway to hydrogen has the potential to become economically viable, but significant semiconductor cost reduction remains a critical challenge. With IMM device thickness being on the order of just microns, material requirements are minimal while the substrate dominates semiconductor cost. Thus, substrate re-use by methods such as epitaxial liftoff will be critical to lowering semiconductor cost. Additionally, moderate levels of solar concentration should be feasible for further reducing the required semiconductor area by at least a factor of ten.

# Complete Bibliography

## Chapter 1 References

- [1] M. A. K. Khalil, “Non-CO<sub>2</sub> Greenhouse gases in the atmosphere,” *Annu. Rev. Energy Environ.*, vol. 24, no. 1, pp. 645–661, 1999.
- [2] M. I. Hoffert, K. Caldeira, A. K. Jain, E. F. Haites, L. D. D. Harvey, S. D. Potter, M. E. Schlesinger, S. H. Schneider, R. G. Watts, T. M. L. Wigley, and D. J. Wuebbles, “Energy implications of future stabilization of atmospheric CO<sub>2</sub> content,” *Nature*, vol. 395, no. 6705, pp. 881–884, 1998.
- [3] N. S. Lewis, G. Crabtree, A. J. Nozik, M. R. Wasielewski, and P. Alivisatos, “Basic Research Needs for Solar Energy Utilization,” *Basic Energy Sci. Work. Sol. Energy Util.*, p. 276, 2005.
- [4] UNDP, *World Energy Assessment. Energy and the challenge of Sustainability*. 2000.
- [5] P. Moriarty and D. Honnery, “What is the global potential for renewable energy?,” *Renew. Sustain. Energy Rev.*, vol. 16, no. 1, pp. 244–252, 2012.
- [6] R. F. Service, “Solar energy. Is it time to shoot for the sun?,” *Science*, vol. 309, no. 5734, pp. 548–551, 2005.
- [7] V. Smill and R. A. Streatfeild, “Enriching the earth: Fritz Haber, Carl Bosch, and the transformation of world food production,” *Electronic Green Journal*, no. 17. 2002.
- [8] B. Kroposki, J. Levene, K. Harrison, P. K. Sen, and F. Novachek, “Electrolysis: Information and opportunities for electric power utilities,” 2006.
- [9] B. D. James, G. N. Baum, J. Perez, and K. N. Baum, “Technoeconomic analysis of photoelectrochemical (PEC) hydrogen production,” *DOE Contract Number GS-10F-009J*, vol. 22201, no. December, pp. 1–128, 2009.
- [10] B. a. Pinaud, J. D. Benck, L. C. Seitz, A. J. Forman, Z. Chen, T. G. Deutsch, B. D. James, K. N. Baum, G. N. Baum, S. Ardo, H. Wang, E. Miller, and T. F. Jaramillo, “Technical and economic feasibility of centralized facilities for solar hydrogen production via photocatalysis and photoelectrochemistry,” *Energy Environ. Sci.*, vol. 6, no. 7, p. 1983, 2013.

- [11] B. U. Bossel, "Does a Hydrogen Economy Make Sense?," vol. 94, no. 10, 2006.
- [12] "Department of Energy Fuel Cell Technologies Office Multi-year Research, Development, and Demonstration Plan," 2015. [Online]. Available: [http://energy.gov/sites/prod/files/2015/06/f23/fcto\\_myrrdd\\_production.pdf](http://energy.gov/sites/prod/files/2015/06/f23/fcto_myrrdd_production.pdf).
- [13] A. J. Bard and L. R. Faulkner, *Electrochemical Methods: Fundamentals and Applications*. Wiley, 2000.
- [14] H. Döscher, J. F. Geisz, T. G. Deutsch, and J. A. Turner, "Sunlight absorption in water – efficiency and design implications for photoelectrochemical devices," *Energy Environ. Sci.*, vol. 7, no. 9, pp. 2951–2956, 2014.
- [15] T. Bak, J. Nowotny, M. Rekas, and C. . Sorrell, "Photo-electrochemical hydrogen generation from water using solar energy. Materials-related aspects," *Int. J. Hydrogen Energy*, vol. 27, no. 10, pp. 991–1022, 2002.
- [16] B. A. MacLeod, K. X. Steirer, J. L. Young, U. Koldemir, A. Sellinger, J. A. Turner, T. G. Deutsch, and D. C. Olson, "Phosphonic Acid Modification of GaInP<sub>2</sub> Photocathodes Toward Unbiased Photoelectrochemical Water Splitting," *ACS Appl. Mater. Interfaces*, vol. 7, no. 21, pp. 11346–11350, 2015.
- [17] "ASTM G173-03, Standard Tables for Reference Solar Spectral Irradiances: Direct Normal and Hemispherical on 37° Tilted Surface, ASTM International, West Conshohocken, PA, 2003, [www.astm.org](http://www.astm.org)."
- [18] O. Khaselev and J. A. Turner, "A Monolithic Photovoltaic-Photoelectrochemical Device for Hydrogen Production via Water Splitting," *Science (80-. )*, vol. 280, no. 5362, pp. 425–427, 1998.
- [19] X. Gao, "Photoelectrochemical decomposition of water using modified monolithic tandem cells," pp. 208–214.
- [20] M. M. May, H.-J. Lewerenz, D. Lackner, F. Dimroth, and T. Hannappel, "Efficient direct solar-to-hydrogen conversion by in situ interface transformation of a tandem structure," *Nat. Commun.*, vol. 6, p. 8286, 2015.
- [21] R. R. King, D. Bhusari, A. Boca, D. Larrabee, X.-Q. Liu, W. Hong, C. M. Fetzer, D. C. Law, and N. H. Karam, "Bandgap-Voltage Offset and Energy Production in Next-Generation Multijunction Solar Cells," *5th World Conf. Photovolt. Energy Convers. 25th Eur. Photovolt. Sol. Energy Conf.*, pp. 6–10, 2010.
- [22] M. C. Hanna and A. J. Nozik, "Solar conversion efficiency of photovoltaic and photoelectrolysis cells with carrier multiplication absorbers," *J. Appl. Phys.*, vol. 100, no. 7, pp. 1–8, 2006.

- [23] J. R. Bolton, S. J. Strickler, and J. S. Connolly, "Limiting and realizable efficiencies of solar photolysis of water," *Nature*, vol. 316, no. 6028, pp. 495–500, 1985.
- [24] F. F. Abdi, L. Han, A. H. M. Smets, M. Zeman, B. Dam, and R. van de Krol, "Efficient solar water splitting by enhanced charge separation in a bismuth vanadate-silicon tandem photoelectrode.," *Nat. Commun.*, vol. 4, p. 2195, 2013.
- [25] S. Y. Reece, J. a. Hamel, K. Sung, T. D. Jarvi, a. J. Esswein, J. J. H. Pijpers, and D. G. Nocera, "Wireless Solar Water Splitting Using Silicon-Based Semiconductors and Earth-Abundant Catalysts," *Science (80-. )*, vol. 334, no. 6056, pp. 645–648, 2011.
- [26] M. a. Green, *Third generation photovoltaics: advanced solar energy conversion*, vol. 10. 2006.
- [27] J. W. Ager III, M. Shaner, K. Walczak, I. D. Sharp, and S. Ardo, "Experimental Demonstrations of Spontaneous, Solar-Driven Photoelectrochemical Water Splitting," *Energy Environ. Sci.*, vol. 2, no. 1, pp. 1–3, 2015.
- [28] S. Hu, N. S. Lewis, J. W. Ager, J. Yang, J. R. McKone, and N. C. Strandwitz, "Thin-Film Materials for the Protection of Semiconducting Photoelectrodes in Solar-Fuels Generators," *J. Phys. Chem. C*, p. 150928141004000, 2015.
- [29] S. Hu, M. R. Shaner, J. a Beardslee, M. Lichterman, B. S. Brunschwig, and N. S. Lewis, "Amorphous TiO<sub>2</sub> coatings stabilize Si, GaAs, and GaP photoanodes for efficient water oxidation.," *Science*, vol. 344, no. 6187, pp. 1005–9, 2014.
- [30] B. Seger, T. Pedersen, A. B. Laursen, P. C. K. K. Vesborg, O. Hansen, and I. Chorkendorff, "Using TiO<sub>2</sub> as a conductive protective layer for photocathodic H<sub>2</sub> evolution," *J. Am. Chem. Soc.*, vol. 135, no. 3, pp. 1057–1064, 2013.
- [31] J. Turner, T. Deutsch, H. Wang, A. Welch, and M. Al-jassim, "II.F.2 Semiconductor Materials for Photoelectrolysis," *DOE Hydrogen and Fuel Cells Program FY 2012 Annual Progress Report.*, 2012. [Online]. Available: [http://www.hydrogen.energy.gov/pdfs/progress12/ii\\_f\\_2\\_turner\\_2012.pdf](http://www.hydrogen.energy.gov/pdfs/progress12/ii_f_2_turner_2012.pdf).
- [32] M. a. Modestino, K. a. Walczak, A. Berger, C. M. Evans, S. Haussener, C. Koval, J. S. Newman, J. W. Ager, and R. a. Segalman, "Robust production of purified H<sub>2</sub> in a stable, self-regulating, and continuously operating solar fuel generator," *Energy Environ. Sci.*, vol. 7, no. 1, p. 297, 2014.
- [33] J. D. Benck, S. C. Lee, K. D. Fong, J. Kibsgaard, R. Sinclair, and T. F. Jaramillo, "Designing Active and Stable Silicon Photocathodes for Solar Hydrogen Production Using Molybdenum Sulfide Nanomaterials," *Adv. Energy Mater.*, p. n/a–n/a, 2014.

- [34] B. Mei, B. Seger, T. Pedersen, M. Malizia, O. Hansen, I. Chorkendorff, and P. C. K. Vesborg, "Protection of p + -n-Si Photoanodes by Sputter-Deposited Ir/IrO<sub>x</sub> Thin Films," *J. Phys. Chem. Lett.*, vol. 5, no. 11, pp. 1948–1952, 2014.
- [35] K. Sun, F. H. Saadi, M. F. Lichterman, W. G. Hale, H.-P. Wang, X. Zhou, N. T. Plymale, S. T. Omelchenko, J.-H. He, K. M. Papadantonakis, B. S. Brunshwig, and N. S. Lewis, "Stable solar-driven oxidation of water by semiconducting photoanodes protected by transparent catalytic nickel oxide films," *Proc. Natl. Acad. Sci.*, p. 201423034, 2015.
- [36] T. G. Deutsch and J. A. Turner, "Semiconductor Materials for Photoelectrolysis: 2014 U.S. DOE Hydrogen & Fuel Cells Program Review," 2014.
- [37] "[http://www.nrel.gov/ncpv/images/efficiency\\_chart.jpg](http://www.nrel.gov/ncpv/images/efficiency_chart.jpg)."

## Chapter 2 References

- [1] "ASTM G173-03, Standard Tables for Reference Solar Spectral Irradiances: Direct Normal and Hemispherical on 37° Tilted Surface, ASTM International, West Conshohocken, PA, 2003, [www.astm.org](http://www.astm.org)."
- [2] Z. Chen, T. F. Jaramillo, T. G. Deutsch, A. Kleiman-Shwarscstein, A. J. Forman, N. Gaillard, R. Garland, K. Takanabe, C. Heske, M. Sunkara, E. W. McFarland, K. Domen, E. L. Miller, J. a. Turner, and H. N. Dinh, "Accelerating materials development for photoelectrochemical hydrogen production: Standards for methods, definitions, and reporting protocols," *J. Mater. Res.*, vol. 25, no. 01, pp. 3–16, 2010.
- [3] K. A. Bertness, S. R. Kurtz, D. J. Friedman, A. E. Kibbler, C. Kramer, and J. M. Olson, "29.5%-efficient GaInP/GaAs tandem solar cells," *Appl. Phys. Lett.*, vol. 65, no. 8, p. 989, 1994.
- [4] O. Khaselev and J. A. Turner, "A Monolithic Photovoltaic-Photoelectrochemical Device for Hydrogen Production via Water Splitting," *Science (80-. )*, vol. 280, no. 5362, pp. 425–427, 1998.
- [5] "NREL-SRRL, [http://www.nrel.gov/midc/srri\\_bms/](http://www.nrel.gov/midc/srri_bms/)."
- [6] A. Chai, "Some basic considerations of measurements involving collimated direct sunlight." Lewis Research Center, National Aeronautics and Space Administration, Cleveland, OH, pp. 233–246, 1976.
- [7] T. W. Cannon, "Spectral solar irradiance instrumentation and measurement techniques," *Sol. Cells*, vol. 18, pp. 233–241, 1986.
- [8] K. Emery, "Solar simulators and I–V measurement methods," *Sol. Cells*, vol. 18, no. 3–4, pp. 251–260, 1986.

- [9] H. Döscher, J. F. Geisz, T. G. Deutsch, and J. A. Turner, “Sunlight absorption in water – efficiency and design implications for photoelectrochemical devices,” *Energy Environ. Sci.*, vol. 7, no. 9, pp. 2951–2956, 2014.
- [10] Z. Chen, H. N. Dinh, and E. Miller, *Photoelectrochemical Water Splitting: Standards, Experimental Methods, and Protocols*. 2013.
- [11] E. Verlage, S. Hu, R. Liu, R. J. R. Jones, K. Sun, C. Xiang, N. S. Lewis, H. A. Atwater, Jr., and H. A. Atwater, “A Monolithically Integrated, Intrinsically Safe, 10% Efficient, Solar-Driven Water-Splitting System Based on Active, Stable Earth-Abundant Electrocatalysts in Conjunction with Tandem III-V Light Absorbers Protected by Amorphous TiO<sub>2</sub> Films,” *Energy Environ. Sci.*, pp. 1–13, 2015.
- [12] T. G. Deutsch and J. A. Turner, “Semiconductor Materials for Photoelectrolysis: 2014 U.S. DOE Hydrogen & Fuel Cells Program Review,” 2014.
- [13] T. G. Deutsch, C. a. Koval, and J. a. Turner, “III-V nitride epilayers for photoelectrochemical water splitting: GaPN and GaAsPN,” *J. Phys. Chem. B*, vol. 110, no. 50, pp. 25297–25307, 2006.
- [14] M. A. Green, *Solar Cells*. 2013.

### Chapter 3 References

- [1] B. D. James, G. N. Baum, J. Perez, and K. N. Baum, “Technoeconomic analysis of photoelectrochemical (PEC) hydrogen production,” *DOE Contract Number GS-10F-009J*, vol. 22201, no. December, pp. 1–128, 2009.
- [2] H. Döscher, J. F. Geisz, T. G. Deutsch, and J. A. Turner, “Sunlight absorption in water – efficiency and design implications for photoelectrochemical devices,” *Energy Environ. Sci.*, vol. 7, no. 9, pp. 2951–2956, 2014.
- [3] O. Khaselev and J. A. Turner, “A Monolithic Photovoltaic-Photoelectrochemical Device for Hydrogen Production via Water Splitting,” *Science (80-. )*, vol. 280, no. 5362, pp. 425–427, 1998.
- [4] J. F. Geisz, S. Kurtz, M. W. Wanlass, J. S. Ward, a. Duda, D. J. Friedman, J. M. Olson, W. E. McMahon, T. E. Moriarty, and J. T. Kiehl, “High-efficiency GaInPGaAsInGaAs triple-junction solar cells grown inverted with a metamorphic bottom junction,” *Appl. Phys. Lett.*, vol. 91, no. 2, pp. 1–4, 2007.
- [5] D. Shahrjerdi, S. W. Bedell, C. Bayram, and D. Sadana, “Flexible InGaP/(In)GaAs tandem solar cells with very high specific power,” *Photovolt. Spec. Conf. (PVSC), 2013 IEEE 39th*, pp. 2805–2808, 2013.

- [6] T. G. Deutsch and J. A. Turner, "Semiconductor Materials for Photoelectrolysis: 2014 U.S. DOE Hydrogen & Fuel Cells Program Review," 2014.
- [7] Z. Chen, H. N. Dinh, and E. Miller, *Photoelectrochemical Water Splitting: Standards, Experimental Methods, and Protocols*. 2013.
- [8] Z. Chen, T. F. Jaramillo, T. G. Deutsch, A. Kleiman-Shwarscstein, A. J. Forman, N. Gaillard, R. Garland, K. Takanabe, C. Heske, M. Sunkara, E. W. McFarland, K. Domen, E. L. Miller, J. a. Turner, and H. N. Dinh, "Accelerating materials development for photoelectrochemical hydrogen production: Standards for methods, definitions, and reporting protocols," *J. Mater. Res.*, vol. 25, no. 01, pp. 3–16, 2010.
- [9] R. R. King, D. Bhusari, A. Boca, D. Larrabee, X.-Q. Liu, W. Hong, C. M. Fetzer, D. C. Law, and N. H. Karam, "Bandgap-Voltage Offset and Energy Production in Next-Generation Multijunction Solar Cells," *5th World Conf. Photovolt. Energy Convers. 25th Eur. Photovolt. Sol. Energy Conf.*, pp. 6–10, 2010.
- [10] R. R. King, D. C. Law, K. M. Edmondson, C. M. Fetzer, G. S. Kinsey, H. Yoon, R. a. Sherif, and N. H. Karam, "40% efficient metamorphic GaInP/GaInAs/Ge multijunction solar cells," *Appl. Phys. Lett.*, vol. 90, no. 18, pp. 98–100, 2007.
- [11] B. A. MacLeod, K. X. Steirer, J. L. Young, U. Koldemir, A. Sellinger, J. A. Turner, T. G. Deutsch, and D. C. Olson, "Phosphonic Acid Modification of GaInP<sub>2</sub> Photocathodes Toward Unbiased Photoelectrochemical Water Splitting," *ACS Appl. Mater. Interfaces*, vol. 7, no. 21, pp. 11346–11350, 2015.
- [12] S. S. Kocha, J. a. Turner, and a. J. Nozik, "Study of the Schottky barrier and determination of the energetic positions of band edges at the n- and p-type gallium indium phosphide electrode | electrolyte interface," *J. Electroanal. Chem.*, vol. 367, no. 1–2, pp. 27–30, 1994.
- [13] R. S. Muller and T. I. Kamins, *Device electronics for integrated circuits*, 3rd ed. New York: John Wiley & Sons, 2003.
- [14] J. A. Turner, "Energetics of the Semiconductor-Electrolyte Interface," *J. Chem. Educ.*, vol. 60, no. 4, pp. 327–329, 1983.
- [15] S. W. Boettcher, E. L. Warren, M. C. Putnam, E. a. Santori, D. Turner-Evans, M. D. Kelzenberg, M. G. Walter, J. R. McKone, B. S. Brunschwig, H. a. Atwater, and N. S. Lewis, "Photoelectrochemical hydrogen evolution using Si microwire arrays," *J. Am. Chem. Soc.*, vol. 133, no. 5, pp. 1216–1219, 2011.
- [16] A. Bansal and J. Turner, "Suppression of band edge migration at the p-GaInP<sub>2</sub>/H<sub>2</sub>O interface under illumination via catalysis," *J. Phys. Chem. B*, vol. 104, pp. 6591–6598, 2000.

- [17] W. A. Smith, I. D. Sharp, N. C. Strandwitz, and J. Bisquert, “Interfacial band-edge energetics for solar fuels production,” *Energy Environ. Sci.*, vol. 8, no. 10, pp. 2851–2862, 2015.
- [18] J. Krepelka, “Maximally flat antireflective coatings,” *Jemná Mech. A Opt.*, vol. 53, pp. 3–5, 1992.
- [19] S. M. George, “Atomic layer deposition: An overview,” *Chem. Rev.*, vol. 110, no. 1, pp. 111–131, 2010.
- [20] B. Seger, T. Pedersen, A. B. Laursen, P. C. K. K. Vesborg, O. Hansen, and I. Chorkendorff, “Using TiO<sub>2</sub> as a conductive protective layer for photocathodic H<sub>2</sub> evolution,” *J. Am. Chem. Soc.*, vol. 135, no. 3, pp. 1057–1064, 2013.
- [21] M. Malizia, B. Seger, I. Chorkendorff, and P. C. K. Vesborg, “Formation of a p–n heterojunction on GaP photocathodes for H<sub>2</sub> production providing an open-circuit voltage of 710 mV,” *J. Mater. Chem. A*, vol. 2, no. 19, p. 6847, 2014.
- [22] A. Paracchino, N. Mathews, T. Hisatomi, M. Stefiik, S. D. Tilley, and M. Grätzel, “Ultrathin films on copper(i) oxide water splitting photocathodes: a study on performance and stability,” *Energy Environ. Sci.*, vol. 5, no. 9, p. 8673, 2012.

## Chapter 4 References

- [1] M. Houssa, D. Nelis, D. Hellin, G. Pourtois, T. Conard, K. Paredis, K. Vanormelingen, A. Vantomme, M. K. Van Bael, J. Mullens, M. Caymax, M. Meuris, and M. M. Heyns, “H<sub>2</sub>S exposure of a (100)Ge surface: Evidences for a (2x1) electrically passivated surface,” *Appl. Phys. Lett.*, vol. 90, no. 22, pp. 3–6, 2007.
- [2] S. Oktyabrsky and P. D. Ye, *Fundamentals of III-V semiconductor MOSFETs*. 2010.
- [3] M. Houssa, E. Chagarov, and A. Kummel, “Surface Defects and Passivation of Ge and III–V Interfaces,” *MRS Bull.*, vol. 34, no. 07, pp. 504–513, 2009.
- [4] J. Janata, “Thirty Years of CHEMFETs - A Personal View,” *Electroanalysis*, vol. 16, no. 22, pp. 1831–1835, Nov. 2004.
- [5] X. Liu, Y. Sun, M. Yu, Y. Yin, B. Yang, W. Cao, and M. N. R. Ashfold, “Incident fluence dependent morphologies, photoluminescence and optical oxygen sensing properties of ZnO nanorods grown by pulsed laser deposition,” *J. Mater. Chem. C*, vol. 3, no. 11, pp. 2557–2562, 2015.
- [6] M. A. Reshchikov, “Strong suppression of the yellow luminescence in C-doped GaN in air ambient,” *Appl. Phys. Lett.*, vol. 89, no. 23, pp. 1–4, 2006.

- [7] S. S. Kocha, M. W. Peterson, A. J. Nelson, Y. Rosenwaks, D. J. Arent, and J. A. Turner, "Investigation of Chemical Wet-Etch Surface Modification of Ga<sub>0.5</sub>In<sub>0.5</sub>P Using Photoluminescence, X-Ray Photoelectron-Spectroscopy, Capacitance Measurements, and Photocurrent-Voltage Curves," *J. Phys. Chem.*, vol. 99, no. 2, pp. 744–749, 1995.
- [8] O. Khaselev and J. A. Turner, "A Monolithic Photovoltaic-Photoelectrochemical Device for Hydrogen Production via Water Splitting," *Science (80-. )*, vol. 280, no. 5362, pp. 425–427, 1998.
- [9] M. M. May, H.-J. Lewerenz, D. Lackner, F. Dimroth, and T. Hannappel, "Efficient direct solar-to-hydrogen conversion by in situ interface transformation of a tandem structure," *Nat. Commun.*, vol. 6, p. 8286, 2015.
- [10] H. Döscher, J. F. Geisz, T. G. Deutsch, and J. A. Turner, "Sunlight absorption in water – efficiency and design implications for photoelectrochemical devices," *Energy Environ. Sci.*, vol. 7, no. 9, pp. 2951–2956, 2014.
- [11] B. C. Wood, T. Ogitsu, and E. Schwegler, "Ab initio modeling of water–semiconductor interfaces for photocatalytic water splitting: role of surface oxygen and hydroxyl," *J. Photonics Energy*, vol. 1, no. 1, p. 016002, 2011.
- [12] H. Lewerenz, B. Aspnes, B. Miller, L. Malm, and A. Heller, "Semiconductor Interface Characterization in Photoelectrochemical Solar Cells: The p-InP(111)A Face," no. 1, pp. 3325–3329, 1982.
- [13] A. Heller, "Hydrogen-evolving solar cells," *Science*, vol. 223, no. 4641, pp. 1141–8, 1984.
- [14] J. W. Elam, M. D. Groner, and S. M. George, "Viscous flow reactor with quartz crystal microbalance for thin film growth by atomic layer deposition," *Rev. Sci. Instrum.*, vol. 73, no. 8, p. 2981, 2002.
- [15] J. A. Turner, "Energetics of the Semiconductor-Electrolyte Interface," *J. Chem. Educ.*, vol. 60, no. 4, pp. 327–329, 1983.
- [16] T. Otaredian, "The influence of the surface and oxide charge on the surface recombination process," *Solid. State. Electron.*, vol. 36, no. 6, p. 905, 1993.
- [17] Z. Chen, T. F. Jaramillo, T. G. Deutsch, A. Kleiman-Shwarsctein, A. J. Forman, N. Gaillard, R. Garland, K. Takanabe, C. Heske, M. Sunkara, E. W. McFarland, K. Domen, E. L. Miller, J. a. Turner, and H. N. Dinh, "Accelerating materials development for photoelectrochemical hydrogen production: Standards for methods, definitions, and reporting protocols," *J. Mater. Res.*, vol. 25, no. 01, pp. 3–16, 2010.
- [18] I. Langmuir, "The Adsorption of Gases on Plane Surfaces of Glass, Mica and Platinum," *J. Am. Chem. Soc.*, vol. 40, no. 9, pp. 1361–1403, 1918.

- [19] W. Shockley and W. T. Read, "Statistics of the Recombination of Holes and Electrons," *Phys. Rev.*, vol. 87, no. 46, pp. 835–842, 1952.
- [20] R. N. Hall, "Electron-Hole Recombination in Germanium," *Phys. Rev.*, vol. 87, no. 387, p. 6, 1952.
- [21] R. S. Muller and T. I. Kamins, *Device electronics for integrated circuits*, 3rd ed. New York: John Wiley & Sons, 2003.
- [22] R. I. Masel, *Principles of adsorption and reaction on solid surfaces*. New York: Wiley, 1951.
- [23] J. U. Keller and R. Staudt, *Gas Adsorption Equilibria: Experimental Methods and Adsorptive Isotherms*, vol. 33. Boston: Springer US, 2005.
- [24] X. Zhang and S. Ptasinska, "Distinct and dramatic water dissociation on GaP(111) tracked by near-ambient pressure X-ray photoelectron spectroscopy," *Phys. Chem. Chem. Phys.*, vol. 17, pp. 3909–3918, 2015.
- [25] R. R. King, C. M. Fetxer, P. C. Colter, K. M. Edmondson, D. C. Law, A. P. Stavrides, H. Yoon, G. S. Kinsey, H. L. Cotal, J. H. Ermer, R. A. Sherif, K. Emery, W. Metzger, R. K. Ahrenkiel, and N. H. Karam, "Lattice-matched and metamorphic GaInP/GaInAs/Ge concentrator solar cells," pp. 10–13, 2003.
- [26] D. K. Schröder, "Carrier lifetimes in silicon," *IEEE Trans. Electron Devices*, vol. 44, no. 1, pp. 160–170, 1997.
- [27] J. I. Izpura, "Surface-assisted luminescence: The PL yellow band and the EL of n-GaN devices," *Adv. Condens. Matter Phys.*, vol. 2013, 2013.
- [28] A. Dobrich, P. Kleinschmidt, H. Döscher, and T. Hannappel, "Quantitative investigation of hydrogen bonds on Si(100) surfaces prepared by vapor phase epitaxy," *J. Vac. Sci. Technol. B Microelectron. Nanom. Struct.*, vol. 29, no. 4, p. 04D114, 2011.
- [29] K. A. Stoerzinger, W. T. Hong, G. Azimi, L. Giordano, Y. Lee, E. J. Crumlin, M. D. Biegalski, H. Bluhm, and K. K. Varanasi, "Reactivity of Perovskites with Water: Role of Hydroxylation in Wetting and Implications for Oxygen Electrocatalysis," *J. Phys. Chem. C*, no. 001, 2015.
- [30] H. Döscher, A. Dobrich, S. Brückner, P. Kleinschmidt, and T. Hannappel, "Si(100) surfaces in a hydrogen-based process ambient," *Appl. Phys. Lett.*, vol. 97, no. 15, p. 151905, 2010.
- [31] S. Brückner, H. Döscher, P. Kleinschmidt, and T. Hannappel, "In situ investigation of hydrogen interacting with Si(100)," *Appl. Phys. Lett.*, vol. 98, no. 21, p. 211909, 2011.

- [32] J. Turner, T. Deutsch, H. Wang, A. Welch, and M. Al-jassim, "II.F.2 Semiconductor Materials for Photoelectrolysis," *DOE Hydrogen and Fuel Cells Program FY 2012 Annual Progress Report.*, 2012. [Online]. Available: [http://www.hydrogen.energy.gov/pdfs/progress12/ii\\_f\\_2\\_turner\\_2012.pdf](http://www.hydrogen.energy.gov/pdfs/progress12/ii_f_2_turner_2012.pdf).
- [33] T. G. Deutsch and J. A. Turner, "Semiconductor Materials for Photoelectrolysis: 2014 U.S. DOE Hydrogen & Fuel Cells Program Review," 2014.
- [34] A. A. Dameron, T. S. Olson, S. T. Christensen, J. E. Leisch, K. E. Hurst, S. Pylypenko, J. B. Bult, D. S. Ginley, R. P. O. Hayre, H. N. Dinh, T. Gennett, R. P. O'Hayre, H. N. Dinh, and T. Gennett, "Pt-Ru Alloyed Fuel Cell Catalysts Sputtered from a Single Alloyed Target," *ACS Catal.*, vol. 1, no. 10, pp. 1307–1315, 2011.
- [35] M. Pourbaix, *Atlas of Electrochemical Equilibria in Aqueous Solutions*, 2nd ed. National Association of Corrosion Engineers, 1974.